Driven-dissipative Josephson dynamics in a high-impedance many-body environment

Samuel Cailleaux

THÈSE

Pour obtenir le grade de

DOCTEUR DE L'UNIVERSITÉ GRENOBLE ALPES

École doctorale : PHYS - Physique
Spécialité : Physique de la Matière Condensée et du Rayonnement
Unité de recherche : Laboratoire de Physique et de Modélisation des Milieux Condensés

Dynamique forcée et dissipative d'une jonction Josephson dans un environnement haute-impédance à N corps

Driven-dissipative Josephson dynamics in a high-impedance many-body environment

Présentée par :

Samuel CAILLEAUX

Direction de thèse :

Denis BASKO DIRECTEUR DE RECHERCHE, CNRS DELEGATION ALPES	Directeur de thèse
Nicolas ROCH CHARGE DE RECHERCHE HDR, CNRS DELEGATION ALPES	Co-directeur de thèse

Rapporteurs :

FABIAN HASSLER
FULL PROFESSOR, RWTH AACHEN UNIVERSITY
MAX HOFHEINZ
ASSOCIATE PROFESSOR, UNIVERSITE DE SHERBROOKE

Thèse soutenue publiquement le **2 juillet 2025**, devant le jury composé de :

JEAN-DAMIEN PILLET, PROFESSEUR, ÉCOLE POLYTECHNIQUE	Président
FABIAN HASSLER, FULL PROFESSOR, RWTH AACHEN UNIVERSITY	Rapporteur
MAX HOFHEINZ, ASSOCIATE PROFESSOR, UNIVERSITE DE SHERBROOKE	Rapporteur
Julia MEYER, PROFESSEURE DES UNIVERSITES, UNIVERSITE GRENOBLE ALPES	Examinatrice
JERÔME ESTEVE, CHARGE DE RECHERCHE, CNRS DELEGATION ILE-DE-FRANCE SUD	Examinateur

Abstract

Français. Cette thèse explore la dynamique d'une petite jonction Josephson couplée à une ligne de transmission de taille finie à haute impédance, en se concentrant sur la façon dont un tel système peut émuler correctement la dynamique dissipative de cette petite jonction. En effet, la dissipation est traditionnellement modélisée par le couplage à un système de taille infinie, ainsi la structure modale discrète et les faibles pertes d'une ligne de transmission de taille finie soulèvent la question suivante : peut-elle encore agir comme un bon réservoir dissipatif ? Tirant parti de la flexibilité des circuits supraconducteurs, nous intégrons une petite jonction dans une chaîne de grandes jonctions Josephson agissant comme une ligne de transmission à haute impédance. En associant mesures DC et micro-ondes, nous accédons à la fois aux propriétés de transport et à la réponse fréquentielle, ce qui permet une caractérisation complète du système. Nous étudions tout d'abord l'apparition des marches de Shapiro duales dans les jonctions Josephson, où un courant quantifié est observé sous irradiation micro-ondes. Cette expérience représente la première observation des marches de Shapiro duales dans les jonctions Josephson depuis leur prédiction théorique il y a plus de trente ans. En étudiant ce phénomène, nous découvrons des signatures d'un courant jusqu'alors inexpliqué à basse tension. Cela nous conduit à identifier un nouvel effet, que nous appelons l'effet Joule photonique : la jonction émet des photons dans la ligne de transmission, ce qui, en raison de sa taille finie et de son faible couplage avec le monde extérieur, provoque une surchauffe des modes. À des biais plus élevés, cet état thermique devient instable et le système subit une transition vers un état cohérent, similaire à une transition laser, où l'énergie se concentre dans les modes basse-fréquences du système. Nous observons et caractérisons cette transition expérimentalement. Ces résultats fournissent une vue détaillée de la dynamique hors d'équilibre d'une jonction couplée à un environnement structuré, et soulignent le rôle des effets de taille finie dans l'ingénierie de la dissipation.

English. This thesis explores the dynamics of a small Josephson junction coupled to a high-impedance, finite-size transmission line, focusing on how such a system can emulate correctly the dissipative dynamics of a Josephson junction. While dissipation is traditionally modeled via idealized thermal baths, the discrete mode structure and low losses of a finite transmission line raise the question: can it still act as a good dissipative reservoir? Leveraging the flexibility of superconducting circuits, we embed a small junction in a chain of larger Josephson junctions acting as a high-impedance transmission line. Using a combination of DC and microwave measurements, we access both transport properties and the finite-frequency response, enabling a full characterization of the system. We first study the appearance of dual Shapiro steps in Josephson junctions, where a quantized current is observed under microwave irradiation. This experiment represents the first observation of dual Shapiro steps in Josephson junctions since their theoretical prediction more than thirty years ago. While studying dual Shapiro steps, we find signatures of a previously unaccounted-for current at low voltages. This leads us to identify a new effect, which we call the photonic Joule effect: the junction emits photons into the line, which, due to its finite size and weak coupling to the outside world, causes the modes to overheat. At higher bias, this thermal state becomes unstable, and the system undergoes a transition into a coherent state, similar to a lasing transition, where energy condenses into the lowest modes of the system. We observe and characterize this transition experimentally. Altogether, these results provide a detailed view of the out of equilibrium dynamics of a junction coupled to a structured environment, and highlight the role of finite-size effects in engineered dissipation.

Contents

Chapter 1

Introduction

Statistical physics emerged in the late 19th century to reconcile the irreversible behavior of macroscopic systems with the time-reversibility of microscopic laws. The conceptual breakthroughs led by Boltzmann, Gibbs, and Maxwell enabled physicists to understand that dissipation is an emergent phenomenon arising from the interaction between the system of interest and a large reservoir of fluctuating microscopic degrees of freedom, usually called a bath. The formalization of this idea was pioneered by Einstein with his work on Brownian motion relating the dissipation experienced by a particle and the thermal fluctuations of the surrounding medium. This was followed by the works of Nyquist [1] and Onsager [2], and culminated with the development of the fluctuation-dissipation theorem in the 1950s by Callen & Walton [3], and Kubo [4]. Since then, the "system+reservoir" approach has been fruitfully applied to quantum systems, birthing a whole field of study on open quantum systems [5, 6]. While one usually foregoes the inner dynamics of the bath to concentrate on the subsystem alone, an interesting question is whether the subsystem itself can influence it in return. There exists a broad range of behaviors depending on the strength of this back-action, from the idealized heat bath, in which the environment remains effectively thermal and unperturbed, through intermediate cases where the subsystem impacts only locally the bath—as in quantum impurity problems like the Kondo model—to the extreme case of quantum measurement, where the subsystem induces a global, one might say macroscopic, change in the state of the environment.

Superconducting circuits have emerged as one of the platforms of choice to experimentally implement and study these models. The tools and techniques inherited from microelectronics offer them a remarkable tunability, while their low internal losses preserve quantum coherences on long timescales. But perhaps their greatest asset is the superconducting tunnel junction: the Josephson junction. Owning to its tunable non-linearity, it became the cornerstone of superconducting circuits, allowing physicists to implement almost any arbitrary Hamiltonian as a circuit. In particular, coupling a single junction to a few electromagnetic modes has allowed researchers to reproduce the results of cavity quantum electrodynamics (cQED) on a microchip, using the junction as an artificial atom. One can even go beyond the parameter regimes accessible in traditional cavity QED, as the coupling to the junction can be made nearly arbitrarily strong, again thanks to the flexibility of circuit engineering. However, despite its omnipresence in superconducting circuits, the dynamics of a single Josephson junction coupled to a dissipative bath is still a

topic of ongoing research to this day, with implications on numerous applications ranging from metrology, quantum phase transitions, quantum optics to quantum simulation and quantum information. In our case, the starting point of this thesis was the study of the dual Shapiro steps where a small Josephson junction shunted by a large resistor produces a quantized current under an external periodic drive. This effect was theorized back in 1985 [7] and had yet to be clearly observed in Josephson junctions at the start of this thesis, despite numerous past experimental efforts motivated by the prospect of using this quantized current as a metrological standard. One of the main challenges in observing dual Shapiro steps lied in the realization of a well-controlled dissipative environment coupled to the junction.

There are two main ways of implementing this dissipative bath in a circuit; the first one is to simply shunt the junction by a resistor R, this has the advantage of realizing a broadband environment from dc up to gigahertz frequencies while being straightforward to fabricate. The second way is to couple the junction to a semi-infinite transmission line of a given impedance Z_c, equivalent to a resistor with $R = Z_c$. The coupling to the line allows the junction to radiate away its energy in this photonic bath, akin to an atom in vacuum. The biggest benefit of using a transmission line is the possibility to directly collect and measure this radiation by using standard microwave measurement techniques, giving access to the microscopic dynamics of the bath—something impossible with a resistor. However, in practice, the transmission line is always of finite length due to impedance mismatch with the external circuitry, which causes light to reflect at the line boundary. This effectively forms a Fabry–Pérot cavity, limiting the junction's interaction to a finite set of modes. Although the number of accessible modes can reach into the hundreds, this remains far from the thermodynamic limit required for an ideal dissipative reservoir.

Moreover, as will be discussed in detail in Chapter 2, one usually requires the value of R to be high compared to the superconducting quantum of resistance $R_Q = h/4e^2 \approx 6.45\,\mathrm{k\Omega}$, above which interesting dissipative quantum effects, like the dual Shapiro steps mentioned above, emerge due to the enhancement of quantum fluctuations. For pure resistors, going to large resistance values is fairly trivial and one can easily reach the megaohm on chip. For transmission lines, however, the impedance $Z_c = \sqrt{L/C_g}$ is given by the ratio between the line's inductance per length L and its ground capacitance per length C_g. With current fabrication techniques the ground capacitance is, at best, a few attofarads per micrometer while the inductance per length can reach dozens of nanohenries per micrometer. This constrains the maximum achievable impedance to around $\sim 50\,\mathrm{k\Omega}$. Despite these shortcomings, the perspective of being able to measure the bath's internal degrees of freedom has cemented transmission lines as a powerful platform for realizing engineered dissipative environments. Yet a fundamental question remains:

Does a finite-size transmission line implements a good dissipative bath?

This thesis work seeks to address that question by studying the dynamics of a small Josephson junction embedded in a high-impedance transmission line composed of larger Josephson junctions. By combining dc and microwave measurements, we are able to fully characterize the system's response, enabling a direct correlation between its transport properties and its finite-frequency spectrum.

1.1 Main results and structure of the manuscript

On top of this introductory chapter, this manuscript contains four subsequent chapters.

Chapter 2 summarizes the main theoretical tools used to model the type of circuit studied in this work. We begin by reviewing the dynamics of a Josephson junction coupled to a dissipative environment, with a focus on transport properties. We then introduce the modeling of transmission lines and linear circuits, concluding with a discussion of Josephson chains. Chapter 3, 4, and 5 contain the main results of this thesis: the dual Shapiro steps, the photonic Joule effect, and the Josephson laser, respectively. Each of these phenomena was studied in samples with the same geometry: a small Junction embedded in an array of several thousands of large Josephson junction. The array of large Josephson junctions realizes a high-impedance transmission line, allowing us to access the dissipative dynamics of the small junction in the regime where fluctuations induce non-trivial signatures.

The starting point of this thesis was the investigation of dual Shapiro steps in this type of sample, which is the subject of Chapter 3. Transport measurements reveal a rich structure in the current-voltage characteristics where series of regularly spaced current peaks are observed. These peaks, separated by twice the superconducting gap $2\Delta/e$, are attributed to the successive resistive switching of individual junctions within the array. To model this behavior, the standard RCSJ model is extended to include voltage-dependent dissipation representing the superconducting gap. Numerical simulations reproduce the discrete current peaks through the sequential switching process. When shining a microwave tone of frequency f on this sample, we measure a quantized dc current following the relation $I = 2ef$, corresponding to the clocked transport of one Cooper pair per drive cycle. The locking of the charge transport manifest itself as a clear response in the microwave transmission spectrum when the strong drive is applied.

While studying the dual Shapiro steps, we stumbled upon a low voltage current which was not explainable with the available theories. This led us to develop the theoretical description of a new effect occurring in our circuit, presented in Chapter 4: the photonic Joule effect. Under a voltage bias, the small Josephson junction in our device dissipates its energy into the transmission line in the form of photons. However, the finite-size of the line and its low internal losses makes it overheat as soon as the power generated by the junction IV exceed the cooling rate of the line, determined by its coupling to the external world. We present both the theoretical modeling and the experimental verification of this effect in Chapter 4. In the theory part of the chapter we present three approaches to describe this overheating. The first two are based on the perturbative $P(E)$ theory which we use to self-consistently calculate the photonic temperature of the modes of the transmission line. The simplest approach assumes that all modes share the same temperature while for the second one we relax this assumption and derive a kinetic equation for each mode's population, leading to a different steady-state temperature per mode. Finally, as a third approach, we fully solve the classical equations of motion of the system and observe that the classical solution matches well the perturbative calculations. This is due to the chaotic nature of the classical dynamics which generates its own noise, thereby validating the perturbative approaches. After exposing these theoretical calculations, we move on to the experimental characterization of the photonic Joule

effect. We measure the emitted radiation from our sample in a frequency band spanning 100 MHz to 12 GHz, giving us access to the photonic populations of our modes, and allowing us to confront these populations against the ones predicted by the theory.

However, the thermal state generated by the photonic Joule effect does not persist for all voltages. Indeed, beyond a given voltage, the system undergoes an incoherent-to-coherent transition, akin to a lasing transition, where most of the thermal excitations "condense" in the lowest modes of the system, forming a coherent state. Chapter 5 is dedicated to the study of this coherent state. While this coherent transition is missed by the first two approaches developed in the modeling of the photonic Joule effect, the classical solution captures it rather well. As such we start the chapter with a brief theoretical study of this transition, capitalizing on the numerical simulation built for the photonic Joule effect. We then study the transition experimentally and obtain the phase diagram of the system by measuring coherent emission of the sample versus the applied bias voltage and the Josephson energy of the small junction.

Chapter 2

Modeling our superconducting circuits

2.1 The superconducting condensate

We will not delve into the microscopic details of the theory of superconductivity but rather recall the main descriptive tools of it. We are mainly concerned by describing the superconductivity in aluminum as it has been the material used in all the experiments presented in the following chapters. Like most elemental superconductors, aluminum is considered a conventional superconductor, meaning that its low-temperature behavior is well described by the Bardeen–Cooper–Schrieffer (BCS) theory. The essential idea of the theory is that, below a given critical temperature T_C, the Fermi sea of a material is unstable against the appearance of a condensate formed by bound pairs of electrons, called Cooper pairs [8]. The spectrum of the system becomes gapped, so that creating an excitation in the system by breaking a Cooper pair costs an energy 2Δ. We call Δ the *superconducting gap* (for our aluminum films $\Delta \approx 0.21$ meV). The Cooper pair condensate then behaves much like a charged superfluid allowing an electrical current to flow through the superconductor without dissipation. As is usual in the modeling of condensates [9], one defines a complex order parameter characterizing the macroscopic coherence of the system

$$\Psi(r,t) = \sqrt{\rho(r,t)}e^{i\phi(r,t)}, \tag{2.1}$$

where ρ represents the local density of Cooper pairs, and we call ϕ the *phase* of the condensate. In the rest of this work we will assume that all the currents passing through the superconducting electrodes of our circuit are sufficiently weak such that the order parameter can be considered uniform in these electrodes. Thus, the state of a superconducting electrode is fully characterized by one complex number, and so by a single pair of variables (ϕ, N). These correspond to the average phase of the electrode[1] and the total number of Cooper pairs in the electrode, respectively. The quantization of these variables is done by assuming the following commutation relation

$$\left[\hat{\phi}, \hat{N}\right] = -i. \tag{2.2}$$

In principle, this relation is approximate [9] and essentially relies on $\Delta/\delta \gg 1$, with δ the mean level spacing in the normal state, a condition we will suppose fulfilled for all the electrodes of our circuits. The link between the condensate variables and the electromagnetic circuit variables is done by invoking gauge invariance [10]. In the absence of external magnetic field, this yields the following relation (sometimes called the second Josephson relation) between the electrode flux Φ, linked to the electrode voltage V through Faraday's law $\dot{\Phi} = V$, and its superconducting phase ϕ:

$$\Phi_0\dot{\phi} = \dot{\Phi} \tag{2.3}$$

with $\Phi_0 = \hbar/2e$ the reduced superconducting flux quantum ($e > 0$ is the elementary charge). It is then customary to integrate this equation and directly identify Φ with $\phi\Phi_0$, thus imposing $-2eN = Q$, the charge on the electrode. This integration is not fully rigorous since ϕ, being a phase, is only defined modulo 2π (meaning N has integer support) while Φ is defined on $\mathbb{R}$ (and Q is continuous). In theory, we should therefore keep track of two degrees of freedom: the condensate one and

[1] To be exact, the average phase of an isolated superconductor is not gauge-invariant and thus redundant. Here, ϕ has to be understood as the gauge-invariant phase difference to some external ground node.

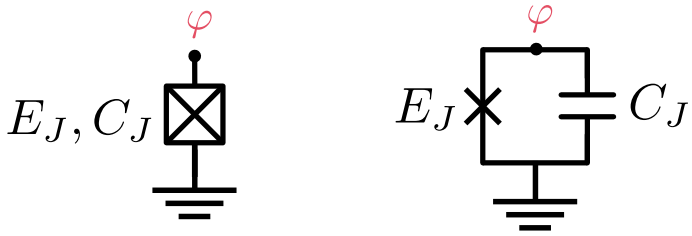

Figure 2.1: Two different ways of writing down the circuit representation for a Josephson junction with Josephson energy E_J and self-capacitance C_J. On the left the two contribution are bundled together in one symbol, while on the right they are explicitly separated.

the electromagnetic one, and then enforce Eq. (2.3) at all times. However, in our case, relaxing the condition of compactness of ϕ allows us to get rid of one degree of freedom without any change to the physical observables [11–13]. Thus, having made this identification, we will treat any superconducting phase as an extended variable and interchangeably use (ϕ, N) or (Φ, Q) to describe our circuits, even if some parts are non-superconducting.

2.2 The Josephson junction

2.2.1 Hamiltonian of an isolated junction

A Josephson junction is a superconducting tunnel junction obtained by separating two pieces of superconductor with a non-superconducting layer. All the junctions used in this thesis were Superconductor-Insulator-Superconductor (SIS) (see chapter 3 for more details). Placing ourselves in the low transparency limit for our tunneling channels, the Cooper pair current flowing through the barrier can be written as [8, 14]

$$I_{L\to R} = I_C \sin\left(\phi_L - \phi_R\right), \tag{2.4}$$

where we denote the phase of our left/right electrode with $\phi_{L/R}$. The critical current of the junction I_C characterizes the maximum tunneling current that can flow through, it depends on the area of the junction and on the details of the insulating barrier. Identifying the phase difference with a flux drop across the junction, via Eq. (2.3), allows us to interpret Eq. (2.4) as the constitutive relation of a non-linear inductor,

$$L(\varphi) = \Phi_0 \frac{\partial_t \varphi}{\partial_t I} = L_J \frac{1}{\cos\varphi} \tag{2.5}$$

with $\varphi = \phi_L - \phi_R$ and the inductance $L_J = \Phi_0/I_C$, usually called the Josephson inductance. We also define an energy scale $E_J = \Phi_0 I_C$ associated with the Cooper pair tunneling, called the Josephson energy of the junction. If we want to account for all the energy stored in a junction, we also have to consider the capacitance C_J formed by the junction, storing an electrostatic energy proportional to $(N_L - N_R)^2$. The full circuit representation of a junction is given Fig. 2.1. We define the differential variable $n = (N_L - N_R)/2$, conjugate to φ, so that the circuit Hamiltonian operator of a Josephson junction is compactly written as

$$\hat{\mathcal{H}}_{JJ} = 4E_C \hat{n}^2 - E_J \cos\hat{\varphi}, \tag{2.6}$$

where the charging energy is defined as $E_C = e^2/2C_J$. Identifying $\hat{\varphi}$ as a position operator, we recognize the Hamiltonian of a quantum particle evolving in a periodic potential.

2.2.2 Spectrum—Bloch bands

The Hamiltonian (2.6) alone is not enough to specify the eigenstates of the system, we also need to impose boundary conditions on our eigenfunctions $\psi(\varphi)$. Formally, the eigenfunctions of our system satisfy a Mathieu equation in the phase representation:

$$-4E_C\,\partial_\varphi^2\psi(\varphi) - E_J\cos(\varphi)\psi(\varphi) = E\,\psi(\varphi). \tag{2.7}$$

Since we are considering φ as an extended phase variable [see the comment after Eq. (2.3)] the correct choice is to enforce $\psi_q(\varphi + 2\pi) = e^{i\pi q/e}\psi_q(\varphi)$, in which case the spectrum will be composed of Bloch bands

$$\hat{\mathcal{H}}_{JJ} = \sum_s \int_{-e}^{e} \frac{dq}{2e}\,\epsilon_s(q)|q,s\rangle\langle q,s| \tag{2.8}$$

and the eigenvectors will be represented as the product between a plane wave and a 2π-periodic function $u_{q,s}(\phi)$,

$$\langle\varphi|q,s\rangle = \psi_{q,s}(\varphi) = e^{iq\varphi/e}u_{q,s}(\varphi), \tag{2.9}$$

indexed by a discrete band number s and a continuous quasi-momentum index $q \in (-e, e]$ [15] called the *quasi-charge*. We plot on Fig 2.2 an example of the spectrum $\epsilon_s(q)$ for several values of the ratio E_J/E_C. We see that, in the limit of large E_J/E_C, the bands flatten, suppressing the dispersion with respect to the quasi-charge. Moreover, the average spacing between the lower bands becomes almost constant with $\epsilon_{s+1}(q) - \epsilon_s(q) \approx \sqrt{8E_CE_J} \equiv \hbar\omega_p$ approximating the level spacing of a harmonic oscillator with resonant frequency ω_p, that we call the plasma frequency of the junction. This harmonic limit can be understood from the fact that the particle sits deep inside the cosine wells of the potential, thus its phase fluctuations become small compared to the periodicity, $\sqrt{\langle\hat{\varphi}^2\rangle} \ll 2\pi$. The cosine term of its Hamiltonian (2.6) can then be expanded perturbatively in phase around any minimum at $2\pi p$, $p \in \mathbb{Z}$,

$$\hat{\mathcal{H}}_{JJ} \approx 4E_C\hat{n}^2 + \sum_{p\in\mathbb{Z}} \frac{1}{2}E_J\,(\hat{\varphi} - 2\pi p)^2 + \mathcal{O}(\hat{\varphi}^4), \tag{2.10}$$

yielding a chain of parabolic wells with strongly suppressed tunneling between them. In this tight-binding limit the lower bands, those with $s\hbar\omega_p \ll E_J$, have a sinusoidal dispersion in quasi-charge with exponentially small amplitudes [7]

$$\epsilon_s(q) = s\hbar\omega_p + (-1)^{s+1}W_s\cos\left(\pi\frac{q}{e}\right), \tag{2.11}$$

$$W_s = \frac{1}{\sqrt{\pi}}\frac{2^{5s+3}}{s!}\hbar\omega_p\left(\frac{E_J}{\hbar\omega_p}\right)^{s+\frac{1}{2}}e^{-8\frac{E_J}{\hbar\omega_p}}. \tag{2.12}$$

Since the W_s correspond to the tunnel coupling between harmonic eigenstates of neighboring wells it is common to call W_s, especially for $s = 0$, the quantum phase slip (QPS) amplitudes.

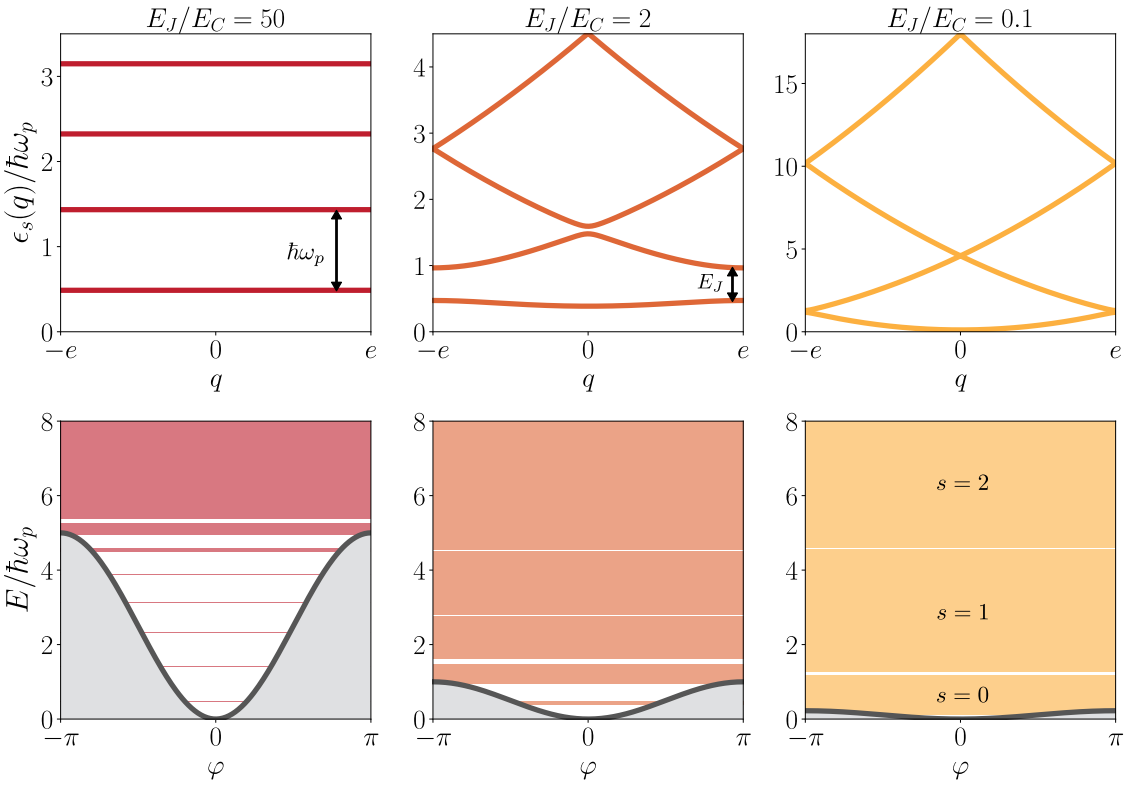

Figure 2.2: **Top row:** The first four Bloch bands of an isolated Josephson junction for varying E_J/E_C ratios while keeping the plasma frequency $\hbar\omega_p = \sqrt{8E_JE_C}$ constant. **Bottom row:** Visualization of the Bloch band widths (colored rectangles) superimposed on the Josephson potential $E_J(1-\cos\varphi)$ (gray), using the same parameters as in the top row. For the $E_J/E_C = 50$ case (left plot), the widths of the lowest bands are exaggerated for visibility, as they are exponentially suppressed.

In the opposite limit $E_J/E_C \ll 1$, the capacitive term of Eq. (2.6) dominates, and the Bloch bands of Fig. 2.2 become charge parabolas weakly coupled by the tunneling term, which opens a gap at their crossing points, of the order of $E_J(E_J/sE_C)^s$. This parabolic limit is also recovered at large energy $E \gg E_J$, no matter the ratio E_J/E_C, since it corresponds to the spectrum of a free particle ionized out of the cosine potential.

Let us define some useful operator representations in the Bloch band basis $|q, s\rangle$; all these expressions come directly from the usual theory of particles in a crystal potential [15, 16]. First, the phase operator $\hat{\varphi}$ can be split in two components

$$\hat{\varphi} = i2e\hat{\partial}_q + \hat{\varphi}^w. \tag{2.13}$$

The derivative operator with respect to q has its spectrum in $2\pi\mathbb{Z}$ since q is compact. This integer spectrum corresponds to the labelling of the wells of the $\cos\varphi$ potential, akin to the index p used in Eq. (2.10) [17]. With this, we can understand the operator $\cos(\pi\hat{q}/e)$ appearing in Eq. (2.11) as tunnel operators shifting φ by $\pm 2\pi$ and so describing the tunneling of flux quanta $2\pi\Phi_0$, called *fluxons*. The other component $\hat{\varphi}^w$ commutes with $\hat{q}$, is purely off-diagonal in s, and describes inter-band transitions. By opposition with $i2e\hat{\partial}_q$, this one corresponds to the intra-well phase variable with a compact spectrum in $]-\pi, \pi]$. Its matrix elements can be expressed with the $u_{q,s}$

functions of the Bloch wave decomposition (2.9)

$$\langle q,s|\hat{\varphi}^w|q',s'\rangle = i4e^2(1-\delta_{ss'})\delta(q-q')\int_{-\pi}^{\pi} d\varphi\, \overline{u}_{q',s'}(\varphi)\,\partial_q u_{q,s}(\varphi)\,, \tag{2.14}$$

with the overline denoting complex conjugation, and we kept the delta function $\delta(q-q')$ to emphasizes that $\hat{\varphi}^w$ is diagonal in the q-index. The voltage operator $\hat{V}$ is found by the time derivative of $\hat{\varphi}$

$$\hat{V} = \frac{1}{i2e}\left[\hat{\varphi}, \hat{H}_{JJ}\right], \tag{2.15}$$

yielding an operator diagonal in q but not in s:

$$\langle q,s|\hat{V}|q',s'\rangle = 2e\delta(q-q')\begin{cases}\partial_q\epsilon_s(q) & \text{if } s=s'\\ \frac{i}{2e}\left[\epsilon_s(q)-\epsilon_{s'}(q)\right]\langle q,s|\hat{\varphi}^w|q,s'\rangle & \text{if } s\neq s'\end{cases} \tag{2.16}$$

This also gives us the charge operator $\hat{Q}$ of the junction since it is simply related to the voltage through the capacitance of the junction, $\hat{Q} = C_J\hat{V}$.

2.2.3 Impedance of an isolated junction

Knowing the decomposition of various observables in the eigenbasis of our junction, we can easily compute its linear response, in particular its frequency dependent impedance $Z(\omega)$. To start, we will assume that the system is in an eigenstate of the first Bloch band $|q,0\rangle$[2] with the details of the calculation given in Appendix A. First, at high frequencies $\hbar\omega \gg E_J$ we recover the simple capacitive response of our junction

$$Z(\omega) \xrightarrow{\omega\to+\infty} \frac{1}{-i\omega C_J}. \tag{2.17}$$

However, at low frequencies $\hbar\omega \ll \epsilon_1 - \epsilon_0$ the junction behaves as a non-linear capacitor C_B in series with an inductor L_B:

$$Z(\omega) \xrightarrow{\omega\to 0} \frac{1}{-i\omega C_B(q)} - i\omega L_B(q). \tag{2.18}$$

The q-dependent capacitance is the inverse of the local curvature of the Bloch band

$$\frac{1}{C_B(q)} = \partial_q^2\epsilon_0, \tag{2.19}$$

while the inductance L_B encompasses the effect of the higher bands on the junction dynamics [20, 21]:

$$L_B(q) = \frac{\hbar^2}{2e^2}\sum_{s=1}^{+\infty}\frac{|\varphi^w_{0s}(q)|^2}{\epsilon_s(q)-\epsilon_0(q)}, \quad \varphi^w_{rs}(q) = \langle q,r|\hat{\varphi}^w|q,s\rangle. \tag{2.20}$$

The q-dependence of $1/C_B$ and L_B is plotted on figure 2.3. We see that in the large-junction limit the dependence disappears, while in the opposite limit $1/C_B$ and L_B strongly peak at the edges of the Brillouin zone. These behaviors can be

[2]Experimentally this can be achieved to a good degree by a charge offset produced in the junction through a voltage-biased capacitor at low temperature [18, 19].

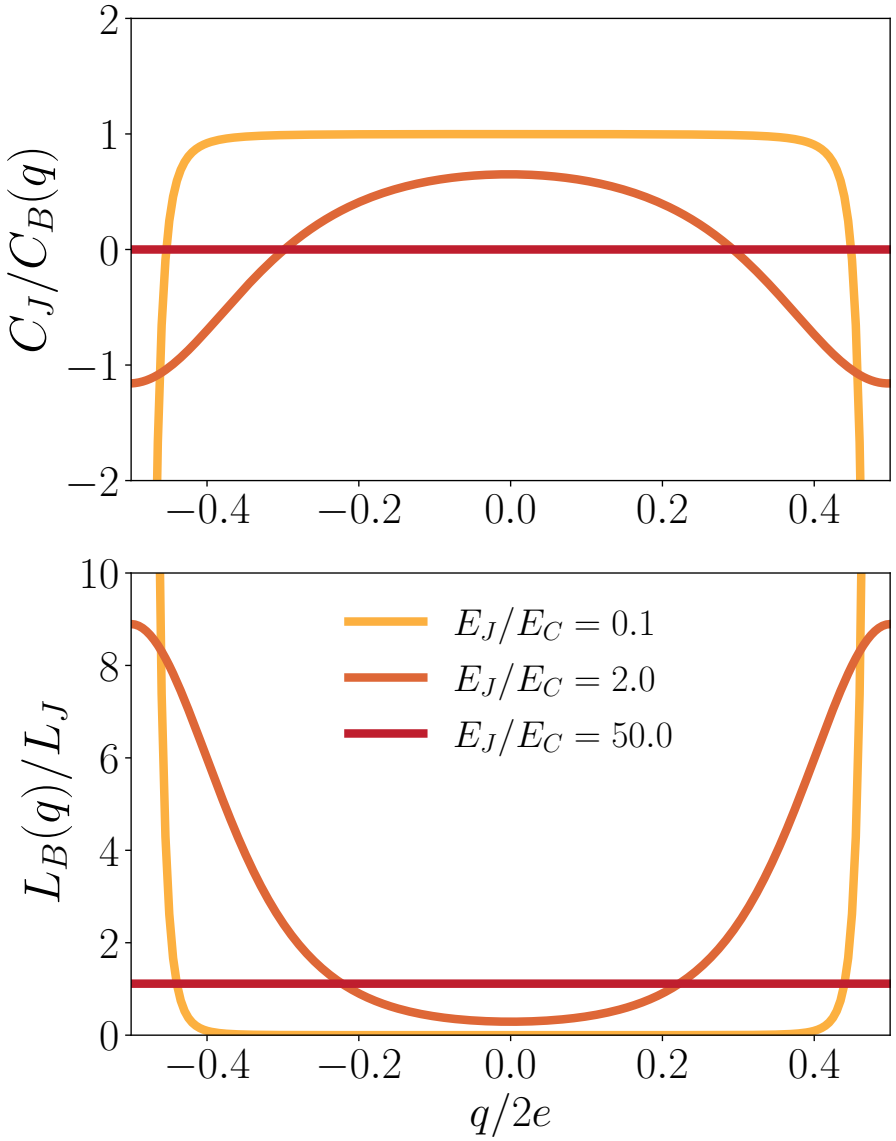

Figure 2.3: Dependence of $1/C_B(q)$ and $L_B(q)$ on the quasi-charge, computed using the sum rule (A.19) and Eq. (2.20), for different E_J/E_C ratios. For $E_J/E_C = 50$, the non-linear capacitive response is strongly suppressed, the inductance loses its quasi-charge dependence, and we recover the classical limit $L_B = L_J$. On the contrary, at $E_J/E_C = 0.1$ the inductance rises to large values at the Brillouin zone edges $L(q = \pm e) \sim 10^3\, L_J$ due to the small gap with the second band there.

readily explained analytically: in the limit $E_J/E_C \gg 1$, the matrix elements $|\varphi^w_{rs}(q)|$ lose their q-dependence and take the form of the position operator for a harmonic oscillator [7]

$$|\varphi^w_{rs}(q)| \approx \left(\frac{2E_C}{E_J}\right)^{\frac{1}{4}} \left(\sqrt{s+1}\delta_{r+1,s} + \sqrt{s}\delta_{r-1,s}\right), \tag{2.21}$$

such that Eq. (2.20) reduces to the usual Josephson inductance relation $L_B(q) = L_J = \Phi_0^2/E_J$, since $\epsilon_1 - \epsilon_0 = \hbar\omega_p$.

In the small-junction limit, $E_J/E_C \ll 1$, L_B and $1/C_B$ are strongly modulated by the quasi-charge. Indeed, the first band is parabolic almost everywhere, so that $C_B = C_J$ except at the Brillouin zone edges where $\epsilon(q)$ quickly changes sign, forcing $1/C_B$ to go deep in the negative. Conversely, the inductive response L_B is strongly suppressed for most of the Brillouin zone because close to $q = 0$ the matrix elements φ^w_{rs} reduce to [7]

$$|\varphi^w_{rs}(0)| \approx \frac{E_J}{E_C}\left[\frac{1}{(2r+1)^2}\delta_{r+1,s} + \frac{1}{(2r-1)^2}\delta_{r-1,s}\right]. \tag{2.22}$$

In addition, we have $\epsilon_1(0) - \epsilon_0(0) = 4E_C$, and thus

$$L_B(0) = \frac{1}{2}L_J\left(\frac{E_J}{E_C}\right)^3 \ll L_J. \tag{2.23}$$

Finite temperature does not really change the calculations made in the appendix; the found expressions should be integrated over the Brillouin zone with a Boltzmann weight $e^{-\epsilon_s(q)/k_BT}$. We will not address all possible cases, but one insightful scenario arises when E_J/E_C is large, and $W_0 \ll k_BT \ll \epsilon_1 - \epsilon_0$. In this limit, the expression for the low frequency limit of the impedance is modified as[3]

$$Z(\omega) = \int_{-e}^{e} \frac{dq}{2e}\, e^{-\frac{1}{k_BT}\epsilon_0(q)}\left[\frac{1}{-i\omega C_B(q)} - i\omega L_B(q)\right]. \tag{2.24}$$

The Boltzmann factor can be assumed constant over the whole Brillouin zone since $W_0 \ll k_BT$; as such the capacitive response of the junction vanishes because $1/C_B = \partial_q^2\epsilon_0$[4]. However, L_B does not change sign [see Eq. (2.20)], so its integral over the Brillouin zone does not vanish. Since the inductive response corresponds to intra-well dynamics in the $\cos\varphi$ potential, it is robust as long as $E_J \gg k_BT$, whereas the coherent coupling W_0 between wells is easily washed out. As such, observing experimental signatures of $C_B(q)$ requires low temperatures and careful tuning of E_J/E_C[5]. Moreover, this capacitive response is only seen below the characteristic frequency $1/\sqrt{L_BC_B}$ which, for big junctions, is exponentially small due to Eq. (2.11). However, no matter the temperature and the ratio E_J/E_C, there is always a capacitive contribution, even if on paper it is minuscule, that dominates at low frequencies such that $Z(\omega \to 0) \to +\infty$. This can be understood in the picture of the Schmid transition, that we will discuss rapidly in Section 2.3.5, where an isolated junction is considered an insulator [13, 22]. This zero-frequency divergence is a signature of that.

[3] We omit the normalization coming from the partition function $\mathcal{Z}$.

[4] At first order in W_0/k_BT we would get something like $1/C_B \propto \frac{1}{k_BT}\int(\partial_q\epsilon_0)^2dq$.

[5] Here we mean the non-linear part of C_B since one can easily make a pure capacitor with $E_J \approx 0$ but without any quasi-charge dispersion.

2.3 Dynamics of a junction coupled to an environment

2.3.1 Coupling between the junction and the environment

The non-linearity provided by the Josephson junction has allowed physicists to implement and study a multitude of quantum systems; even coupling a junction to just a few electromagnetic modes has enabled the manipulation of qubits [23, 24], implementations of strong-light matter interactions [25, 26], and even realizations of fundamental tests of quantum mechanics [27–30]. However, in this thesis we will be interested in the study of a junction coupled to a dissipative environment containing a large number of harmonic modes. At the linear level this environment is modeled as a frequency dependent admittance $Y(\omega)$, or equivalently as an impedance $Z(\omega) = 1/Y(\omega)$, whose real part is non-zero. The Hamiltonian describing the system "junction+bath" is written in the Caldeira-Leggett fashion [5, 31]:

$$\hat{\mathcal{H}} = \sum_m \frac{1}{2}\left(\hat{p}_m - g_m\hat{\varphi}\right)^2 + \frac{1}{2}\omega_m^2\hat{x}_m^2 + 4E_C\hat{n} - E_J\cos\hat{\varphi}, \tag{2.25}$$

with the operators $\{\hat{x}_m, \hat{p}_m\}$ representing the coordinates of the bath. The coupling constants g_m are linked to the admittance Y through (see Appendix B for details)

$$g_m = \frac{\hbar}{2e}\sqrt{\frac{2\mathrm{Re}\left[Y(\omega_m)\right]\Delta\omega_m}{\pi}}, \tag{2.26}$$

where $\Delta\omega_m = \omega_{m+1} - \omega_m$ is the frequency spacing of the bath oscillators at frequency ω_m. Here we chose to couple the bath to the junction through the phase operator, but another popular choice is to translate $\hat{p}_m$ by the unitary transformation[6]

$$\hat{\mathcal{U}} = \exp\left(i\sum_m g_m\hat{x}_m\hat{\varphi}\right), \tag{2.27}$$

and put the coupling in the $\hat{n}$ operator

$$\hat{\mathcal{H}} = \sum_m \frac{1}{2}\hat{p}_m^2 + \frac{1}{2}\omega_m^2\hat{x}_m^2 + 4E_C\left[\hat{n} - \sum_m g_m\hat{x}_m\right]^2 - E_J\cos\hat{\varphi}. \tag{2.28}$$

Both prescriptions are valid, but in our case we will stick with the former when dealing with the dissipative quasi-charge dynamics in the following sections, because of convenience. There are two main ways to probe our system: either by a current bias, in which case the admittance shunts the junction, or by voltage bias, where the impedance is in series with the junction. We depict the two cases in Fig. 2.4. We should stress that these bias schemes are completely equivalent and map onto each other through the Thévenin-Norton transformation (a derivation is given in Appendix C)

$$V(\omega) = Z(\omega)I(\omega), \tag{2.29}$$

[6] In principle, we do not have to translate all the p_m, we could only pick a subset of bath frequencies and end up in a mixed coupling configuration. This is unwarranted in our case, but when dealing with numerics this technique can yield a more efficient truncation of the Hilbert space, see e.g. Ref. [32].

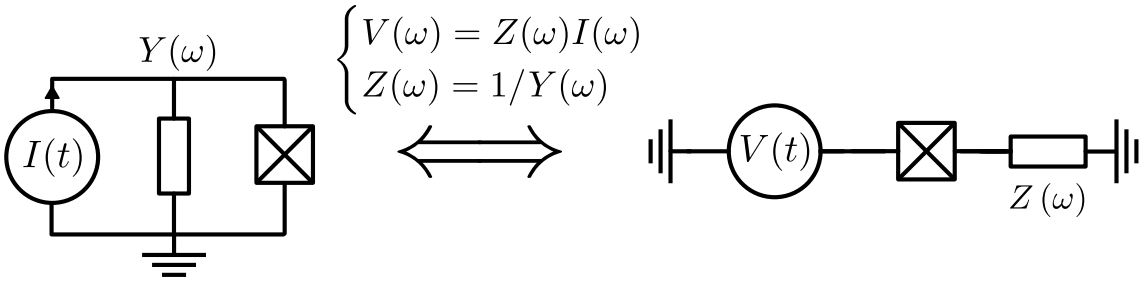

Figure 2.4: Equivalence between current bias (left) and voltage (right) due to the Thévenin-Norton transformation.

where $V(\omega)$ and $I(\omega)$ are the Fourier transform of the biases. As such, we will freely switch between the two configurations in the rest of the manuscript. For now, we postpone the discussion on how to implement such bath experimentally until Section 2.4; we assume it has been implemented in some way and describe a few phenomena that can take place in this type of circuit.

2.3.2 Bloch oscillations

Let us start with a junction shunted by a pure resistor R under an external DC current bias I_0. We will assume that the resistor behaves as a good dissipative bath for the junction, with the following conditions

- There is no entanglement between the junction and the environment so that the total density matrix is separable $\hat{\rho}_{tot} = \hat{\rho}_{JJ} \otimes \hat{\rho}_{env}$. This is a good approximation if we are far from the Schmid transition $R \gg R_Q$, with $R_Q \equiv h/(2e)^2 \approx 6.45\,\mathrm{k\Omega}$ (see subsection 2.3.5).
- Its internal state is considered thermal at all times and remains unaffected by the dynamics of the junction.

The quantum Langevin equation for the quasi-charge operator $\hat{q}$ is (see Appendix B for the derivation)

$$\dot{\hat{q}} = I_0 + \tilde{I} - \frac{1}{R}\hat{V}, \tag{2.30}$$

with $\hat{V}$ the voltage operator defined by Eq. (2.16) and $\tilde{I}$ is a random variable corresponding to the Johnson-Nyquist current noise of the resistor defined by the moments

$$\langle \tilde{I}(t) \rangle = 0, \tag{2.31}$$

$$\langle \tilde{I}(t)\tilde{I}(0) \rangle = \int_0^{+\infty} d\omega\, \hbar\omega \frac{1}{\pi R} \left[\coth\left(\frac{\hbar\omega}{2k_B T}\right) \cos\omega t - i \sin\omega t \right]. \tag{2.32}$$

To simplify the right-hand side of Eq. (2.30) let us first suppose that the system stays confined in the first Bloch band so that $\hat{V} \approx \partial_q \epsilon_0(\hat{q})$, and that the fluctuations (quantum or stochastic) of the quasi-charge are small allowing $\langle \partial_q \epsilon_0(\hat{q}) \rangle \approx \partial_q \epsilon_0(\langle \hat{q} \rangle)$. If we also suppose that E_J/E_C is big enough as to make Eq. (2.11) valid, we get[7]

$$\dot{q} = I_0 - \frac{\pi W_0}{eR} \sin\left(\frac{\pi}{e} q\right). \tag{2.33}$$

[7] We use the notation $q = \langle \hat{q} \rangle$.

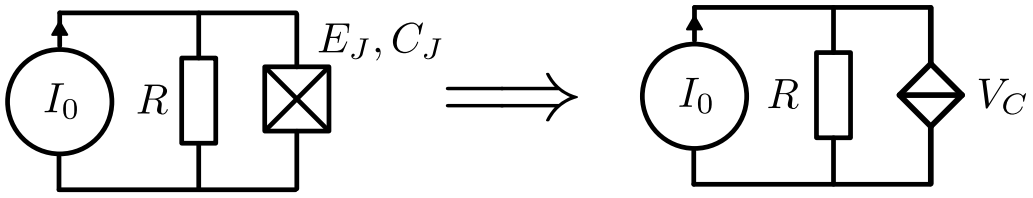

Figure 2.5: In the single band approximation, we can replace a current biased small Josephson junction(left) with a Quantum Phase Slip element, dual to the junction (right).

This is the equation of motion of a strongly damped charge particle evolving in the washboard potential $U(q) = -RI_0 q - W_0 \sin(\pi q/e)$, exactly dual of the equation of a "phase-classical" Josephson junction in series with a small resistor under an external voltage bias. The circuit depiction of the dual circuit is given in Fig. 2.5, the dual element to a Josephson junction, that we call a Quantum Phase Slip (QPS) element, is depicted by a diamond shape. Drawing from this duality, we can derive two regimes for the solution $q(t)$ of Eq. (2.33). If the current is small enough, we have a solution at a fixed quasi-charge defined by $\dot{q} = 0$ and thus [33]

$$q = \frac{e}{\pi} \arcsin\left(\frac{e}{\pi W_0} R I_0\right). \tag{2.34}$$

In this regime all the current I_0 flows through the shunting resistor and the voltage across the junction is just $V = RI_0$, such that the current source is effectively voltage biasing the junction. The tunneling current is suppressed due to the electrostatic term $E_C \hat{n}^2$ in the Hamiltonian, so this regime corresponds to the Coulomb blockade of the Josephson junction. If now the current exceeds the threshold value $I_{thr} = \pi W_0/eR$, the equation $\dot{q} = 0$ has no solutions, and our charge particle runs downs the washboard potential. This also means that the voltage cannot exceed the value $V_C = RI_{thr}$. By analogy with classical junctions we call V_C the *critical voltage* of the junction. It is an intrinsic property of the junction[8], and is defined by the maximal slope of the first Bloch band

$$V_C = \max\left[\partial_q \epsilon_0(q)\right] \overset{E_J \gg E_C}{=} \frac{\pi W_0}{e}. \tag{2.35}$$

In the running state the voltage oscillates with a frequency ω_B proportional to the current I flowing through the junction (which is not necessarily I_0) [7]

$$\omega_B = \frac{\pi}{e} I. \tag{2.36}$$

These are called *Bloch oscillations*, as they are completely analogous to the solid state phenomenon involving electrons in a periodic potential subject to a constant force. For a Josephson junction the Bloch oscillations are just the dual of the usual Josephson oscillations that one obtains when voltage biasing a junction. They can also be understood as the periodic charging and discharging of the junction [7]. This picture makes most sense in the small junction limit $E_J/E_C \ll 1$, where the bands are quasi-parabolic (see Fig. 2.2); in this limit the charge on the junction $Q = C_J V = C_J \partial_q \epsilon_0$ is equal to q everywhere except close to Brillouin zone edges.

[8] Whereas the threshold current depends on R.

When the current bias forces q to cross the edge, Q quickly changes sign and shifts by $2e$. We identify this shift with a Cooper pair tunneling event discharging the junction.

The current I in Eq. (2.36) can be obtained by integrating Eq. (2.33) to find the period $T = 2e/I$ over which q increase by $2e$. This gives again a dual result as the one obtained from classical phase dynamics [8, 33]:

$$I = \frac{1}{R}\sqrt{(RI_0)^2 - V_C^2}. \tag{2.37}$$

Concerning the effects of current fluctuations $\tilde{I}$, they are also dual to the ones observed in classical junctions, as long as the energy scales involved are smaller than the band gap $\epsilon_1 - \epsilon_0$. First, the critical voltage is affected by quantum and thermal fluctuations. In the zero temperature limit, the zero point motion of the bath renormalizes V_C according to [13]

$$V_C^\star = V_C \left(\frac{W_0}{\hbar\omega_p}\right)^{\frac{\alpha}{1-\alpha}}, \tag{2.38}$$

with $\alpha = R_Q/R$. At finite temperatures we can reuse the results of Ambegaokar & Halperin [34] to obtain the impact of thermal fluctuations on the IV characteristic.

The spectrum of the oscillations is also impacted. A perturbative approach in W_0[9] gives an asymmetric voltage noise spectral density $S_{VV}(\omega)$ at zero temperature, which can diverge as a power law close to ω_B [36–38]:

$$S_{VV}(\omega) \overset{\omega\to\omega_B}{\propto} \frac{V_C^2}{\omega_p}\left(\frac{\omega_B - \omega}{\omega_p}\right)^{2\alpha-1} \theta\left(\omega_B - \omega\right), \tag{2.39}$$

where θ is the Heaviside step function. At higher temperatures, the emission symmetrizes and approaches a Gaussian shape,

$$S_{VV}(\omega) \propto \exp\left[-\frac{\hbar}{4\pi\alpha k_B T\omega_p}\left(\omega_B - \alpha\omega_p - \omega\right)^2\right]. \tag{2.40}$$

Between these two limits, the spectrum interpolates smoothly.

Higher bands do impact the quasicharge dynamics in several ways. First, as we have seen in the preceding subsection [see Eq. (2.18)], the presence of the higher bands induce an inductive part in the low frequency response of the junction. This inductance L_B adds an effective mass term to the motion of our particle in the first band, such that Eq. (2.33) acquires an additional term of the form $L_B(q)\ddot{q}$ [20]. This addition is valid as long as the Bloch frequency is low enough as to make Eq. (2.18) valid. In the case $E_J \gg E_C$, this means $\omega_B \ll \omega_p$, and additionally we have $L_B(q) \sim L_J$. With this mass term, we end up with the complete dual of the usual RCSJ equations under current bias [33]

$$L_J\ddot{q} + R\dot{q} + V_C \sin\left(\frac{\pi}{e}q\right) = RI_0, \tag{2.41}$$

and can reuse all the theoretical treatments from it. The characteristic frequency of this equation, dual to the plasma frequency of a junction, is now

$$\omega_q = \sqrt{\frac{\pi V_C}{eL_J}}. \tag{2.42}$$

[9] Using the $P(E)$ framework [35], discussed in the following subsection 2.3.4.

If $R/L_J \gg \omega_q$, we recover the overdamped limit of the RCSJ model and all the above derivations still hold because we can neglect the mass term. In the opposite underdamped limit, $R/L_J \ll \omega_q$, the IV curve becomes hysteretic and presents a discontinuity [20, 33, 39]. Moreover, this inductive term can filter out the noise $\tilde{I}$ coming from the resistor so that if the cutoff frequency $\omega_{RL} = R/L_J$ becomes smaller than ω_p, one should replace ω_p in Eqs. (2.38), (2.39), and (2.40) by ω_{RL}.

When $E_J \ll E_C$, the dual RCSJ model of Eq. (2.41) is not suited since $L_B(q)$ strongly varies with q. As seen on Fig. 2.3, it is negligible in most of the Brillouin zone except close to the crossing points where it peaks. This signals that the dynamics are best described in terms of Landau-Zener transitions happening when the quasicharge crosses these points at the fixed velocity $e\omega_B/\pi$. The probability to transition to the second band is given by [40]

$$P_Z = \exp\left(-\frac{\pi}{8}\frac{E_J^2}{E_C\hbar\omega_B}\right). \tag{2.43}$$

As soon as this probability becomes appreciable, the system evaporates to the higher bands, since the band gaps are smaller in the higher bands, and the oscillations are spoiled. Interestingly, dissipation will counteract these transitions by inducing random decays back down, helping to stabilize Bloch oscillations beyond the $\hbar\omega_B = E_J^2/E_C$ point, albeit with reduced coherency [41, 42].

If $E_J \gg E_C$ now, the standard Landau-Zener formula does not really apply since the band gap is bigger than the bandwidth, so P_Z is negligible. However, an interesting resonant transition can occur when $\omega_B \approx \omega_p$. As illustrated on figure 2.6, this corresponds to the current bias which align the harmonic levels of the $\cos\varphi$ potential, giving an enhancement of the tunneling between them [11, 43]. We can also see this as the junction driving itself resonantly through Bloch oscillations and undergoing a transmon-like excitation. After a tunneling event between wells, the system can relax downwards or continue to tunnel, meaning further excite to higher bands, producing a voltage peak in IV curve or even switching to the resistive state [44]. The expected impact of this resonant Zener process on Bloch oscillations is mainly to destroy their coherence, as such $\omega_B < \omega_p$ should be enforced[10].

At intermediate ratios $E_J/E_C \sim 1$ a hybrid situation should occur. The transitions to higher bands should be describable in terms of Landau-Zener or resonant tunneling, perhaps with some correction coming from the higher harmonics of the band profile. In any case, the Landau-Zener condition $\hbar\omega_B \ll E_J^2/E_C$ and the resonant condition $\hbar\omega_B \ll \epsilon_1 - \epsilon_0 \approx E_J$ yield similar bounds since $E_J/E_C \sim 1$.

To conclude this part on Bloch oscillations we recapitulate the main conditions for these oscillations to occur experimentally. First, the ratio E_J/E_C should be big enough as to make gap to the second band big enough with regard to ω_B and T but also small enough as to maximize V_C. The best compromise seems to be $2 \leq E_J/E_C \leq 10$ [7]. Second, the temperature should obviously be as low as possible in order to suppress thermally activated transitions to the higher bands $k_BT \ll \epsilon_1 - \epsilon_0$. More constraining is the condition to have a sufficiently narrowband observable spectrum; this can found from Eq. (2.40):

$$\sqrt{k_BT\hbar\omega_p} \ll \hbar\omega_B. \tag{2.44}$$

[10] Whether there exists Bloch oscillations when $\omega_p < \omega_B < 2\omega_p$ is an interesting question which has yet to be addressed.

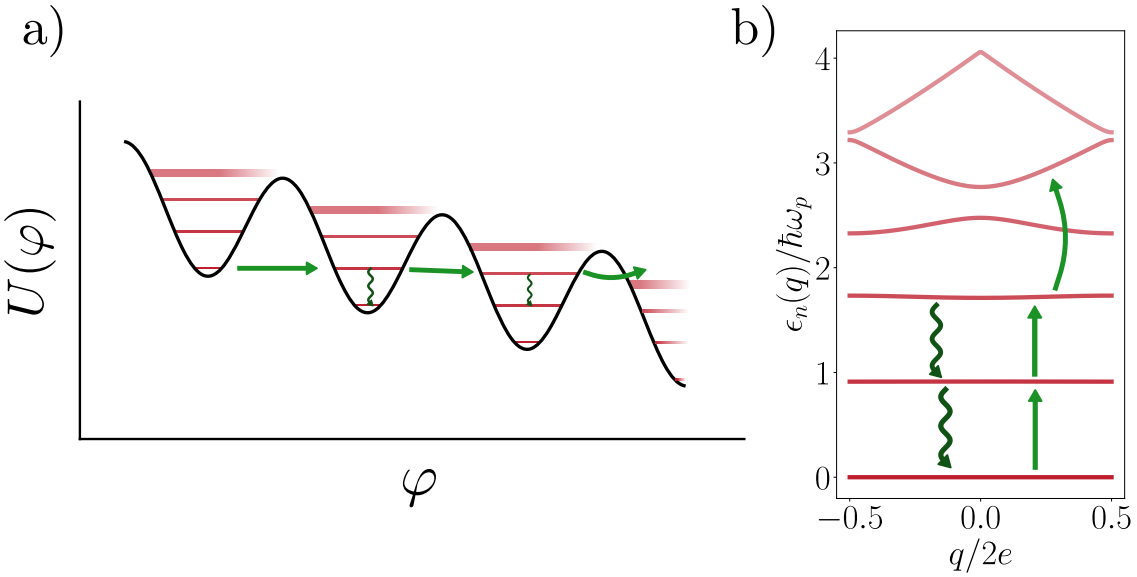

Figure 2.6: Illustration of the resonant Zener process in the tilted phase washboard potential (a) and in the Bloch band spectrum (b). When the current bias matches the energy spacing of the bands $I\Phi_0 \sim \hbar\omega_p$ the system can self-excite to higher bands through resonant tunneling (straight arrows). Then, it can decay back (wiggly arrows), due to dissipation, or continue tunneling and eventually escape into the free particle states (curved arrow).

This condition can be eased with the use of a series inductance, either the "intrinsic" one L_B, or an external one, in series with the resistor R to filter out thermal fluctuations. With this, the condition is

$$\sqrt{k_B T \hbar \frac{R}{L}} \ll \hbar\omega_B, \tag{2.45}$$

which can be easier to achieve experimentally. The choice of the resistance value R can be subtle. Justifying the classical approximation made for equation (2.33) requires $R \gg R_Q$, and the higher the resistance the smaller the emission linewidth according to Eqs. (2.39) and (2.40). However, the decay rate from the higher bands to the first one scale as $\Gamma_{s\to 0} \propto R_Q/R$[11], so dissipation can help stabilize the system in the lowest band when Landau-Zener transitions are important. Thus, in the case $E_J < E_C$, there exists an experimental trade-off on R by imposing $P_Z < \Gamma_{s\to 0}$, see Refs. [41, 42] for a more detailed study. If $E_J > E_C$, this constraint should be less stringent since the transitions to higher bands are negligible for a wide range of current, and so any finite R stabilizes the system in the lowest band, for low currents. At the time of writing, direct experimental observation of Bloch oscillations in Josephson junctions is still lacking. However, a great deal of effort has been put towards observing a secondary effect linked to it: the dual Shapiro steps.

[11] This can be found by applying Fermi Golden rule to the operator $\sum_m g_m \hat{p}_m \hat{\varphi}$ in Hamiltonian (2.25).

2.3.3 Dual Shapiro steps

The dual Shapiro steps are a consequence of the phase locking of the Bloch oscillations under an external finite frequency drive. For now, we place ourselves in the regime $E_J > E_C$ and consider the same circuit as for the Bloch oscillations, to which we add a harmonic drive and an unspecified inductance L representing any series inductance be it L_B or an external one. The equation of motion of the quasicharge for this circuit is [39]

$$L\ddot{q} + R\dot{q} + V_C \sin\left(\frac{\pi}{e}q\right) = V_0 + V_{ac}\cos\omega_{ac}t. \tag{2.46}$$

where we put the equivalent dc voltage bias $V_0 = RI_0$. The two characteristic frequencies of this system have already appeared in the discussion on Bloch oscillations: $\omega_q = \sqrt{\pi V_C/eL}$ is the inertial frequency, dual to the plasma frequency in Josephson junction, and R/L is the damping rate due to the resistor, dual to the $1/RC$ frequency in junctions. We solve Eq. (2.46) numerically and plot the obtained IV curve on Fig. 2.8. We clearly see the appearance of current plateaux satisfying the relation

$$I_n = n\frac{e}{\pi}\omega_{ac},\ n \in \mathbb{Z}. \tag{2.47}$$

These plateaux are the dual Shapiro steps, named after the usual Shapiro steps occurring in classical Josephson junction dynamics which are voltage plateaux whose heights follow the relation $V_n = n\hbar\omega/2e$.

The intuition behind the "quantization" of these plateaux is shown on Fig. 2.7 and is as follows. Eq. (2.46) describes the evolution of a classical particle in a tilted washboard potential, with the drive making the tilt periodic in time. Now, let us assume that the particle is trapped in one of the potential wells at the start of a drive cycle [$t = \pi/2$ in Eq. (2.46)]. Once the drive ramps up, the particle can escape the well and starts to run down the potential. Then, when the drive tilts the potential back in the other direction, the particle retraps itself in one of the wells. Thus after one full drive the particle will have advanced an integer number n of wells, such that its time-averaged velocity is

$$\langle\dot{q}\rangle = n\frac{P}{T},\ n \in \mathbb{Z}, \tag{2.48}$$

where P is the periodicity of the potential (in our case $2e$) and T is the drive period. To see why this synchronization happens we first take the overdamped limit of Eq. (2.46) with $R/L \gg \omega_d$, yielding

$$R\dot{q} = -V_C \sin\left(\frac{\pi}{e}q\right) + V_0 + V_{ac}\cos\left(\omega_{ac}t\right). \tag{2.49}$$

We know that the locking corresponds to $\dot{q}$ satisfying Eq. (2.47), as such we can define the differential variable

$$\delta q_n = q - n\frac{e}{\pi}\omega_{ac}t - \frac{V_{ac}}{R\omega_{ac}}\sin\omega_{ac}t. \tag{2.50}$$

The goal of δq_n is to quantify the distance to the locked solution for the plateau of order n, so that if $\delta q_n(t) \to \infty$ the system is not locked, and if $\delta q_n(t) \to$ const. the system follows the drive (with a constant phase difference). The equation of motion is obtained by transforming Eq. (2.49):

$$R\delta\dot{q}_n = \Delta V_n - V_C \sin\left(\frac{\pi}{e}\delta q_n + n\omega_{ac}t + a\sin\omega_{ac}t\right) \tag{2.51}$$

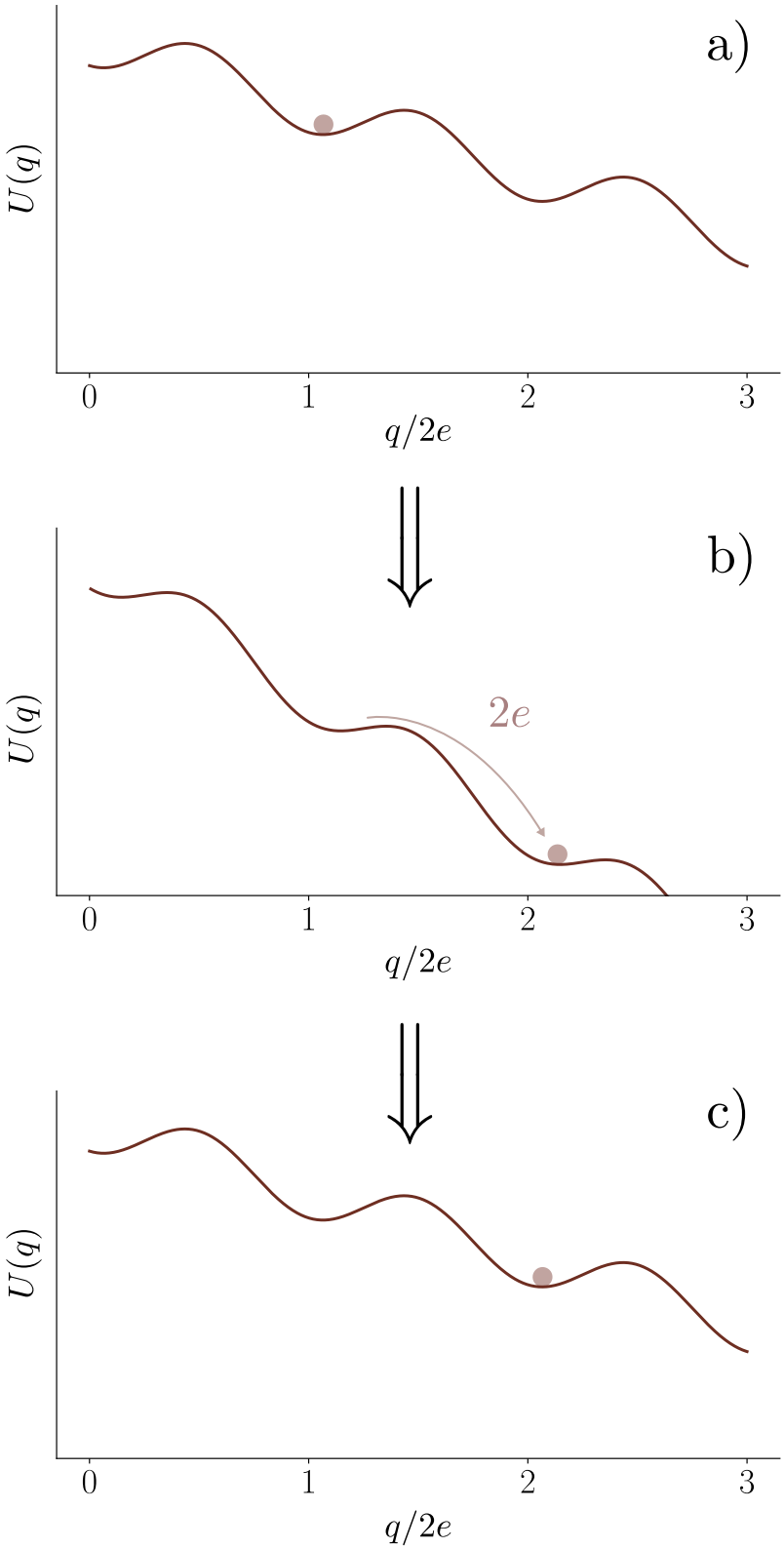

Figure 2.7: Illustration of the phase locked movement of the charge particle when on a step of order $n = 1$. At the start of the drive cycle (a) the particle is trapped in a minimum, due to the tilt when the drive is maximum it rolls down to the next minima (b) and then retraps here when the drives tilts back (c).

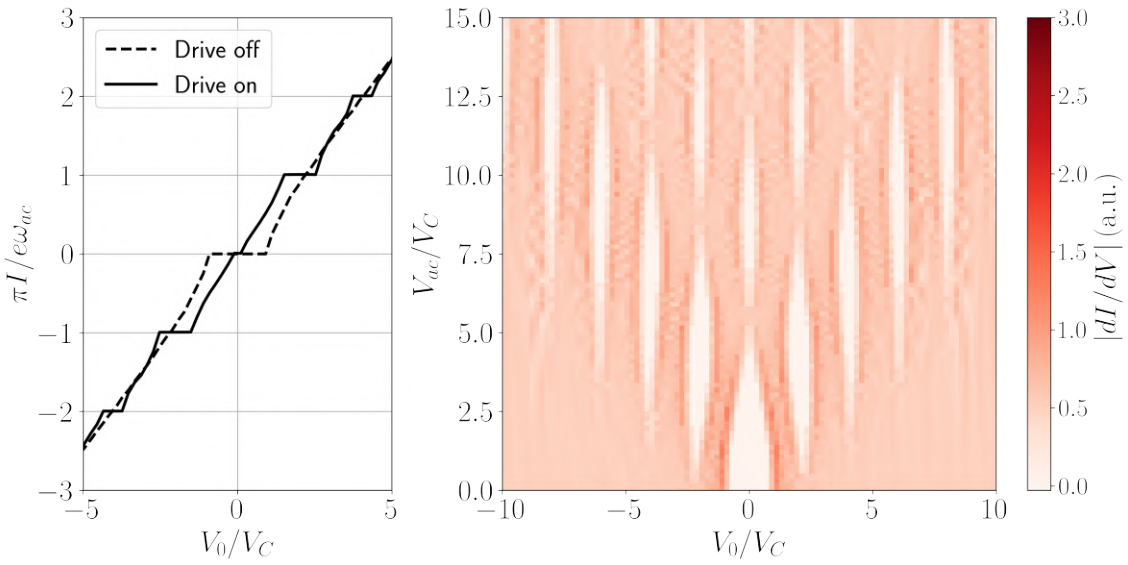

Figure 2.8: Left: IV curve obtained by solving numerically Eq. (2.46) for $R\sqrt{e/\pi V_C L} = 2$, $\omega_{ac}\sqrt{eL/\pi V_C} = 1$ with $V_{ac} = 0$ (dotted) and $V_{ac} = 5V_C$ (full line). Right: 2D plot of the differential conductance of the IV curves obtained by solving Eq. (2.46) for the same parameters as for the left plot but with varying drive strength V_{ac}.

where we use the shorthand notations

$$\Delta V_n = V_0 - n\frac{eR}{\pi}\omega_{ac}, \quad a = \frac{\pi V_{ac}}{eR\omega_{ac}}, \tag{2.52}$$

to make things more compact. To simplify the sine expression we make use of the Jacobi-Anger relation

$$e^{iz\sin\theta} = \sum_{k\in\mathbb{Z}} J_k(z)e^{ik\theta}, \tag{2.53}$$

where J_k is the k-th Bessel function of the first kind. This gives us

$$R\delta\dot{q}_n = \Delta V_n - V_C \sum_{k\in\mathbb{Z}} J_k(a)\sin\left[\frac{\pi}{e}\delta q_n + (n+k)\omega_{ac}t\right]. \tag{2.54}$$

Since we are only interested in the long-time behavior of δq_n, we average Eq. (2.54) over time and only retain the terms which do not oscillate, that is the term $n+k=0$ for the sum. This is valid as long as $\omega_{ac} \gtrsim \pi V_C/eR$ [33]. We end up with

$$R\delta\dot{q}_n = \Delta V_n - (-1)^n J_n(a)V_C \sin\left(\frac{\pi}{e}\delta q_n\right) \tag{2.55}$$

which is almost exactly the equation (2.33) we had in the case of a purely dc biased overdamped QPS element. The difference is that ΔV_n now represents the dc bias with respect to the center of the n-th step and the amplitude of the potential is renormalized by a Bessel function dependent on the drive strength. Since the equations are the same, all the treatments made in the preceding section follows: if $|\Delta V_n| < J_n(a)V_C$ there exists a solution with $\delta\dot{q}_n = 0$ and the system is locked to the drive. Outside this, $\delta\dot{q}_n$ enters the running state, it does not synchronize, and the plateau ends. This directly tells us that the plateau widths vary as a Bessel function

of the drive power. This is verified on Fig. 2.8 where we plot the dI/dV obtained by solving Eq. (2.46) with varying drive strengths. The ovals corresponding to the step modulation with power are called Arnold's tongues in synchronization theory [45]. Equation (2.55) can be seen as a kind of Adler's equation as well. When leaving a step, the system undergoes a cascade of period-doubling bifurcations before transitioning to chaotic motion between the steps [46, 47].

The similarity of Eq. (2.55) with the undriven one also allows us to predict how the steps will be affected by fluctuations by reusing the results without drive[12]. For example, the zero-point fluctuations will renormalize the step size according to Eq. (2.38), again imposing $R \gg R_Q$. Finite temperature will give steps a finite slope given, close to the step center $\Delta V_n = 0$, by [34]

$$\frac{dI}{dV} = \mathcal{I}_0 \left[\frac{eV_C}{\pi k_B T} J_n(a) \right]^{-2}, \tag{2.56}$$

here $\mathcal{I}_0$ is the modified Bessel function of the first kind. This gives an upper bound on the temperature if one wants to observe a flat n-th step [48]

$$\frac{\pi k_B T}{eV_C} < \max J_n(a) \approx 0.68\, n^{-1/3}. \tag{2.57}$$

Outside the overdamped regime, we need to take into account the finite inductance L. This can be done by changing the definition (2.50) so as to absorb the differential operator $L\partial_t^2 + R\partial_t$ from the left-hand side of Eq. (2.46), giving the transformation

$$\delta q_n = q - n\frac{e}{\pi}\omega_{ac} t + \frac{V_{ac}}{R^2 + L^2\omega_{ac}^2} \left(L\cos\omega_{ac} t - \frac{R}{\omega_{ac}} \sin\omega_{ac} t \right). \tag{2.58}$$

Then, one should reinject this expression inside the sine, expand it in harmonics, and average out the oscillating terms. We will not go into details for the sake of simplicity, but we mention that in the underdamped regime the steps overlap in the IV curve [39]. This can lead to chaotic transitions at high power in the overlapping regions [47].

In Eq. (2.46), we assumed that the QPS voltage-charge relation was purely sinusoidal, which is only true if $E_J/E_C \gg 1$, but this does not really affect the dual Shapiro steps. Indeed, the quantization of the steps relies only on the periodicity of the potential U (and of the drive), not its exact shape. However, in the general case, the modulation with respect to power will not be a Bessel function. For an arbitrary periodic function $f(q) = \partial U/\partial q = \sum_k c_k e^{ikq}$ appearing in the equation of motion, the Jacobi-Anger expansion (2.53) needs to be replaced by

$$f(a\sin\omega t - n\omega t) = \sum_{k,\, m\in\mathbb{Z}} c_k J_m(ak) e^{i(m-kn)\omega t}, \tag{2.59}$$

which allows steps of fractional order for $n = m/k$, but all the calculations follow similarly as for the case of sinusoidal Bloch bands.

Finally, the bounds coming from the transition to higher bands are sensibly the same as for Bloch oscillations. The main difference is the presence of the drive such that intuitively we should have

$$\hbar\omega_{ac} \ll \epsilon_1 - \epsilon_0. \tag{2.60}$$

[12] This works well as long as the characteristic frequencies of the fluctuations are small compared to ω_{ac}.

The impact of the drive strength V_{ac} on these transitions has not been studied in the context of dual Shapiro steps. However, in the quasi-harmonic regime $E_J > E_C$, we can roughly estimate that drive induced transitions will be suppressed in a Rabi fashion so that the probability to transition from the lowest band to the first one would be given by

$$P_{0\to 1} \sim \frac{V_{ac}^2}{V_{ac}^2 + (\epsilon_1 - \epsilon_0 - \hbar\omega_{ac})^2/e^2}. \tag{2.61}$$

This would indicate that we could even drive at frequencies placed between the bands, although to reach the steps in the IV curve we would need to cross through the resonant Zener region described in the previous section. Whether the locking can happen in these conditions is unclear, and thus we are probably better off using the condition (2.60) as a strict inequality. A more precise modeling of the bands' impact could be done in the same fashion as the quasiparticle states are taken into account for the usual Shapiro steps (and Josephson effect). This is done by introducing a frequency-dependent critical current $I_C(\omega)$, which encompasses the singularity at the gap edge (the so-called Riedel peak), and by applying the Tien-Gordon formula [49, 50]. In any case, a more complete theoretical analysis done in Ref. [51] confirms that the optimal E_J/E_C is similar as to what is obtained in the Bloch oscillations case, that is $E_J/E_C \sim 5$–10.

Besides being a prime example of synchronization, a ubiquitous phenomenon in non-linear physics[13], dual Shapiro steps have very concrete applications. The main one, like their usual counterpart, is metrological: shining a well-controlled frequency on the junction yields a very precise current through the relation (2.47); this current only depends on the frequency and the electric charge, a fundamental constant. This places dual Shapiro steps among effects considered for the metrological definition of the Ampere, in the same way that the usual Shapiro steps are used for the Volt standard [52]. Although predicted theoretically back in 1985 by Averin & Likharev [7], the first experimental evidence on the topic came at the start of the 90s [53, 54] with a clear demonstration of the blockade at zero bias, but only weak signatures of the steps in dI/dV under microwave irradiation, putting them far from metrological applications. It was not until recent years that three independent works managed to measure the dual Shapiro steps in Josephson junctions [55–57]. One of these is the subject of Chapter 3 of this thesis.

2.3.4 Dissipative quantum tunneling: $P(E)$ theory

In the previous sections we have dealt with a junction coupled to an external environment which we considered purely resistive. However, in reality the impedance of the environment $Z(\omega)$ might not be purely ohmic. The impact of the frequency dependence of the environmental impedance can be modeled perturbatively through the $P(E)$ theory [35, 36]. The perturbative expansion is done in the tunneling operator which for us is going to be either $E_J \cos\hat{\varphi}$, for Cooper pair tunneling, or $W_0 \cos(\pi\hat{q}/e)$ for fluxon tunneling. We will present the formalism with a $\cos\varphi$ potential, but the results will carry over for dual case as long as the higher bands are not excited.

We consider the circuit shown on Fig. 2.9. It consists of a Josephson junction under voltage bias connected to a bath represented by an impedance $Z(\omega)$. The bath

[13] Superconductivity is another example of mutual phase-locking, loosely speaking.

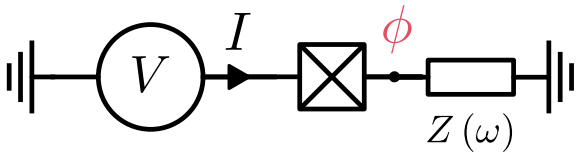

Figure 2.9: Circuit considered for the inelastic tunneling of Cooper pairs.

is going to be assumed in a thermal state of temperature T, and large enough so we can ignore the back action of the junction on its state. The junction is coupled to the impedance through the phase ϕ so that the phase difference φ across the junction is $\varphi = \phi - 2eVt/\hbar$ by virtue of the Josephson relation. The Hamiltonian of the system is thus

$$\hat{H} = \hat{H}_{bath} + \hat{H}_{coupling} = \sum_m \hbar\omega_m \hat{a}_m^\dagger \hat{a}_m - E_J \cos\left(\frac{2e}{\hbar}Vt - \hat{\phi}\right). \tag{2.62}$$

Here we included the capacitance of the junction C_J in the harmonic bath. This is done by diagonalizing the quadratic part of the Hamiltonian of Eq. (2.25). The variable ϕ is thus not anymore a degree of freedom independent of the bath, but is written as linear combination of the bath operators. Its fluctuations are given by [58]

$$\left\langle \hat{\phi}(t+\tau)\hat{\phi}(t)\right\rangle = 2\int_0^{+\infty} \frac{d\omega}{\omega} \frac{\mathrm{Re}\, Z_t(\omega)}{R_Q} \left[\coth\left(\frac{\hbar\omega}{2k_BT}\right)\cos\omega\tau - i\sin\omega\tau\right], \tag{2.63}$$

where Z_t is the total impedance of the circuit composed of Z in parallel with C_J, so that

$$Z_t(\omega) = \frac{1}{\frac{1}{Z(\omega)} - i\omega C_J}. \tag{2.64}$$

We now apply perturbation theory in the Josephson term $H_{coupling}$. The main observables of experimental relevance that we want to compute perturbatively are:

- The dc component of the tunneling current I_{dc}.
- The noise spectral density of the current $S_{II}(\omega)$.
- The impedance $Z_J(\omega)$ of the junction, to be defined later.

All of these are going to be expressed in terms of the P function defined by

$$P(E) = \frac{1}{2\pi\hbar}\int_{-\infty}^{+\infty} \left\langle e^{i\hat{\phi}(u)}e^{-i\hat{\phi}(0)}\right\rangle_0 e^{i\frac{E}{\hbar}u}\, du, \tag{2.65}$$

with the quantum averages $\langle\cdots\rangle_0$ done over the unperturbed bath in the thermal state. Since the bath's state is Gaussian-centered, we can express the correlation function appearing in Eq. (2.65) in terms of the phase correlator [35]

$$\left\langle e^{i\hat{\phi}(t)}e^{-i\hat{\phi}(0)}\right\rangle_0 = e^{J(t)}, \tag{2.66}$$

$$J(t) = \left\langle \left[\hat{\phi}(t) - \hat{\phi}(0)\right]\hat{\phi}(0)\right\rangle_0 = J^*(-t). \tag{2.67}$$

$P(E)$ represents the probability density of the environment absorbing an energy quantity E when a Cooper pair tunnels through the junction. Indeed, $P(E)$ is normalized:

$$\int_{-\infty}^{+\infty} P(E)\, dE = e^{J(0)} = 1. \tag{2.68}$$

Moreover, it obeys the detailed balance symmetry [35]:

$$P(-E) = e^{-E/k_B T} P(E). \tag{2.69}$$

Tunneling current.

The operator of the electric current flowing through the junction is given by

$$\hat{I} = -\frac{2e}{\hbar}\frac{\partial \hat{H}_{coupling}}{\partial \phi} = \frac{2e}{\hbar} E_J \sin\left(\frac{2e}{\hbar} V t - \hat{\phi}\right). \tag{2.70}$$

Applying the Kubo formula for the steady state value of $\langle \hat{I} \rangle$ gives:

$$\left\langle \hat{I}(t) \right\rangle = \left\langle \hat{I}(t) \right\rangle_0 - \frac{i}{\hbar}\int_{-\infty}^{t} \left\langle \left[\hat{I}(t), \hat{H}_{coupling}(t')\right] \right\rangle_0 dt'. \tag{2.71}$$

The operators on the right-hand side are in the interaction picture. In our case the first term is always going to vanish as we average over a thermal state which is Gaussian-centered. To compute the second term we split the sine/cosine into complex exponential terms, keep only the products which depend on the time difference $|t - t'|$ and ditch those who yields terms in $|t + t'|$ (who are going to oscillate at frequency $4eV/\hbar$). After some algebra we arrive at the expression for the dc current [35]:

$$I_{dc}(V) = \frac{\pi e E_J^2}{\hbar}\left[P(2eV) - P(-2eV)\right]. \tag{2.72}$$

Noise spectral density.

The noise emitted by the junction can be computed with the Fourier transform of the current correlator

$$S_{II}(\omega) = \int_{-\infty}^{+\infty} \left\langle \hat{I}(t+\tau)\hat{I}(t) \right\rangle e^{-i\omega\tau}\, d\tau. \tag{2.73}$$

To compute the current correlator we replace the two $\hat{I}$ with the expression from Eq. (2.70) and do the same treatment as for the dc current essentially. We expand the sines into exponentials, throw away the terms which are not stationary–those who oscillate with $4eV/\hbar$–and rearrange the correlators. We skip the calculations (for details see Ref. [37]) and just provide the final result

$$S_{II}(\omega) = \frac{2e^2 E_J^2}{\hbar^2}\int_{-\infty}^{+\infty} e^{J(\tau)} \cos\left(\frac{2e}{\hbar} V\tau\right) e^{-i\omega\tau}\, d\tau, \tag{2.74}$$

which can rewritten as

$$S_{II}(\omega) = \frac{2\pi e^2 E_J^2}{\hbar}\left[P(2eV - \hbar\omega) + P(-2eV - \hbar\omega)\right]. \tag{2.75}$$

Impedance of the junction.

To obtain the impedance Z_J of the junction perturbatively, we add a small monochromatic perturbation $\delta V(t)$ to the voltage so that the Josephson term of Hamiltonian (2.62) becomes, to first order in δV [21, 59]:

$$\hat{H}_{coupling}(t) = -E_J \cos\left(\frac{2e}{\hbar}Vt - \hat{\phi}\right) + \left[\int^t \delta V(t')\,dt'\right] \frac{2eE_J}{\hbar} \sin\left(\frac{2e}{\hbar}Vt - \hat{\phi}\right), \tag{2.76}$$

The current operator is expanded similarly:

$$\hat{I}(t) = \frac{2e}{\hbar}E_J \left\{\sin\left(\frac{2e}{\hbar}Vt - \hat{\phi}\right) + \left[\int^t \delta V(t')\,dt'\right] \frac{2e}{\hbar} \cos\left(\frac{2e}{\hbar}Vt - \hat{\phi}\right)\right\}. \tag{2.77}$$

We then compute the linear response of the junction current to find the admittance of the junction, $Y_J(\omega) = 1/Z_J(\omega)$,

$$Y_J(\omega) = \left(\frac{2eE_J}{\hbar}\right)^2 \frac{1}{2\hbar\omega} \int_0^{+\infty} \left[e^{J(\tau)} - e^{J^*(\tau)}\right] \left(e^{i\omega\tau} - 1\right) \cos\left(\frac{2e}{\hbar}V\tau\right) d\tau. \tag{2.78}$$

Using the definition of the current noise density (2.73), one can show that

$$\mathrm{Re}\, Y_J(\omega) = \frac{1}{2\hbar\omega}\left[S_{II}(-\omega) - S_{II}(\omega)\right], \tag{2.79}$$

which is essentially the generalized fluctuation-dissipation theorem applied to our system. We can also put Eq. (2.79) in the form

$$\mathrm{Re}\, Y_J(\omega) = \frac{e}{\hbar\omega}\left[I_{dc}(2eV + \hbar\omega) - I_{dc}(2eV - \hbar\omega)\right] \tag{2.80}$$

by using the definition from Eq. (2.72). This form is actually a particular case of the more general formula (see Refs. [60–62]) linking the finite frequency response of a junction under irradiation to replicas of its IV curve, akin to what we encountered for the dual Shapiro steps. The imaginary part of the admittance can also be found by using the Kramers-Kronig relations:

$$\mathrm{Im}\, Y_J(\omega) = -\frac{1}{\pi}\mathcal{P}\int_{-\infty}^{+\infty} \frac{\mathrm{Re}\, Y_J(\omega')}{\omega' - \omega}\, d\omega', \tag{2.81}$$

where $\mathcal{P}$ represents the Cauchy principal value. The right-side is also called the Hilbert transform of $\mathrm{Re}\, Y_J$.

Asymptotic behaviour and applicability of the $P(E)$ theory.

We now showcase some asymptotes of the $P(E)$ theory and then discuss its range of applicability. For the following discussions we are going to assume that $Z(\omega) = R$ such that the total impedance $Z_t(\omega)$ is the impedance of an RC circuit:

$$Z_t(\omega) = \frac{R}{1 + (\omega/\omega_{RC})^2}, \quad \omega_{RC} = \frac{1}{RC_J}. \tag{2.82}$$

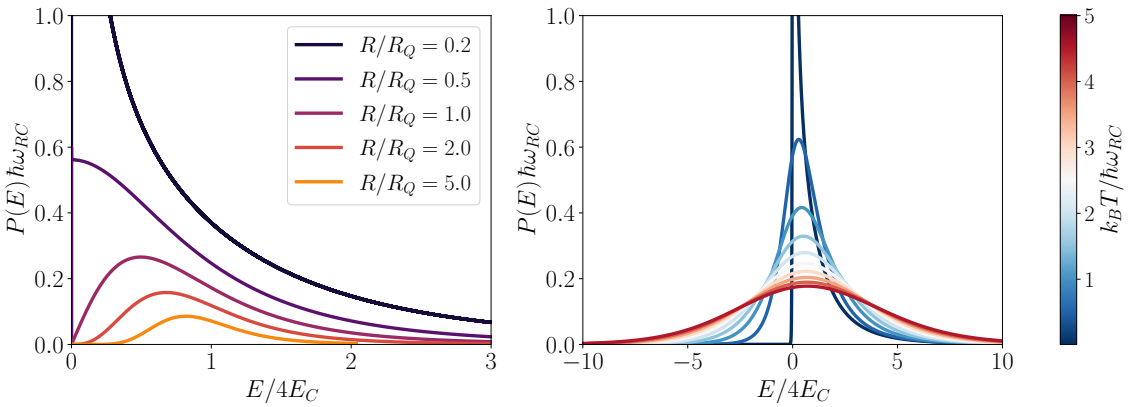

Figure 2.10: Left: evolution of the $P(E)$ distribution as a function of the impedance at $T = 0$. Right: evolution of the $P(E)$ distribution as a function of the temperature for $R/R_Q = 0.2$.

First, in the zero-temperature limit we have $P(E < 0) = 0$ because of Eq. (2.69), and at low voltage $P(E)$ scales as [35, 36]

$$P(E) \overset{E\to 0^+}{\propto} \left(\frac{E}{\hbar\omega_{RC}}\right)^{2\alpha-1}, \quad \alpha = \frac{R}{R_Q}, \quad R_Q = \frac{h}{4e^2}. \tag{2.83}$$

We plot on Fig. 2.10 the $P(E)$ function at $T = 0$ for various values of α. We see that at low bias $V \to 0$ the low frequency admittance of the junction diverges $Y_J(\omega) \propto dP/dE$ if $R < R_Q$. This divergence signals that our perturbative treatment fails and is, to some extent, a signature of the Schmid transition [21]. Now in the opposite limit, when the temperature becomes high compared to the cutoff ω_{RC}, the function $P(E)$ becomes approximately Gaussian. This can be seen by computing the integral of Eq. (2.63) in the limit of high T yielding

$$J(t) = \pi\alpha\left[\frac{2k_BT}{\hbar\omega_{RC}}A(t) + iB(t)\right], \tag{2.84}$$

$$A(t) = 1 - \omega_{RC}|t| - e^{-\omega_{RC}|t|}, \tag{2.85}$$

$$B(t) = \mathrm{sign}(t)\left(e^{-\omega_{RC}|t|} - 1\right). \tag{2.86}$$

Then, if $k_BT \gg \hbar\omega_{RC}/\alpha$, the integral of $e^{J(t)+iEt}$ will be dominated by small t such that we can use the short-time expansion of Eq. (2.84) yielding a Gaussian:

$$P(E) = \frac{(\alpha k_BT\hbar\omega_{RC})^{-1/2}}{2\pi}\exp\left[-\frac{(E-\alpha\hbar\omega_{RC})^2}{4\pi\alpha k_BT\hbar\omega_{RC}}\right]. \tag{2.87}$$

The result of a numerical computation of $P(E)$ for increasing temperature, and at fixed α is plotted on the second panel of Fig. 2.10.

Finally, in the high-energy limit $E \gg \hbar\omega_{RC}$, $P(E)$ dies out, either polynomially for zero temperature $P(E) \sim E^{-3}$ [35] or exponentially at high temperature. Therefore, $Y_J(\omega) \to 0$, the tunneling is suppressed by the RC cutoff, and the junction behaves as a pure capacitance C_J.

To conclude this part we discuss a bit on the range of validity of the $P(E)$ framework. The first remark is that since it is a perturbative expansion, the expansion

parameter should satisfy a smallness condition. This is given by $E_J P(E) \ll 1$ for the Josephson potential. This is equivalent to saying that the current calculated with Eq. (2.72) should be small compared to the critical current of the junction. As such, $P(E)$ is applicable to small junctions (obviously) but also to bigger junctions coupled to a hot environment. This condition also tells us that for the low impedance case, the theory cannot be trusted at low bias because of the divergence of Eq. (2.83). Evidently, the theory misses all the Bloch dynamics we described in the previous sections as this dynamics is non-perturbative in E_J.

Another, perhaps more subtle point, is that $P(E)$ fundamentally describes incoherent processes. Indeed, by using linear response theory and enforcing the stationarity of our correlation functions, we implicitly assume that the tunneling events are independent and well separated in time. This is also evident in Ref. [35], where the authors derive the theory through Fermi Golden rule. This means that the bath memory should decay faster than the tunneling characteristic time $\tau_{P(E)} \sim 2e/I_{dc}$, i.e. that $P(E)$ should vary on scales much bigger than $1/\tau_{P(E)}$[14]. The fourth chapter of this thesis tackles the problem of extending $P(E)$ in environments where this condition fails.

2.3.5 The Schmid phase transition

During the previous sections we mentioned several times the Schmid transition when faced with sharp behavior changes at $R = R_Q$. We discuss it in a bit more detail here. The goal is not really to study this phase transition, but more to add weight to the $R > R_Q$ condition we mentioned multiple times. The interested reader can consult the seminal review by Schön & Zaikin [13], or the more modern Refs. [21, 63, 64] (and references therein), for a more complete and quantitative overview of the topic.

The transition, first described by Schmid [65], concerns the localization of quantum particle, moving in a periodic potential, due to dissipation, implemented through the ohmic coupling to an external infinite bath. At low dissipation the particle explores all the potential wells and its ground state is similar to the Bloch eigenvector. Upon increasing the dissipation past a threshold value the system undergoes a quantum phase transition where the particle is localized around the bottom of a well of the potential. We illustrate this on figure 2.11. There is now an infinite amount of degenerate ground states which correspond to choosing another well for the localization (they are all equivalent). As usual for quantum phase transitions, the degeneracy is lifted when one "pokes" the system by introducing a symmetry breaking term [66]. In this regard Schmid computed the mobility of the particle, i.e. the linear response of the velocity to a small tilt of the potential, and found that a localized particle stays trapped in the potential wells due to dissipation, leading to a vanishing mobility. In the other phase, the dissipation is not enough to hinder tunneling and the particle can run down the potential, yielding a large (infinite) mobility. Perhaps the most impressive thing about this transition is that it seems to not depend on the strength of the potential nor on the mass of the particle and everything is determined by the coupling strength to the bath. Proving this for

[14] This was not so much of a problem for us since we considered a flat Z_t but had we considered a single mode resonator coupled to the junction we would have had to make sure its linewidth κ is larger than $1/\tau_{P(E)}$, for example [37].

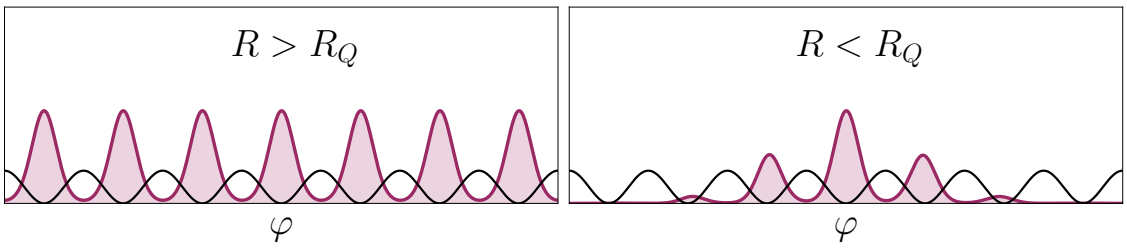

Figure 2.11: Pictorial representation of the probability density (purple) for the junction phase difference, when it is insulating (left) and superconducting (right). On the insulating side the phase is delocalized and the groundstate of the system is close to a Bloch eigenvector. In the superconducting side there is an infinite amount of degenerate groundstates localized around different minimas of the periodic potential (black).

the complete phase diagram is still the topic of ongoing research at the time of writing [64, 67].

This model belongs to a more general class of quantum impurity models which have received a lot of attention in the many-body physics community. Indeed, a particle in a periodic potential can be seen as a generalization of the spin-boson model, which describes the localization of a particle in a double well potential, and the spin-boson model itself is equivalent at low energy to the famous Kondo problem [6].

The relation to a Josephson junction shunted by a resistor is quite direct: the potential is the Josephson term $-E_J \cos\hat{\varphi}$, the mass of the particle C_J, the ohmic bath is the resistor R and the transition happens at $R_Q = h/4e^2 \sim 6.45\,\mathrm{k}\Omega$. The velocity of the particle corresponds to the voltage drop across the junction and the tilt is induced by an external current source, so that the mobility is the dc impedance of the junction. For $R > R_Q$ the system is mildly perturbed by the bath and still exhibit all the non-linear quasi-charge related behaviors we described in the previous sections. The impedance of the junction is close to Eq. (2.18) and diverges at zero frequency because of the blockade described by Eq. (2.34). At $R < R_Q$ the particle is trapped in one of the wells, so no voltage develops across it: its low-frequency impedance is purely inductive and a supercurrent given by $I_C \sin\varphi$ can flow. Since the well index operator is conjugate to the quasi-charge, on this side of transition q ceases to be a good quantum number[15]. Because of these two limits it is also common to refer to the localized case as "superconducting" and the delocalized as "insulating" (although the electrodes are still perfectly superconducting).

Ironically, it is the superconducting state, where the junction is strongly entangled with the bath, which is most easily observed when doing transport measurements. This is a consequence of the natural low impedance of experimental measurement apparatuses at GHz frequencies. Moreover, the insulating response of large junction is exponentially suppressed according to Eq. (2.11) and so any large noise or temperature will wash out the blockade in dc.

Although direct measurements of the insulating state exist [56, 57, 68, 69], a

[15]That does not mean q necessarily becomes meaningless. If the localization length spans many wells it might still make sense to write down the reduced density matrix of the junction in the Bloch band basis.

clear study of the transport properties across the transition is still lacking to this day. Beyond transport measurements, the finite-frequency response of the junction should also display signatures of its insulating/superconducting state [21]. As such, great efforts went into characterizing the response of a junction embedded in a high-impedance environment [70–72] culminating in a recent work [73] claiming the finite-frequency observation of the transition in-situ.

2.3.6 Summary of the IV curves of a junction coupled to an ohmic environment

In this section we recapitulate different possible IV curves that can be obtained when coupling a junction to an external resistor R. For the sake of simplicity we put ourselves at zero temperature, ignore quasiparticles unless the voltage exceed $2\Delta/e$, and consider a purely dc bias.

The IVs for the low impedance case $R \ll R_Q$ are given on figure 2.12 for three sizes of junction: large, medium and small. In all three cases we suppose the junction overdamped so that $RC_J\omega_p \ll 1$. Due to the low R the junction is phase-localized, at low currents the particle sits in one of the well of the tilted washboard phase potential and the junction does not develop any voltage. However, when the tilt (the current I) increases, the particle can escape its well and start running down the potential, yielding a finite voltage. This effect is stronger in smaller junctions: their capacitance being smaller, the phase particle is lighter, and so its escape is facilitated. As a result, the maximum current achievable is significantly lower than I_C for small junctions. In this overdamped regime one can use the expansions of Ref. [74] to compute the IV characteristics. In the opposite underdamped regime the junction will directly switch to its resistive state once the particle escape the potential [33], in which case one can compute the impact of fluctuations on the switching rate, see e.g. Refs. [31, 75].

For high-impedance, $R > R_Q$, we provide a more detailed analysis of the phenomenology in figure 2.13, where we present the IV characteristics along with the corresponding dynamics within the Bloch bands at various points.

For $E_J/E_C \gg 1$ (i), the curve is close to the underdamped classical case since tunneling between wells is exponentially suppressed. Nonetheless, there exists a blockade at low currents (a) where the system stabilizes in the lowest band due to friction. Once the voltage across the junction exceeds V_C, the particle moves in the band at a fixed velocity I, yielding an oscillating voltage of frequency $\omega_B = I/2e$: the Bloch oscillations (b). The system stays in this state until the frequency ω_B becomes resonant with a transition to the higher bands (c). As shown on figure 2.6 and discussed before, this also corresponds to aligning the different energy levels of two neighboring wells in the phase representation. Depending on the dissipation, this process should yield a sharp bump in the IV, or even a finite transition rate to the resistive state [43, 44] if the junction is underdamped. Eventually, the frequency (or the tilt) is such that the particle can overcome the Josephson potential E_J and ionize to a free particle state (d), which is equivalent to running down the potential in phase. Again, the junction being underdamped most likely, it will switch to its resistive state with quasi certainty. The switching current can be computed with the usual formulas for macroscopic quantum tunneling (MQT) [31, 75].

When E_J/E_C is reduced (ii), tunneling between cosine wells becomes significant,

leading to appreciable Bloch band widths and causing the IV characteristics to deviate considerably from the classical case. Similar to the large-junction scenario, a blockade occurs at low bias (a), followed by a transition into Bloch oscillations (b), resulting in a back-bending feature in the IV curve. However, unlike the resonant transitions observed in the large-junction case, transitions to higher bands (c) are better described as Landau-Zener transitions. In this regime, dissipation plays a crucial role in stabilizing the steady state by facilitating relaxation back to the lower bands before another transition occurs [42]. This mechanism introduces a positive slope in the IV characteristic and disrupts the coherence of Bloch oscillations. Beyond point (c), the system's behavior depends on the specific properties of the junction. In principle, neglecting the superconducting gap, the current should decrease due to the same mechanism that suppresses current in curve (iii) [76], which will be discussed in the following paragraph. However, during excursions into higher bands, the instantaneous voltage may exceed $2\Delta/e$ at certain points, leading to quasiparticle generation, increasing dissipation and allowing the junction to sustain a higher current [40, 41].

Finally, at very low E_J/E_C (iii), we recover the curve given by the $P(E)$ theory [76], which has a non-zero current only around $V = V_C$ for a high-impedance environment. In this limit, the dynamics of the charge becomes driven by the fluctuations of the environment and so, incoherent. The Brillouin zone picture is thus inadequate since the system will end up in a statistical mixture of many charge states. Nonetheless, we can abuse notation a bit and consider the dynamics of the system in an extended quasi-charge picture with some weakly coupled charge parabolas $E(q, N) = (q - 2eN)^2/2C_J$, indexed by an integer N. In the blockade state (a) the charge particle sits in one parabola and no current flows. However, when the voltage tunes the charge so that it approaches the crossing points (b1, c1) the fluctuations of the bath can shift N by 1 through the Josephson term. Due to this tunneling, the voltage across the junction drops in the negative, the capacitance recharges in a characteristic time RC_J and the system eventually comes back to its initial state, waiting for another tunneling event (b2, c2). This cycle repeats at random, yielding a finite dc current in the IV curve. It can be computed with the $P(E)$

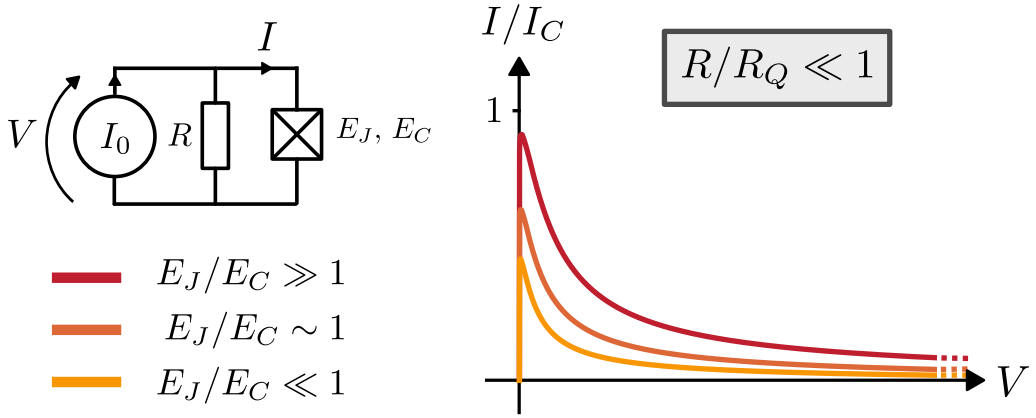

Figure 2.12: Summary of the IV curves of a junction coupled to resistor with $R \ll R_Q$ at zero temperature. A circuit indicating I and V is also given on the left. We assume that R is small enough so that the junction is considered overdamped no matter E_J/E_C.

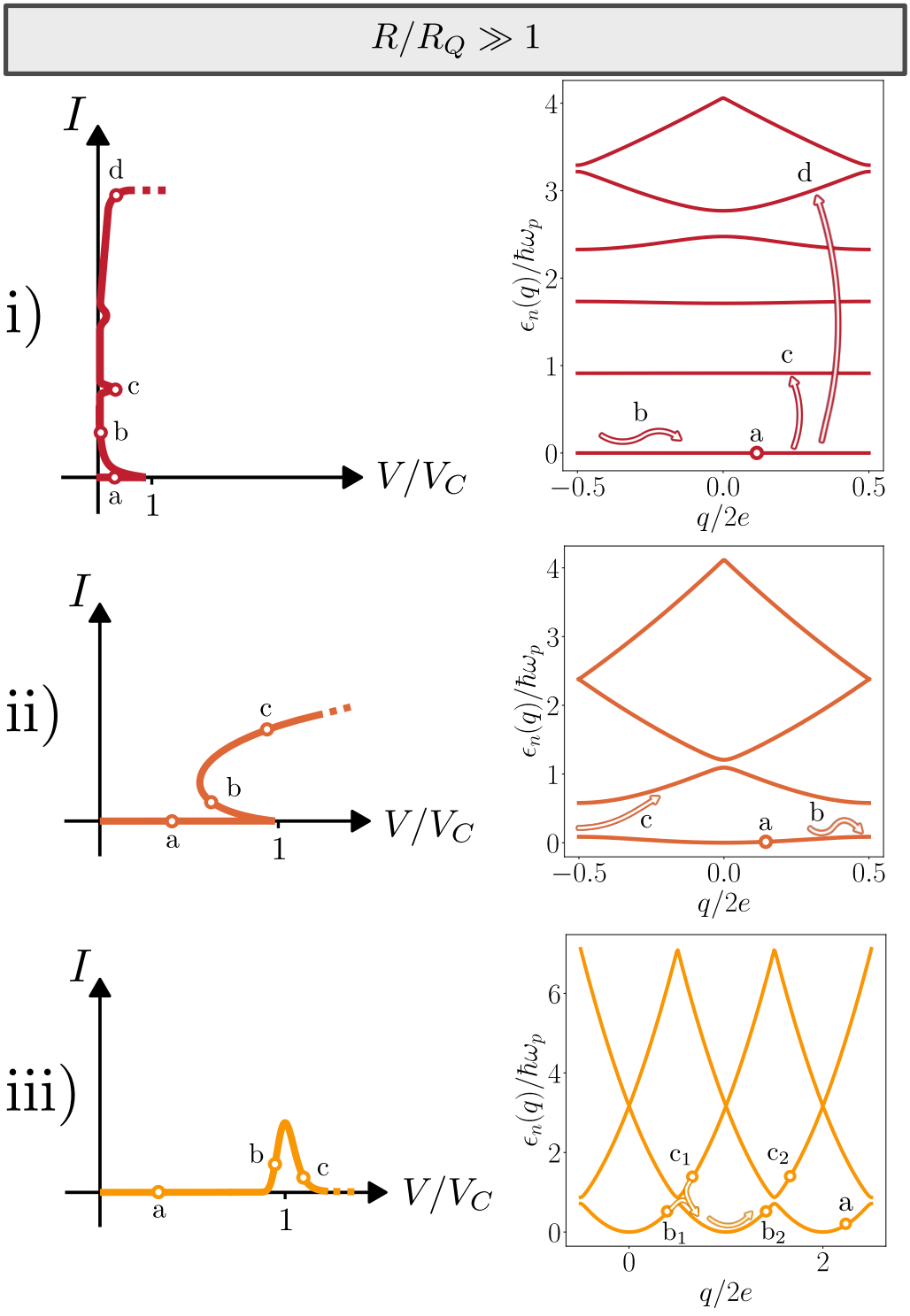

Figure 2.13: Summary of the IV curves of a junction coupled to a resistor with $R \gg R_Q$ at zero temperature, and for varying E_J/E_C. The definitions of I and V, and the color code are the same as in Fig. 2.12. When E_J/E_C is large (i) the effects of quantum fluctuations are minimal and the curve is close to the phase-classical one. However, at moderate (ii) or small (iii) E_J/E_C ratios, quantum effects can strongly affect the response of the junction. The various points of interest of the IVs (a, b, c, d) are detailed in the main text.

formalism where the recharging part of the dynamics is taken care of by absorbing the capacitor in the external impedance. Far from $V \approx V_C$ the coupling between neighboring parabolas is strongly suppressed and the current dies out. Since the dynamics is completely incoherent, there are no Bloch oscillations in this case.

Obviously, the cases described here are, to some extent, idealized. First, finite temperature will wash out some features of the curves. In case (i) it will most likely hide the band dynamics (a,b,c) because the band widths are exponentially small. For (ii) and (iii), the blockade state should be observable at temperatures on the order of dozens of milli-Kelvins since $V_C \sim 30\,\mu\text{V}$ for $C_J \sim 10\,\text{fF}$. It is also worth mentionning that the presence of quasi-particles can give rise to a bump in the IV curve at low currents through single electron tunneling [40, 77]. Finally, the quantum fluctuations of the resistor will lead to some tunneling out of the blockade state (a). This will give some finite conductance at low bias which can be computed with the formulas of Ref. [74], or using the dual version of $P(E)$ in the large junction case [35].

2.3.7 The need for high impedance environments

The previous sections highlighted the importance of a high-impedance environment for the observation and usage of the non-linear capacitive response of a junction. This environment also needs to be sufficiently broadband in order to cover the frequency band related to the junction dynamics, typically from dc up to $\omega_p \sim 10\,\text{GHz}$.

Implementing this experimentally can be challenging since the impedance needs to be close to the junction in order to not be shunted by stray capacitances at these frequencies. The rule of thumb being that the junction feels the impedance of the environment on the scale of a wavelength of the radiation. Thus, for tens of GHz this means roughly $d \sim 1\,\text{cm}$, i.e. the size of a microchip on which we fabricate our superconducting circuits and so the impedance should be on-chip, ideally.

Multiple candidate solutions have emerged for the realization of these high impedances. Obviously, putting thin-film resistor on-chip close to the junction is the most straightforward one. This was, historically, the first way of embedding a junction inside a high impedance environment [54, 78]. The main drawback of this method is the heating of the resistors, which in turn affect the response of the junction, proper care has then to be taken to control the electronic temperature during measurement.

A second solution is to replace the resistor by a superconducting transmission line of high impedance $\sqrt{L/C_g}$ by using materials with large inductances L per length and by pushing away the ground to reduce the capacitance C_g. The idea behind being to avoid Joule heating while also permitting the measurement of energy dissipated by the junction. Materials used for this purpose can be disordered superconductors with high kinetic inductances, such as granular aluminum [56, 79, 80], titanium nitride [57], or niobium nitride [81]. The transmission line can also be made with Josephson junctions deep in the harmonic regime thus creating a high impedance metamaterial [82–84]. This is the solution we are going to use in this thesis but we will show in Chapter 4 that, despite being superconducting, a finite-size transmission line will experience the photonic form of Joule heating.

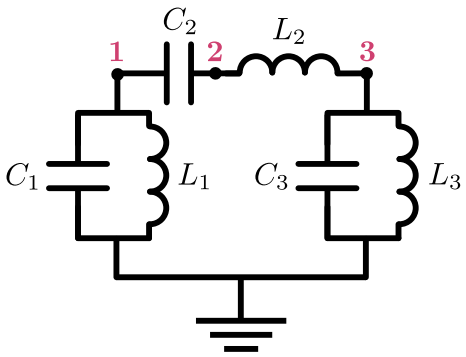

Figure 2.14: A simple linear circuit described by 3 node fluxes, whose positions are highlighted in purple.

2.4 Linear circuit theory

Until now, we have taken the dissipative bath of our circuits as granted, but in practice, as stated in the previous paragraph, we are going to implement the bath with a long transmission line. Thus, we now recapitulate various tools used to model large linear circuits in order to explain how to find their normal modes and the impedance felt by a system coupled to them. We start with the general case of an arbitrary circuit, and then focus on the description of transmission lines.

2.4.1 Conservative circuits

Normal mode decomposition

Starting with the dissipationless case, we consider an arbitrary circuit composed of capacitances and inductances. We take as our degrees of freedom the node fluxes $\{\Phi_n\}$ of the circuit, linked to the usual node voltages $\{V_n\}$ by analogy with Faraday's law $\dot{\Phi}_n = V_n$, so that its Lagrangian can be written down as:

$$\begin{aligned}\mathcal{L} &= \sum_{m,n} \frac{1}{2} C_{mn} \left(\dot{\Phi}_m - \dot{\Phi}_n\right)^2 - \frac{1}{2L_{mn}} \left(\Phi_m - \Phi_n\right)^2 \\ &= \frac{1}{2} \dot{\vec{\Phi}}^T \mathbf{C} \dot{\vec{\Phi}} - \frac{1}{2} \vec{\Phi}^T \mathbf{\Gamma} \vec{\Phi},\end{aligned} \tag{2.88}$$

where we bundled all the degrees of freedom in the vector $\vec{\Phi}$. We also defined the capacitance matrix $\mathbf{C}$ and the inverse inductance matrix $\mathbf{\Gamma}$ that we choose to be symmetric. For example, the matrices corresponding to the circuit represented Fig. 2.14 are

$$\mathbf{C} = \begin{bmatrix} C_1 + C_2 & -C_2 & 0 \\ -C_2 & C_2 & 0 \\ 0 & 0 & C_3 \end{bmatrix}, \quad \mathbf{\Gamma} = \begin{bmatrix} \frac{1}{L_1} & 0 & 0 \\ 0 & \frac{1}{L_2} & -\frac{1}{L_2} \\ 0 & -\frac{1}{L_2} & \frac{1}{L_2} + \frac{1}{L_3} \end{bmatrix}. \tag{2.89}$$

The canonical momenta $(Q_1, Q_2, \dots) = \vec{Q}$, which correspond to the electrical charges on each of the circuit nodes, and the Hamiltonian $\mathcal{H}$ of the system are then

$$\vec{Q} = \frac{\partial \mathcal{L}}{\partial \dot{\vec{\Phi}}} = \mathbf{C} \dot{\vec{\Phi}}, \tag{2.90}$$

$$\mathcal{H} = \frac{1}{2} \vec{Q}^T \mathbf{C}^{-1} \vec{Q} + \frac{1}{2} \vec{\Phi}^T \mathbf{\Gamma} \vec{\Phi}. \tag{2.91}$$

The dynamics can be fully solved by finding the *normal modes* of the system. To do so, one solves the following generalized eigenvalue problem

$$\mathbf{P}^T\mathbf{C}\mathbf{P} = \mathbb{1}, \quad \mathbf{P}^T\mathbf{\Gamma}\mathbf{P} = \mathbf{\Omega}^2, \tag{2.92}$$

yielding two matrices: $\mathbf{P}$ the matrix of eigenvectors containing information on the mode envelopes, and a diagonal matrix $\mathbf{\Omega}$ whose entries $\{\omega_m\}$ are the resonant frequencies of each mode. Then performing the change of coordinates $\vec{x} = \mathbf{P}^{-1}\vec{\Phi}$ and $\vec{p} = \mathbf{P}^T\vec{Q}$ brings the Hamiltonian from Eq. (2.91) in its diagonal form (one can check that this transformation is symplectic and thus leaves the Poisson bracket unchanged)

$$\mathcal{H} = \sum_m \frac{1}{2}p_m^2 + \frac{1}{2}\omega_m^2 x_m^2. \tag{2.93}$$

Anticipating quantum mechanics, we can define the complex coordinates $\alpha_m = \frac{1}{\sqrt{2\hbar\omega_m}}(\omega_m x_m + ip_m)$ so that the Hamiltonian becomes

$$\mathcal{H} = \sum_m \hbar\omega_m \alpha_m^* \alpha_m, \tag{2.94}$$

with α_m^* denoting the complex conjugate of α_m (the introduction of $\hbar$ here is arbitrary and is done just for convenience). The equations of motion then become trivial,

$$\dot{\alpha}_m = -\frac{i}{\hbar}\frac{\partial \mathcal{H}}{\partial \alpha_m^*} = -i\omega_m\alpha_m \implies \alpha_m(t) = \alpha_m(0)e^{-i\omega_m t}, \tag{2.95}$$

allowing us to compute the time evolution of any observable of the system by decomposing it in the normal basis.

Linear response

Apart from the resonant modes of the circuit, we want to access the linear response of the circuit at a given frequency ω, since it determines the impedance seen by a small system coupled to it; moreover, it directly relates to quantities measured experimentally (for example, the transmission coefficient S_{21}). The linear response can be encoded in the impedance matrix $\mathbf{Z}(\omega)$ whose elements $Z_{mn}(\omega)$ connect the Fourier transform of the voltage $V_m(\omega) = -i\omega\Phi_m(\omega)$ appearing at node m due to a small current source $I_n(\omega)$ into node n, so that $Z_{mn} = V_m/I_n$. Plugging a current source into node n adds a $-I_n(t)\Phi_n$ term to the Lagrangian (2.88) so that the equation of motion for $\vec{\Phi}$ becomes

$$\mathbf{C}\ddot{\vec{\Phi}} + \mathbf{\Gamma}\vec{\Phi} = \vec{I}, \tag{2.96}$$

with $\vec{I} = [0, \cdots, I_n(t), \cdots, 0]^T$. Fourier transforming Eq. (2.96) and inverting the matrix of the left-hand side, we directly find

$$\mathbf{Z}(\omega) = -i\omega\left(\mathbf{\Gamma} - \omega^2\mathbf{C}\right)^{-1} \tag{2.97}$$

$$= -i\omega\mathbf{P}\left(\mathbf{\Omega}^2 - \omega^2\right)^{-1}\mathbf{P}^T. \tag{2.98}$$

2.4.2 Dissipative circuits

Adding linear dissipation to our circuits is straightforward classically, the equations of motion can still be derived from the circuit Lagrangian from Eq. (2.88) but we have to add the dissipation to the Euler-Lagrange equations by means of Rayleigh's dissipation function $\mathcal{R}$:

$$\begin{aligned} \frac{d}{dt}\frac{\delta \mathcal{L}}{\delta \dot{\Phi}} - \frac{\delta \mathcal{L}}{\delta \Phi} = -\frac{\delta \mathcal{R}}{\delta \dot{\Phi}}, \quad \mathcal{R} = \frac{1}{2}\dot{\vec{\Phi}}^T \mathbf{G} \dot{\vec{\Phi}} \\ \iff \mathbf{C}\ddot{\vec{\Phi}} + \mathbf{G}\dot{\vec{\Phi}} + \mathbf{\Gamma}\vec{\Phi} = 0, \end{aligned} \tag{2.99}$$

where $\mathbf{G}$ is the conductance matrix whose entries G_{mn} are constructed in the same fashion as for $\mathbf{C}$ and $\mathbf{\Gamma}$, but for the inverse of the resistances connecting two nodes of the circuits. Finding the now damped normal modes of the circuit can again be done by solving a generalized eigenvalue problem where the matrices involved are now twice as big as in the undamped case because we recast the system (2.99) as

$$\frac{d}{dt}\begin{bmatrix} 0 & \mathbf{C} \\ \mathbf{C} & \mathbf{G} \end{bmatrix}\begin{bmatrix} \dot{\vec{\Phi}} \\ \vec{\Phi} \end{bmatrix} = \begin{bmatrix} \mathbf{C} & 0 \\ 0 & -\mathbf{\Gamma} \end{bmatrix}\begin{bmatrix} \dot{\vec{\Phi}} \\ \vec{\Phi} \end{bmatrix}. \tag{2.100}$$

Then, we solve the following eigenvalue problem

$$\mathbf{P}^T \begin{bmatrix} 0 & \mathbf{C} \\ \mathbf{C} & \mathbf{G} \end{bmatrix} \mathbf{P} = \mathbb{1}, \quad \mathbf{P}^T \begin{bmatrix} \mathbf{C} & 0 \\ 0 & -\mathbf{\Gamma} \end{bmatrix} \mathbf{P} = \mathbf{\Lambda} \tag{2.101}$$

where $\mathbf{\Lambda}$ contains the eigenvalues $\{\lambda_m\}$ of the system which are now complex-valued since the two matrices are not positive definite. The real parts correspond to half of the mode's energy loss rate (amplitude damping rate) $\mathrm{Re}\,\lambda_m = \frac{1}{2}\kappa_m$ and the imaginary parts are the resonant frequencies $\mathrm{Im}\,\lambda_m = \omega_m$. The normal mode variables $\vec{\alpha} = \{\alpha_m\}$ and their equations of motion are then simply obtained by

$$\vec{\alpha} = P^{-1}\begin{bmatrix} \dot{\vec{\Phi}} \\ \vec{\Phi} \end{bmatrix} \implies \dot{\alpha}_m = \left(-i\omega_m - \frac{1}{2}\kappa_m\right)\alpha_m. \tag{2.102}$$

We also note that, since the matrices in Eq. (2.100) are real, for every α_m the complex conjugate α_m^* is also a normal mode with $\dot{\alpha}_m^* = \lambda_m^* \alpha_m^*$.

The impedance matrix of the system simply becomes

$$\mathbf{Z}(\omega) = -i\omega\left(\mathbf{\Gamma} - i\omega\mathbf{G} - \omega^2\mathbf{C}\right)^{-1}. \tag{2.103}$$

2.4.3 Quantum circuits

Quantizing linear circuits is done by replacing the Poisson bracket with the commutator, so that for circuit variables we have [58]

$$\left[\hat{\Phi}_m, \hat{Q}_n\right] = i\hbar\delta_{mn}, \tag{2.104}$$

and for the normal mode variables[16]:

$$\left[\hat{a}_m, \hat{a}_n^\dagger\right] = \delta_{mn}. \tag{2.105}$$

[16] We use the usual annihilation and creation operators, $\hat{a}$ and $\hat{a}^\dagger$ for the operator versions of α and α^*.

The equations of motion for the quantum averages are the same as the classical equations of motion since everything is linear. However, in the case of dissipative circuits one needs to employ the formalism of open quantum systems to properly derive the equation of motion for the system operators (see e.g. Ref [5]) which contains quantum noise terms coming from the fluctuations in the resistors. Overall the dynamics does not really display any interesting or novel phenomena in the quantum regime until we introduce non-linearity in the circuits. Our way of doing this will be through the usage of superconducting tunnel junction that we describe shortly after.

2.4.4 Transmission lines

In the previous sections we described how we can extract the normal modes of an arbitrary linear circuit. However, in circuit-QED we often deal with circuits possessing a 1D geometry that we can treat as transmission lines. In the most general of cases, a transmission line is a circuit composed of a unit cell containing an in-line impedance $Z_l(\omega)$ and a ground impedance $Z_g(\omega)$ as shown on Fig. 2.15. These impedances can be made of more complicated linear circuits as long as the system is made of a repetition of these circuits. Formally, this means that the differents matrices from the previous sections will be tridiagonal by block (the block size will depend on the number of internal nodes composing Z_l and Z_g). Since we are using impedances, the dynamical equations of the system are better written in terms of the nodes' voltages $\{V_n(\omega)\}$ and the inline currents $\{I_n(\omega)\}$:

$$\begin{cases} V_{n+1}(\omega) - V_n(\omega) = -Z_l(\omega) I_n(\omega) \\ I_n(\omega) - I_{n-1}(\omega) = -\frac{1}{Z_g(\omega)} V_n(\omega) \end{cases} . \tag{2.106}$$

For now, we consider an infinite transmission line, so that we aim at solving the dynamics by using travelling waves. Moreover, we make the continuum approximation of Eqs. (2.106). This can be done by defining a unit cell size a so that $V_n(\omega) = V(x/a, \omega)$ and taking the limit $a \to 0$ while keeping Z_l/a and Z_g/a constant. This assumption is valid if we are only interested in waves whose wavelengths are large compared to the unit cell. We thus end up with [85]

$$\begin{cases} \partial_x V(x,\omega) = -Z_l(\omega) I(x,\omega) \\ \partial_x I(x,\omega) = -\frac{1}{Z_g(\omega)} V(x,\omega) \end{cases} \implies \begin{cases} \partial_x^2 V = \gamma^2 V \\ \partial_x^2 I = \gamma^2 I \end{cases} , \tag{2.107}$$

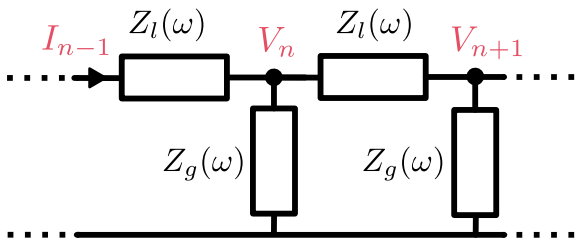

Figure 2.15: The equivalent circuit of an infinite transmission line with in-line impedance $Z_l(\omega)$ and a ground impedance $Z_g(\omega)$. The voltage and current variables are also represented.

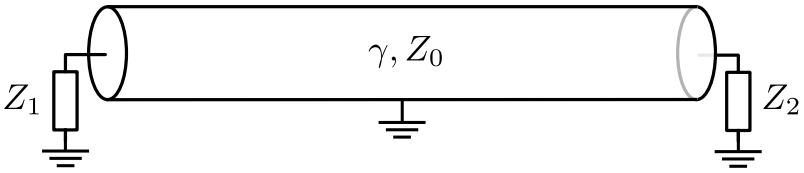

Figure 2.16: A finite-length transmission line, characterized by its propagation constant γ and its impedance Z_0, terminated by the impedance Z_1 on the left side and Z_2 on the right one.

where we defined the propagation constant $\gamma = \sqrt{Z_l/Z_g}$. Voltage and current waves of a particular frequency are then a superposition of right-going and left-going waves,

$$\begin{cases} V(x,\omega) = V^+ e^{-\gamma x} + V^- e^{\gamma x}, \\ I(x,\omega) = I^+ e^{-\gamma x} + I^- e^{\gamma x}. \end{cases} . \tag{2.108}$$

Additionally, Eqs. (2.107) also give us the relation

$$\frac{V^+}{I^+} = -\frac{V^-}{I^-} = \sqrt{Z_l Z_g} = Z_0. \tag{2.109}$$

We call Z_0 the *characteristic impedance* of our transmission line.

Finite-size transmission lines

In reality, most transmission lines in our circuits will be of finite length. To model this, we consider a piece of transmission line of length L, terminated by impedances, Z_1 on the left ($x = 0$) and Z_2 on the right ($x = L$), see Figure 2.16. These impedances will reflect back any incoming wave, creating a Fabry-Pérot 1D cavity. The modes of this cavity could be found by discretizing the transmission line, essentially reverting to Eqs. (2.106) but with boundary conditions, and applying the general matrix formalism described in the previous section. However, the 1D geometry of the system allows for simpler and more intuitive formulas. The boundary conditions impose

$$\begin{cases} V(0,\omega) = -Z_1(\omega) I(0,\omega), \\ V(L,\omega) = Z_2(\omega) I(L,\omega), \end{cases} \tag{2.110}$$

so that the two amplitudes from Eq. (2.108) are related by

$$\begin{cases} V^+ = r_1 V^-, \\ V^- e^{\gamma L} = r_2 V^+ e^{-\gamma L}, \end{cases} \tag{2.111}$$

where $r_{1/2}$ are the complex reflection coefficients from the left and right ends of the line given by

$$r_{1/2} = \frac{Z_{1/2} - Z_0}{Z_{1/2} + Z_0}. \tag{2.112}$$

Therefore, the resonant condition can be written as

$$r_1 r_2 e^{-2\gamma L} = 1, \tag{2.113}$$

which the discrete complex frequencies λ_m of the system are solutions of. This equation just means that, on resonance, a wave of a given wavevector has to come back to itself after propagating for a full round trip along the line.

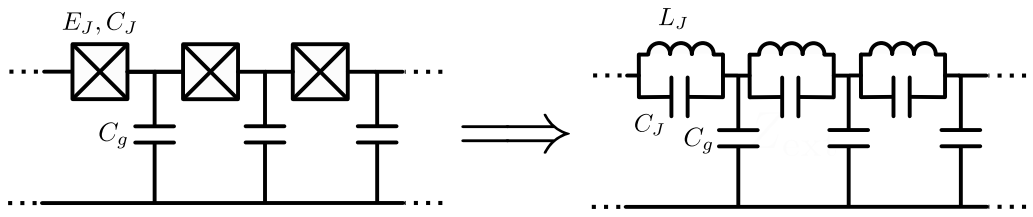

Figure 2.17: The circuit representation for a Josephson junction chain (left) and its linear approximation (right).

Implementing a bath with a transmission line

Since ultimately our goal is to create a dissipative bath with this transmission line, we consider the impedance seen by a system (a small junction) at one end. For instance, Z_1 in Figure 2.16 experiences an impedance $Z_{\rm tl}$ given by [85]:

$$Z_{\rm tl}(\omega) = \frac{V(0)}{I(0)} = Z_0 \frac{1 + r_2 e^{-2\gamma L}}{1 - r_2 e^{-2\gamma L}}. \tag{2.114}$$

This means that, unless there is a perfectly absorbing boundary on the other end ($r_2 \approx 0$) or large bulk losses [$\mathrm{Re}(2\gamma L) \gg 1$], our system does not see the smooth impedance $Z_0(\omega)$, but a peaked version of it due to the bath finite size. This peaked frequency dependence encodes the recurrence that will occur in the dynamics of the system because of the reflection at the other boundary. The characteristic time of this recurrence will be given by the round-trip times at the frequencies of the dynamics given by $t_{\rm R} \propto L\partial\gamma/\partial\omega$. In Chapter 4, we will show that this induces a non-trivial back action of our small junction on the bath state. Nevertheless, we postpone these issues for now, and expose the modeling of the transmission lines we are going to use to induce dissipation: Josephson junctions chains.

2.4.5 Josephson junction chains as high impedance transmission lines

Linear regime

As stated before, Josephson junctions chains are 1D arrays composed of a large amount of superconducting junctions, in our case typically several thousands. The non-linear dynamics of these chains constitutes a field of study of its own, and so we will restrict ourselves for now to their linear limit. If the junctions are big enough, $E_J/E_C \gg 1$, we can approximate them as linear oscillators, so that the array becomes a transmission line with an in-line impedance

$$Z_l(\omega) = \frac{-i\omega L_J}{1 - (\omega/\omega_p)^2}, \quad \omega_{\rm p} = \frac{1}{\sqrt{L_J C_J}}, \tag{2.115}$$

and a purely capacitive ground impedance $Z_g(\omega) = -1/i\omega C_g$. The equivalent circuit for a chain of large junctions is given on Fig. 2.17. We now apply the equations of Section 2.4.4 to derive the properties of these arrays. The dispersion relation for the dimensionless wavevector k is plotted on Fig. 2.18 and is given by

$$k(\omega) = -i\sqrt{\frac{Z_l}{Z_g}} = \sqrt{L_J C_g}\frac{\omega}{\sqrt{1 - (\omega/\omega_p)^2}}, \tag{2.116}$$

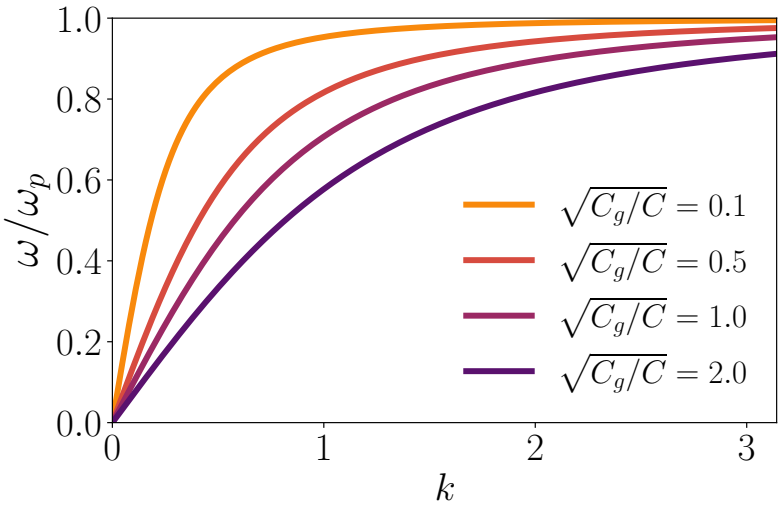

Figure 2.18: Dispersion relation of a Josephson junction chain for varying ratio of the ground capacitance C_G to the junction's capacitance C_J.

and the impedance of the chain is

$$Z_0(\omega) = \sqrt{Z_l Z_g} = \sqrt{\frac{L_J}{C_g}} \frac{1}{\sqrt{1-(\omega/\omega_p)^2}}. \tag{2.117}$$

Note that here we are ignoring the discrete nature of the junctions composing the array; this is valid as long as we are interested in long wavelength $k \ll 1$. With Eqs. (2.116) and (2.117), we see that the plasma frequency ω_p of the junction plays the role of a UV cutoff, and that at low frequencies the chain behaves as an ohmic transmission line of characteristic impedance $\sqrt{L_J/C_g}$. Using modern nanofabrication techniques, it is now routine to fabricate junction chains with $L_J \sim 1\,\mathrm{nH}$ and $C_g \sim 10 - 100\,\mathrm{aF}$, such that high impedances $\sqrt{L_J/C_g} \sim 1 - 10\,\mathrm{k\Omega}$ can be reached experimentally.

Phase transition

One might wonder then if the junctions in the chain stay unaffected by their own high impedance, as we have seen that a single junction becomes an insulator in this regime. Indeed, a phase transition does occur in arrays of Josephson junctions but in this case the critical impedance $Z_C \neq R_Q$ depends on the E_J/E_C ratio since they constitute their own environment [86–90]. Above Z_C the chain turns insulating, and no transport can occur. However, in practice this state is unobservable for junctions with large E_J/E_C [91]. Indeed, taking the $C_g \to 0$ limit, tells us that the total critical voltage of an insulating chain is bounded by the number of junctions times their individual critical voltage, since the junctions decouple in this limit. Because W_0 is exponentially suppressed for big junctions, according to Eq. (2.12), any noise or finite temperature destroys the insulating state [92], akin to the washing out of C_B for a single junction. As such when using arrays of large junctions, we will consider them superconducting no matter their impedance.

Chapter 3

Evidence of dual Shapiro steps in a Josephson junction array

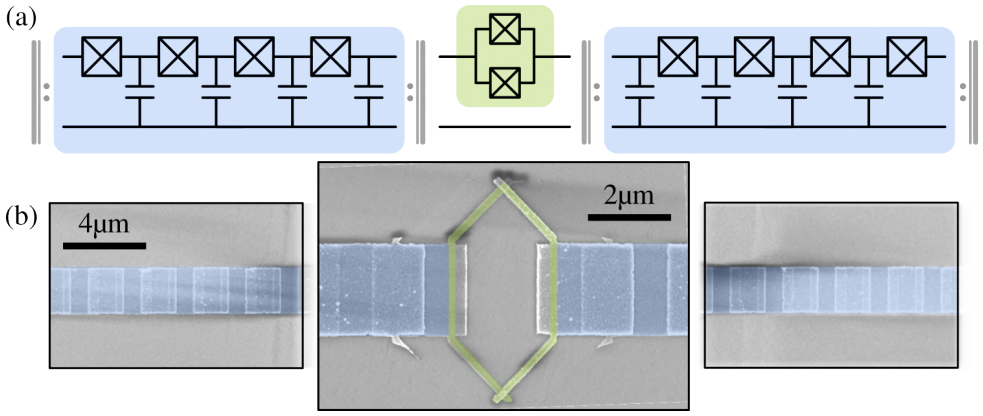

Figure 3.1: Presentation of the sample studied in this chapter which consists of a small junction in a SQUID geometry (green) embedded in a long array of larger junctions (blue). In (a) we show the circuit representation of the sample and in (b) an SEM image of the SQUID and the array.

In this chapter we report the experimental results related to the observation of dual Shapiro steps in a sample made of a small Josephson junction embedded in an array of large junctions. These results represent the first clear evidence of flat dual Shapiro steps since their prediction in 1985 by Averin & Likharev [7], paving a path towards the long-sought closure of the quantum metrology electrical triangle. Additionally, we describe the modeling and measurement of the dc response of a Josephson array under voltage biases large compared to the superconducting gap.

3.1 Sample presentation and experimental setup

The sample we will study in this chapter is presented on Fig. 3.1. It consists of a superconducting quantum interference device (SQUID) made of two small junctions embedded in an array of 7000 large Josephson junctions providing a high-impedance environment. The junctions are $Al/AlO_x/Al$ junctions fabricated using the Dolan bridge shadow evaporation technique [93] on a fused silica wafer with electron beam lithography. The fused silica was used for the substrate instead of the standard silicon in order to minimize the ground capacitance C_g of the Josephson array by taking advantage of the lower dielectric constant of silica. This change yields a reduction by about a factor 4 in C_g. The complete fabrication steps are described in Appendix D. They are similar to the ones from previous works in the Superconducting Circuits group of the Néel Institute (see Refs. [94, 95]) with the addition of a conductive resist layer (Electra 92) on top of the usual resist stack to disperse charges during lithography, fused silica being insulating.

In order to characterize our circuit we cool it down to 23 mK in an inverted dilution fridge. The experimental setup used for this chapter is depicted on Fig. 3.2 with the various temperature stages of the fridge. A photograph of the fridge containing the setup is given on Figure 3.3. I wired this setup at the start of my thesis work with the goal of being able to do transport measurements and radio-frequency (RF) spectroscopy at the same time. This is achieved using two bias tees that split the dc circuit from the RF circuit, which lives in the GHz range. Just after these bias tees, the dc lines contain lumped 45 MHz π-filters and a distributed Ecosorb filter cutting

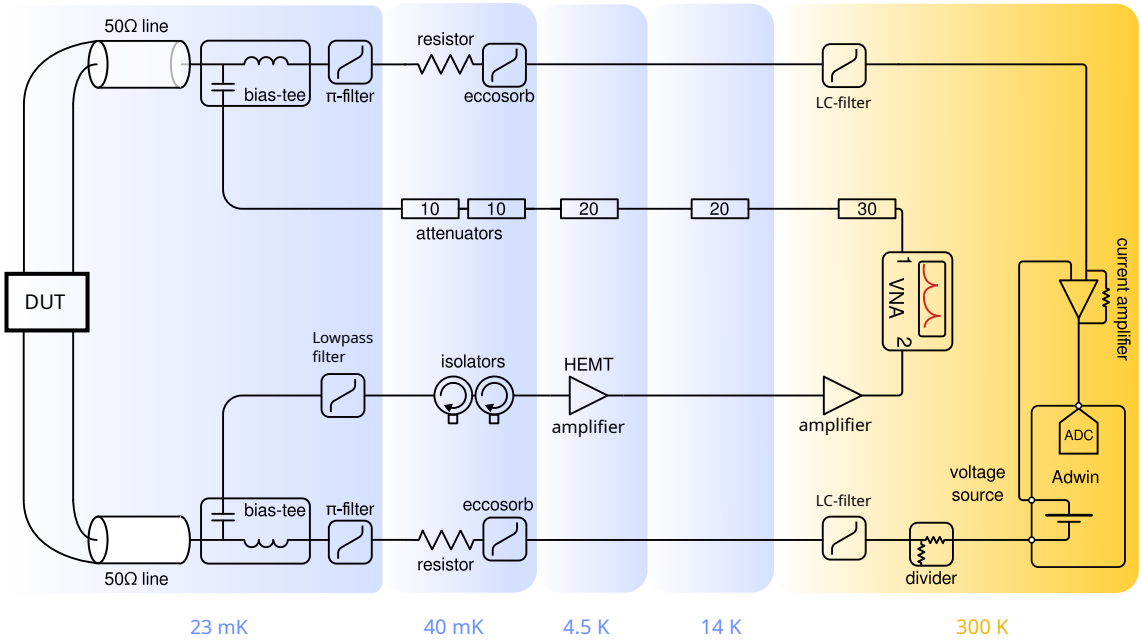

Figure 3.2: Experimental setup used in this chapter. The blue boxes represent the different temperature stages of our dilution fridge.

around 1 GHz. In between these two filters each dc line features a biasing resistor of 50 Ω or 500 Ω, depending on the line. At room temperature, outside the fridge, further filtering is applied through LC and π-filters. The room-temperature filters set the low-pass cutoff frequency of the dc lines which is around 1 kHz. We apply a voltage bias using the digital-to-analog converter (DAC) of a real time processing unit (ADwin-Gold II). The dc current flowing through the dc lines is amplified by a low noise transimpedance current amplifier (Femto DLPCA-200) whose output is read by the analog-to-digital converter (ADC) of the Adwin. The output resolution of the ADwin being $(20\,\mathrm{V})/2^{16} \sim 0.3\,\mathrm{mV}$, we employ homemade voltage dividers to vary our bias range. The microwave measurement lines are attenuated of 20 dB on the input side, at three different temperature stages. The total microwave attenuation is 60 dB allowing the suppression of the thermal noise coming from the exterior. The output part of the lines is composed of two isolators anchored at the lowest temperature stage, these provide 40 dB of backward isolation in the 4–8 GHz frequency range. Just after that, the lines go through a lowpass filter (K&L Microwave 6L250) cutting at 12 GHz. Finally, the output signal is amplified by a high electron mobility transistor (HEMT) amplifier, whose bandwidth is 4–8 GHz. The HEMT noise temperature was estimated, from its datasheet, to be around 5 K with a gain of around 40 dB. Further microwave amplification is done at room temperature. The final bandwidth of the setup for this experiment is 4–8 GHz, set by the HEMT amplifier and the isolators.

3.2 Spectroscopy measurements

After detailing the measurement setup, we now present transmission measurements used to characterize our device. On figure ?? we show the transmission versus frequency of the sample. The peaks in transmission correspond to two of the device's

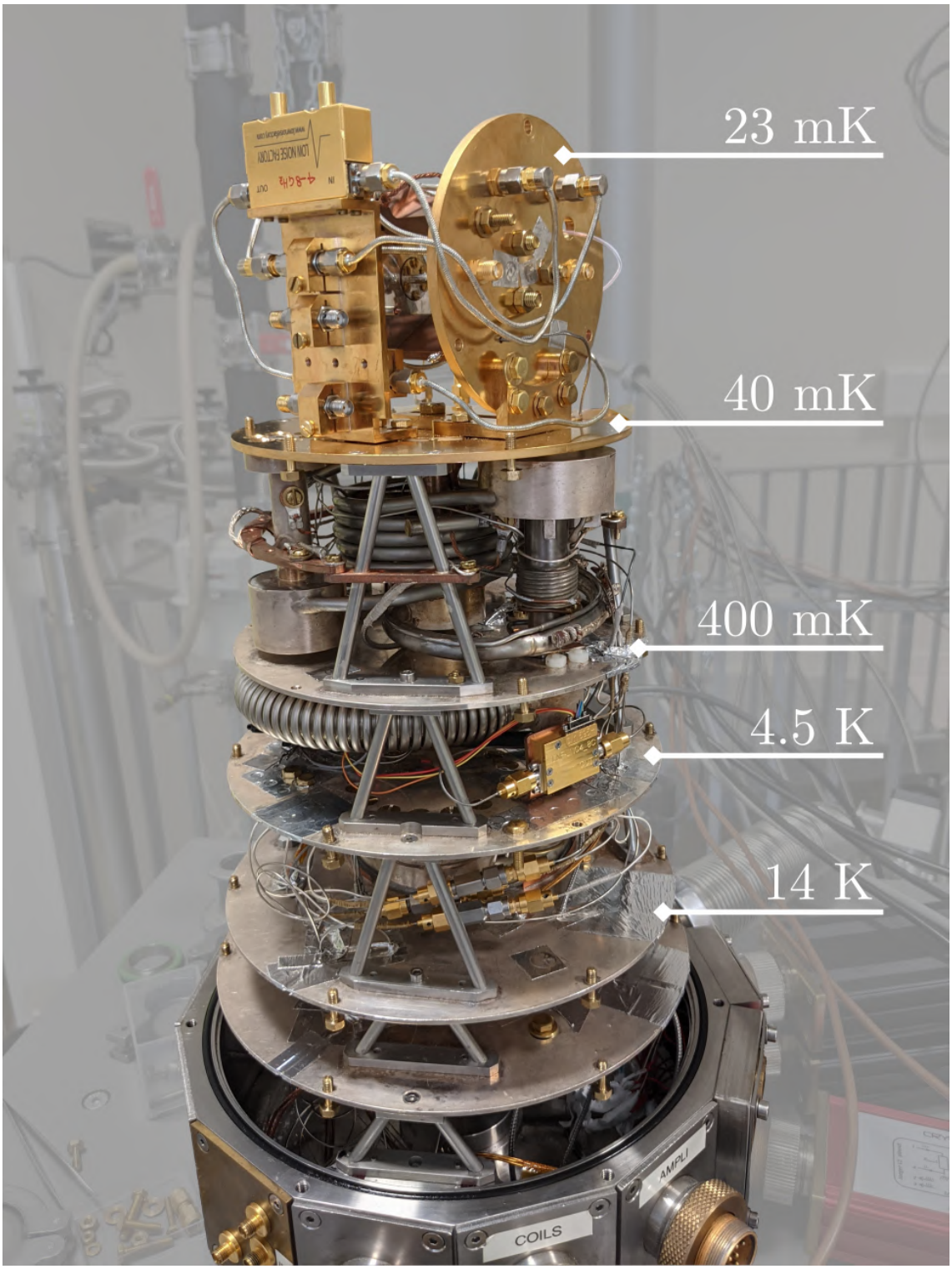

Figure 3.3: Photograph of the dilution fridge used during this thesis. The different stages are labeled with their typical temperatures. The mixing chamber plate (23 mK) is disposed vertically to gain space.

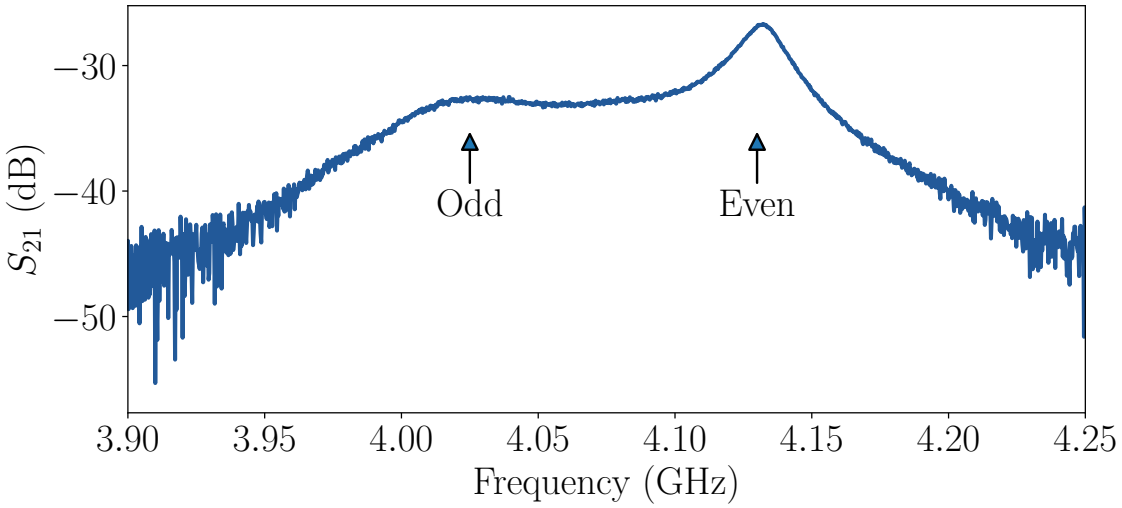

Figure 3.4: Transmission of the sample versus frequency near a mode doublet. The transmission presents two peaks which each corresponds to a mode of the system; the one with the lower quality factor, that we call the odd mode, is the most coupled to the junction.

normal modes. Since we embed our small junction in the middle of an array of length L it creates a system of two weakly coupled $L/2$ transmission lines, such that the modes occur in doublets given by the in-phase or out-of-phase superposition of the transmissions lines' modes. The in-phase modes, that we will also call *even modes*, due to their symmetric voltage profile relative to the center of the line, are decoupled from the small junction in the middle and correspond to the bare modes of the uncoupled $L/2$ transmission lines. On the contrary, the out-of-phase modes, or *odd modes*, are maximally coupled to the impurity and have their frequency shifted compared to the even modes [70]. This shift depends on the impurity impedance seen by the odd modes: if it is inductive, the shift is positive (towards higher frequencies) while if it is capacitive, the shift is negative (see Appendix E for a justification). Due to their coupling to the small junction and its non-linearity, the odd modes are broader than the even modes. Indeed, the non-linearity of the small junction allows for photon conversion processes between odd modes (see the next chapter on the photonic Joule effect), increasing their losses, and leading to a broadening in transmission [96]. Using that we can identify the odd mode on Fig. ?? and infer that the small junction behaves capacitively at this frequency.

Additionally, since the even modes are the bare modes of the (half) array, we can use those to extract the linear properties of the chain. To do this we perform a two-tone measurement: we probe the transmission of the array near an even resonance while varying the power and frequency of an additional applied tone. When this tone aligns with another mode of the array, it influences the transmission at the probe mode, allowing us to measure the frequencies of modes outside our bandwidth. A two-tone measurement is presented on figure 3.5 where we show the transmission at 4.13 GHz versus pump power and frequency. The black regions correspond to a shift of the probed resonance allowing us to directly identify the plasma frequency ω_p of the array at ~ 16 GHz, corresponding to the highest frequency after which the probe mode does not shift anymore. Fitting the dispersion relation of Eq. (2.116) to

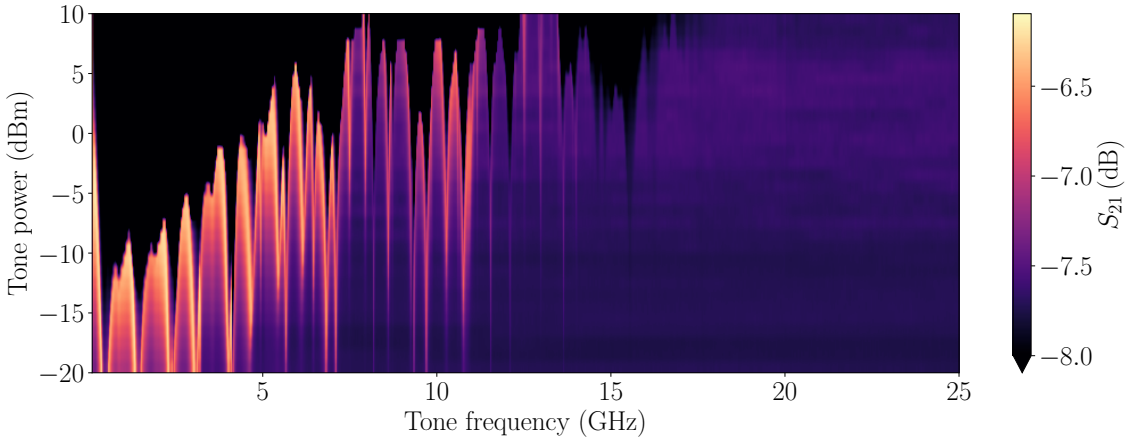

Figure 3.5: A two-tone measurement done by pumping the sample with a microwave tone while measuring its transmission coefficient S_{21} at a fixed probe frequency, corresponding to a mode of the system (here at 4.13 GHz). The pump frequency and power is varied, and we plot the modulus of the transmission coefficient. When the pump tone hits another mode of the system, the probe mode shifts, and a drop in the transmission occurs. This corresponds to the black areas in the figure.

the mode frequencies then gives us the ratio C/C_g. The capacitance to area ratio for C is known empirically in the Néel Institute group to be around $45\,\mathrm{fF}/\mu\mathrm{m}^2$ which, knowing the areas from scanning electron microscope (SEM) imaging, allows us to compute the rest of the parameters. The parameters of the small junctions forming the SQUID are extracted by assuming the same plasma frequency as for the array. We summarize the main ones in table 3.1.

3.3 Transport measurements

We now turn to transport measurements: we apply solely a dc voltage V_0 on the sample and measure the dc current I_0. The obtained IV characteristics for voltage scales ranging from milli-volts to volts are shown on figure 3.6. Beyond $eV_0 = 2N_{JJ}\Delta \approx 3\,\mathrm{V}$ the whole sample turns resistive with $R_{tot} = 8\,\mathrm{M}\Omega$. This gives us

Parameter	SQUID	Array
Area	$0.08\,\mu\mathrm{m}^2$	$1\,\mu\mathrm{m}^2$
Critical current I_C	15 nA	190 nA
Junction capacitance C_J	3.6 fF	45 fF
Inductance L_J	28 nH	2.2 nH
Plasma frequency ω_p	16 GHz	16 GHz
E_J/E_C	1.1	170
Number of junctions N_{JJ}	–	7000
Characteristic impedance Z_c	–	15 kΩ
Ground capacitance C_g	–	8 aF

Table 3.1: Table recapitulating the parameters of the sample studied in this chapter. The values for the SQUID column take into account the two small junctions: for example, the area in the table is twice the area of one small junction.

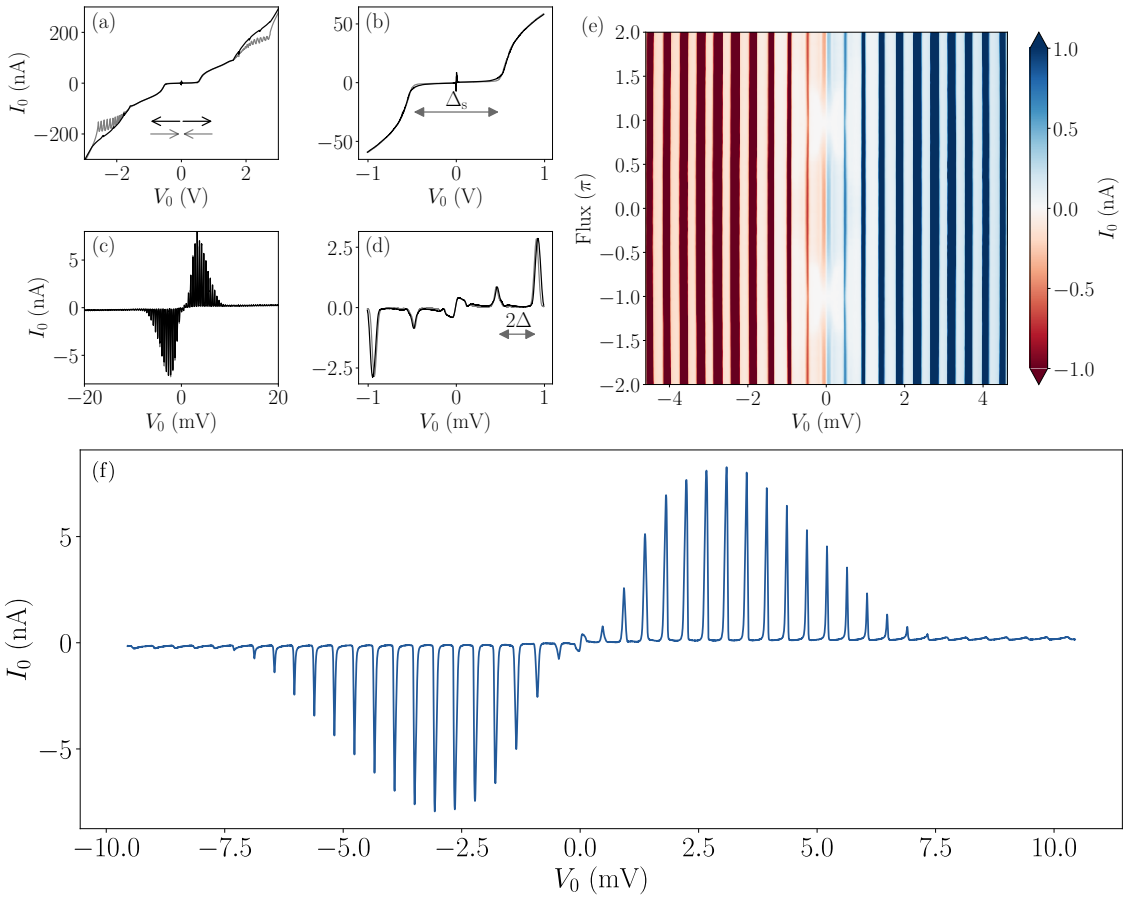

Figure 3.6: Full IV curve at different voltage scales. The arrows in plot (a) indicate the direction of the voltage sweep—toward higher (black) or lower (gray) voltages—to highlight hysteretic features. The voltage scale is gradually reduced from (a) to (d). The system shows a low-conductance plateau of size $\Delta_s \approx 1\,\mathrm{V}$ at large voltages while a forest of peaks, spaced by twice the superconducting gap Δ, emerges at lower bias values. In (f), we offer a better view of the forest of peaks present in (c). Panel (e) shows the flux dependence of the IV curve at low voltages, the flux is normalized with respect to one Φ_0 in the SQUID.

an estimate of the normal state resistance of the big junctions, $R_N = R_{tot}/N_{JJ} \approx 1.1\,\mathrm{k\Omega}$, and so of their critical current through the Ambegaokar–Baratoff formula $I_C = \pi\Delta/2eR_N$ [97]. This gives a critical current of $I_C \approx 290\,\mathrm{nA}$, matching the order of magnitude of the finite-frequency measurements; the discrepancy in the values might arise from thermal or quantum fluctuations [70]. Below this high-voltage regime, the system present a central plateau (b) of size $\Delta_s \approx 1\,\mathrm{V}$, where its resistance is larger than $100\,\mathrm{M\Omega}$. Zooming in, we see appearing a fine structure (c) of current peaks spaced by $2\Delta/e = 0.42\,\mathrm{mV}$ with a smooth envelope. Finally, at low voltages $V_0 < 2\Delta/e$, we detect a current with a non-trivial shape (d), which is not a supercurrent, but that we associated with the small junction since it is strongly modulated with flux, as shown on panel (e) of the figure. The behavior at high voltages (a-b) is not completely understood, although it should be related to that described in Ref. [98] where multiple spatially close junctions switch to their voltage state, creating large clusters spanning several hundreds of junctions. In any case, we are mainly interested in what happens close to low bias (c-d); a broader IV curve

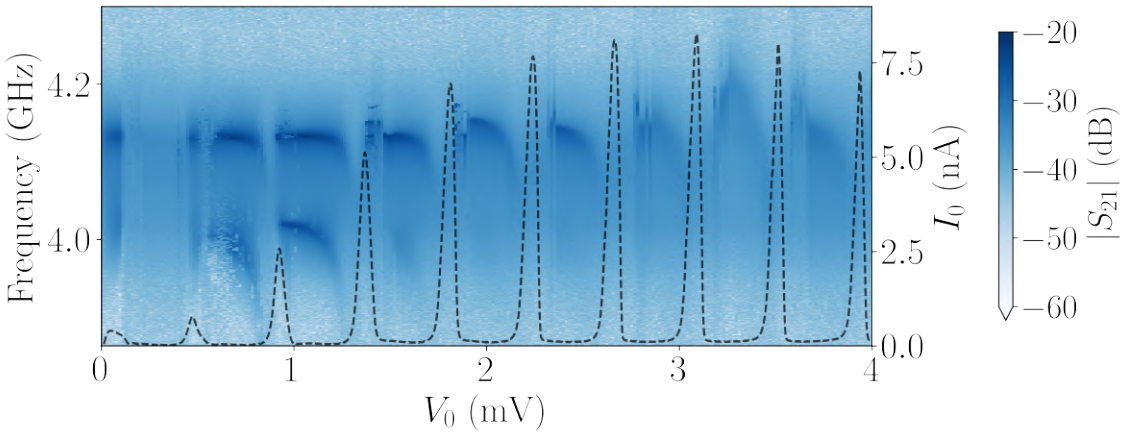

Figure 3.7: Impact of the voltage bias on the mode doublet at 4 GHz. The current I_0 (dashed line) is superimposed to the 2d plot, showing that the current peaks correspond to a rapid degradation of the modes quality factor.

of this region is given in (f). This forest of current peaks was previously observed in works involving chains of junctions under dc bias [91, 99], but no theoretical modeling of this phenomenon existed at the time of measurement (Ref. [98] focuses on the large bias region). Thus, we had to develop it ourselves.

3.4 Theoretical modeling of the 2Δ peaks

The spacing of these current peaks clearly indicates that they are related to the resistive switching of the junctions. This is corroborated by the measurements shown on Figure 3.7 where we plot the transmission of the mode doublet close to 4 GHz versus dc bias. We clearly see that when the bias corresponds to a current peak, the quality factor of the mode degrades quickly. Counterintuitively, it seems that, when we apply a voltage $eV_0 > 2\Delta$ on a chain of junctions, the voltage does not distribute itself equally across each junction as V_0/N_{JJ} but rather that one junction takes on all the voltage drop. To test this, we incorporate the resistive transition due to the superconducting gap in the classical RCSJ model of a Josephson junction by introducing a voltage-dependent resistor [33]. The total current I through a junction is thus:

$$I = C_J \Phi_0 \ddot{\varphi} + f(\dot{\varphi}) \frac{\Phi_0}{R_N} \dot{\varphi} + I_C \sin \varphi, \tag{3.1}$$

with R_N the normal state resistance of the junction, and f is a function which smoothly interpolates between 0 and 1 across the point $|\dot{\varphi}|\Phi_0 = 2\Delta/e$. We found that, for the modeling of the current peaks, the exact form of f does not change the obtained IV curve as long as it is sharp around 2Δ. A computationally efficient choice is a Hill polynomial of the form $f_n(x) = x^n/(1+x^n)$ for $n = 2^k$ [33] (we use $n = 64$ for the rest of this work). The IV curve of a simple circuit consisting of a resistor and a single junction is shown on figure 3.8.

To study the phenomenon in a chain of junctions, we simulate in the same fashion four junctions in series with each other. All the junctions' parameters used in the simulation are nominally identical apart from a very small relative shift in the critical current I_C of each junction. This shift, on the order $10^{-7}\, I_C$, is there to break the

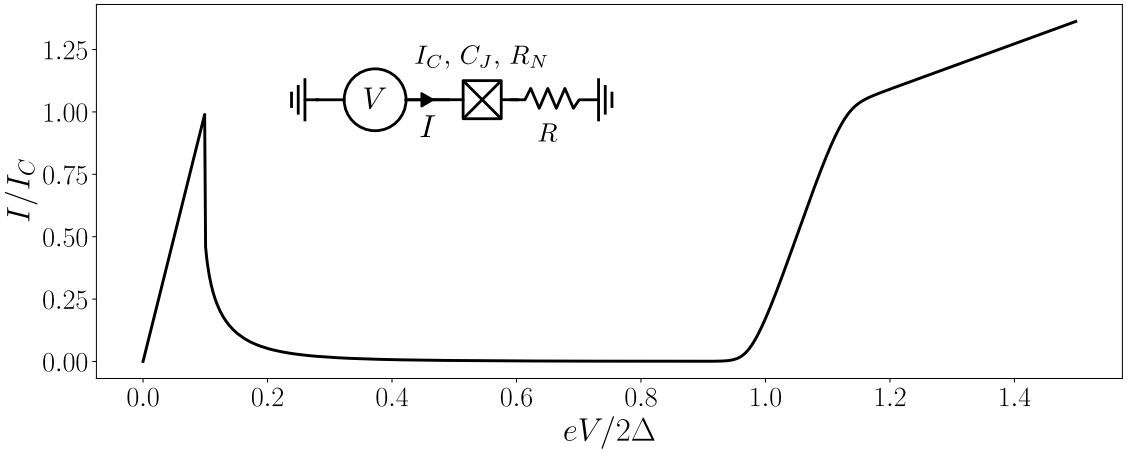

Figure 3.8: IV curve obtained by numerically solving the equations of motion of a circuit, shown on the figure, containing a resistor R and a junction implementing Eq. (3.1). The parameters used for the simulation were $R/R_N = 0.1$, $R^2 C_J I_C/\Phi_0 = 1$ (the ratio squared of the RC_J frequency with the plasma frequency). The gap Δ is fixed by the Ambegaokar-Baratoff formula.

perfect symmetry of the circuit[1]. Without it, the numerical solution does indeed distribute the voltage equally on each junction (since there is no noise present), and the IV is essentially identical to that of figure 3.8, with a single resistive transition at $V = 2N_{JJ}\Delta$. We plot on figure 3.9 the IV curve obtained by numerically solving the equations of motion of such circuit (also shown on the figure). On top of the current I, which displays the resistive peaks, we also plot the voltage distribution in our chain. We clearly see that the voltage does not distribute uniformly among the junction. On peak number n there is exactly n junctions which are turning resistive, since the voltage across them approaches 2Δ, while the others stay in their zero-voltage state, i.e. are superconducting. Just after a current peak, one of the superconducting junction quickly jumps into its finite-voltage state, causing a sharp drop in the current. In this zero-current part, there is $n+1$ junctions in their subgap state where they behave as linear capacitors C_J (assuming no inelastic tunneling takes place). Interestingly, it is not the junction with the smallest critical current (junction 1) which switches first at $eV = 2\Delta$, but rather a random one. This process repeats itself until there is no more junction to switch. While we can reproduce the current peaks, this simple numerical simulation always yield current peaks with constant amplitudes of I_C whereas we find experimentally a non-trivial envelope. This envelope did not arise in any simulation we performed, despite increasing the number of junctions to hundreds, or incorporating a ground capacitance C_g. Thus, it might be caused by fluctuations, or more complicated many-body dynamics, which are not captured by these simulations.

To check the interplay between the current peaks and the dual Shapiro steps we can extend our model to include a QPS element, and an external inductance L. This adds an equation of motion for the charge $\dot{Q} = I$ flowing through the circuit:

$$L\ddot{Q} + R\dot{Q} + V_C \sin\left(\frac{\pi}{e}Q\right) = V(t) - \sum_i \dot{\varphi}_i \Phi_0, \tag{3.2}$$

[1] Anyway, the experimental disorder in critical current is at least on the order of the few percent, due to fabrication variability.

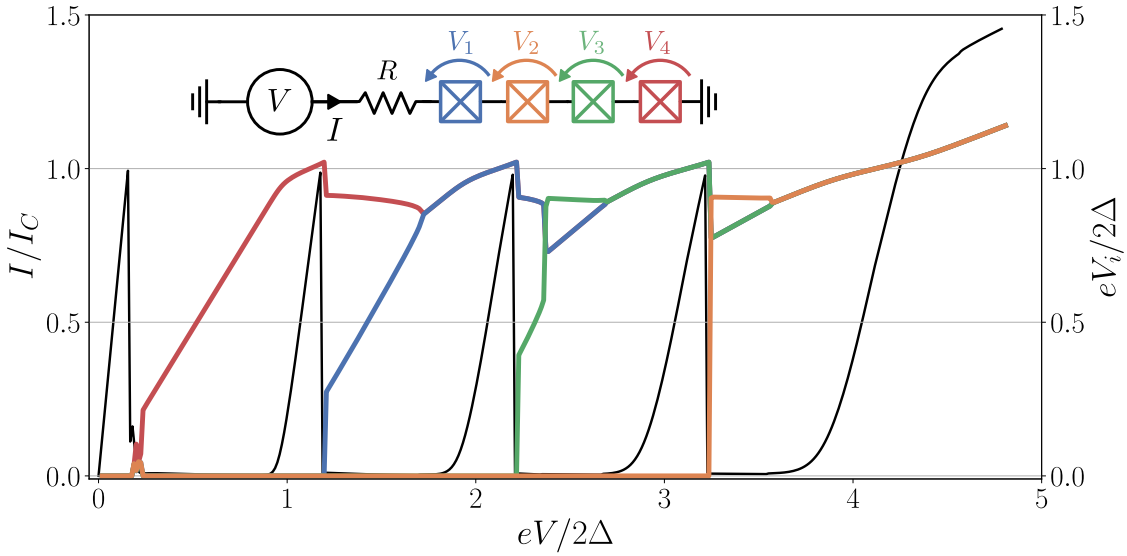

Figure 3.9: Simulation of a chain of four junctions in series with a resistor R. The junctions are identical to each other except in critical current I_C where a small relative shift of $i \times 10^{-7}\, I_C$ is added to the i-th junction to break the symmetry of the circuit. The others parameters are identical for all junctions with $R/R_N = 0.2$, and the damping rate squared $R^2 C_J I_C/\Phi_0 = 1$. We plot in black the dc current I (left y-axis) flowing through the circuit versus the applied voltage V. We also plot, in color, the voltage drop V_i (right y-axis) across each junction as a function of the bias, showcasing the successive resistive switching of each junction.

where now the voltage bias can contain an ac component $V(t) = V_{\mathrm{dc}} + V_{\mathrm{ac}} \sin \omega_{\mathrm{ac}} t$. The IV curve of this circuit is plotted on figure 3.10, with and without the ac tone applied. We see that the current steps appear before each current peak when driving the circuit. Indeed, as we saw before, on a current peak the junctions in the chain behave either as resistors or as inductors, and thus the QPS can exhibit dual Shapiro steps at each peak, although with increased damping as more junctions turn resistive.

3.5 Response to microwave irradiation

Having developed a qualitative understanding of the current peaks and their possible interplay with dual Shapiro steps, we return to our experiment. Our goal now is to apply an ac tone to our sample in order to drive the small junction in the middle of it. This is achieved by strongly pumping the odd modes of the system, which exhibit the strongest coupling to the central junction and thereby enable efficient power transfer. In Figure 3.11, we plot the evolution of the transmission near the mode doublet of 4 GHz that we showed on Figure ??. In panel (a), we study the evolution of the transmission with respect to the frequency of the pump while keeping the pump strength fixed at $p = -5\,\mathrm{dBm}$. When the tone is close to the odd mode $4.02\,\mathrm{GHz} \leq f \leq 4.11\,\mathrm{GHz}$, we observe a repulsion between the mode and the pump. At the same time, a linewidth locked with the pump appears, as can be seen by the thin dark line of slope 1 present in (a). This linewidth only appears at sufficiently high power, and that is what we study in (b) and (c). Here we plot

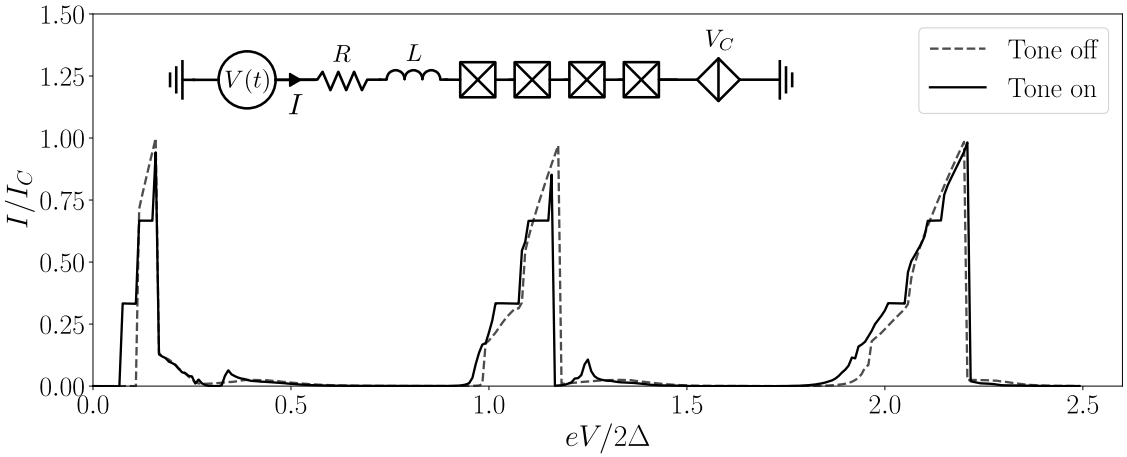

Figure 3.10: Numerical simulation of the circuit, drawn on the figure, containing a resistor R, an inductor L, a QPS element of critical voltage I_C, and four junctions implementing the resistive transition. The voltage bias $V(t)$ is either purely dc (dotted lines) or contains an ac drive $V(t) = V + V_{\rm ac} \sin \omega_{\rm ac} t$ (full lines). The parameters used for this figure are $R/R_N = 0.2$, $R^2 C_J I_C/\Phi_0 = 1$ (the ratio squared of the RC_J frequency with the plasma of the junctions), $V_C/RI_C = 0.7$, $\pi L V_C/eR^2 = 4.2$ (the ratio squared of the RL frequency with the characteristic frequency of the QPS), for the circuit elements. For the ac tone, the parameters are $V_{\rm ac}/RI_C = 0.7$, and $\omega_{\rm ac} = 2RI_C/\Phi_0$, yielding steps at quantized currents $I = n \times I_C/3$.

the variation of transmission when we sweep the pump power p at a fixed frequency of $f = 4.04\,\text{GHz}$. At low powers $p < -30\text{dBm}$, we recover the linear regime of our system which survives until $p \simeq -20\text{dBm}$ where the transmission spectrum shows a strong interplay of the pump with the odd mode, akin to a Fano resonance. Further increasing the pump strength, we eventually see the appearance of the linewidth at $p \simeq -5\text{dBm}$. We interpret this as the locking of Bloch oscillations onto our pump tone and now look at the IV curve for $p = -5\text{dBm}$ and $f = 4.04\,\text{GHz}$. The measurement result is displayed on (d), and we see the emergence of current plateaux, aligned with $2ef$, before each resistive peak.

Although these current steps coincide with appearance of the linewidth around the pump, we further assess the stability of the steps by looking at their power dependence. In figure 3.12a, we show the influence of the power on the step height. We also measure experimentally the derivative dI_0/dp using a lock-in. We modulate very weakly the pump tone in amplitude with a low frequency ($f < 200\,\text{Hz}$) carrier. The current I_0 is then demodulated using a Stanford Instrument lock-in amplifier (SR830), giving us access to the derivative that we plot on panel (b). It is clear that the emergence of the linewidth, and of the current steps aligned with $2ef$, are concomitant with the minimum of the derivative with respect to power.

We repeat the same procedure for all the available modes in our $4-8\,\text{GHz}$ bandwidth, and find three other working points where current steps appears before each 2Δ-peak, for $f = 3.20\,\text{GHz}$, $4.04\,\text{GHz}$, $5.45\,\text{GHz}$ and $6.46\,\text{GHz}$. The first current step for each frequency, apart from $5.45\,\text{GHz}$, is plotted on panel (c). The step at $5.45\,\text{GHz}$ is not shown, for the sake of clarity, because the corresponding IV curve suffer from a much greater noise, akin to switching between bistable states, than the other three frequencies. In any case we can plot the current step versus pump

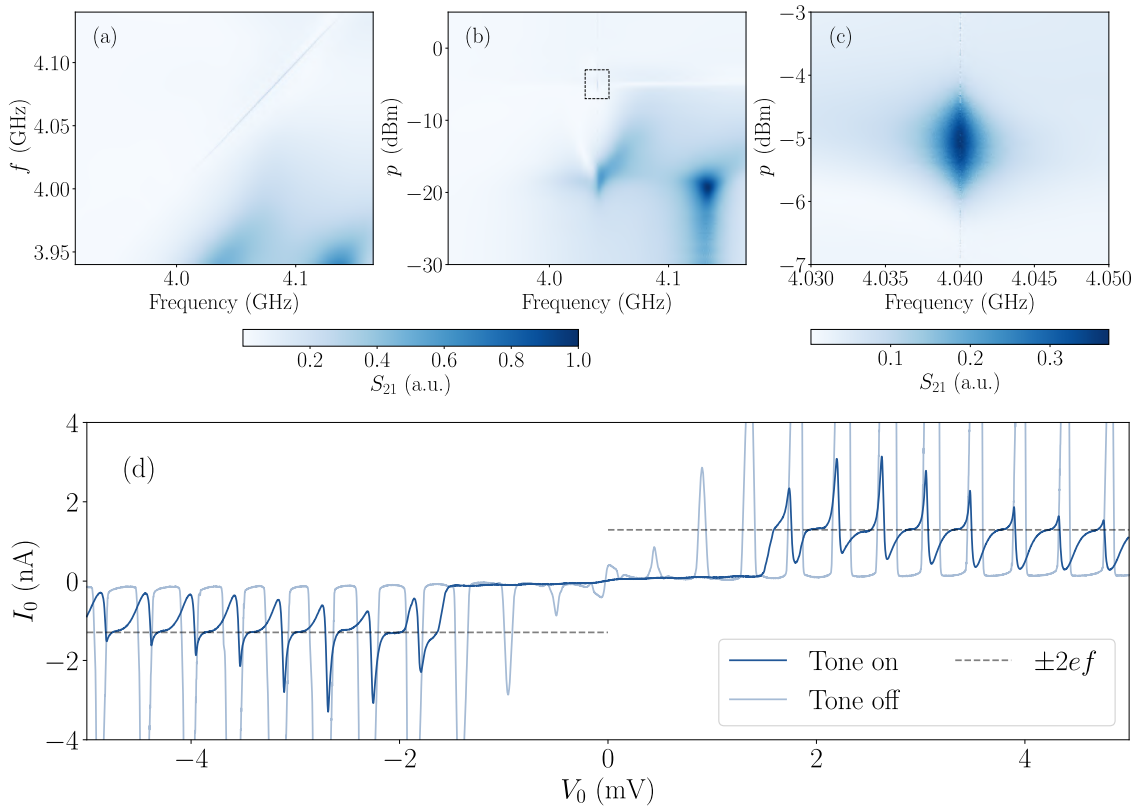

Figure 3.11: Influence of a pump tone on the transmission and transport measurements. In (a) the frequency of the external tone f is changed to observe the effect it has on the transmission spectrum of the system measured with a VNA. While in (b), we vary the power p of the tone at a fixed frequency $f = 4.04\,\mathrm{GHz}$. The dashed rectangle highlights the plot region reported in (c), where the appearance of the linewidth synchronized with the pump is clearly visible. Plot (d) shows the IV characteristics measured, with and without the tone, for $f = 4.04\,\mathrm{GHz}$ and $p = -5.0\,\mathrm{dBm}$. The plateau's current is $\pm 2ef$, as is evidenced by the gray dashed lines.

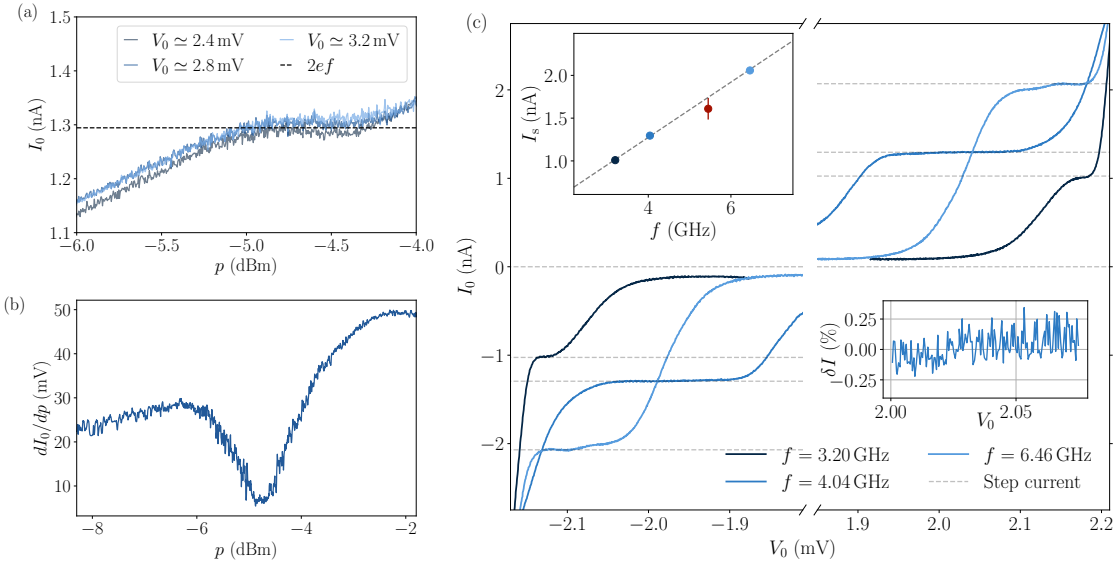

Figure 3.12: Current plateaux at different microwave tone frequency and power. (a) Average plateaux current at different microwave powers p for three separate voltages. (b) Lock-in measurement collected by modulating the microwave power p and detecting the corresponding current variation at $V_0 = 2.4\,\mathrm{mV}$. (c) For three different values of f we follow the procedure described in the text to observe current plateaux whose amplitude correspond to the one of the first dual Shapiro step, which is shown as a grey dashed line. The inset shows the relation between the step current I_s and tone frequency, and the fitted slope is consisted with $2e$. The red point's IV curve was omitted for clarity (see the main text for further details).

frequency and fit the linear relationship, as shown on the inset of figure 3.12c. The slope of the fitting line is $(3.23 \pm 0.07) \times 10^{-19}$ C, giving us an estimate of the charge of a Cooper pair. The average deviation from the expected current $\delta I = I_0/2ef - 1$ on the 4 GHz step is $\langle \delta I^2 \rangle^{1/2} \leq 0.001$, limited by the setup noise in an averaging time of one minute (see inset of figure. 3.12c).

3.6 Conclusion and open questions

In this chapter, combining finite frequency with transport measurements, we have studied the dynamics of a small junction embedded in a Josephson array. We have shown that the discrete switching of the junctions in the array gives rise to current peaks in the IV curve, and that, under irradiation by a strong pump tone, quantized current steps arise before each of these peaks, following the dual Shapiro step relation $I = 2ef$. While the current steps are quantized within less than a percent, several changes could be made to improve the process. First, we are pumping through the array to drive the small junction in the middle. Thus, a significant fraction of the RF power is absorbed by our array, forcing us to use fairly high powers to exhibit the steps (around -70 dBm applied at the sample) which inhibit the superconducting state of the junctions in the array (for example, see the strong reduction of the current peaks when a tone is applied on figure 3.11d). This strongly constrains our working range, and possibly drives the junctions in the array out of their linear regime. One solution to this problem is to directly couple the drive line to the small junction in the middle through small capacitors (see Refs [56, 57]), limiting the power leaked to the rest of the array. Secondly, the working frequencies are set by the resonant modes of the system. Although this might not be a critical problem, it stills limit the working dynamical range. This could be solved through longer arrays, which would increase the modal density, or by impedance matching at the array, which would broaden the discrete modes in a continuum.

Moreover, at the level of physics, a few fundamental questions remains open:

- What is the role of the array? At these drive powers, it is hardly a linear transmission line anymore. Strongly pumping on the even modes does not yield current steps, nor the locking to the pump tone, so the small junction seems critical to the process, but the array dynamics might induce a non-trivial contribution.

- What determines the step widths? In all our numerical simulations, the step size is given by the critical voltage of the QPS element with a factor always smaller than one. Here, using the parameters of table 3.1, we expect a $V_C \approx 30\,\mu V$, which is consistent with the step size for all pump frequencies, except for $f = 4.04$ GHz where the step size is almost $200\,\mu$V.

- Which junction turns resistive, and is this order impacted by the pump? In our simple simulations of Section 3.4, the order seemed truly random and strongly dependent on the initial conditions. However, one can wonder if this is still the case when voltage fluctuations, which are not uniform in our system, are taken into account. Additionally, the drive tone will generate a non-uniform voltage profile in the array, possibly skewing the switching towards junctions with a large field gradient across them.

- What determines the envelope of the current peaks? As we discussed in Section 3.4, the envelope does not arise in the numerical simulations we performed, all peaks have the same height.

- Why do the low voltage currents not present a blockade? In principle, we expect a blockade on the order of V_C. Here we observe a finite current at low voltages, see figure 3.6d.

All these questions are significant on their own, but for the remainder of this thesis, we have chosen to focus on the last one. As we will see in the next chapter, it turns out that the finite size of our array induces an overheating of the mode populations when applying a small voltage bias on the small junction. This heating problem disappears at larger voltages, where we see the current steps, as the resistive switching of multiple junctions lowers the quality factor of our modes, as can be seen on Figure 3.7.

Chapter 4

Photonic Joule effect

4.1 Statement of the problem

In this chapter we address the back-action of a small junction dynamics on its environment. As we mentioned in Section 2.3.7, a popular choice for implementing a dissipative environment in circuit QED are superconducting transmission lines. These transmission lines mainly dissipate through their coupling with $50\,\Omega$ external circuit, which occurs at their boundary and so is independent of the line length. When the power injected by the small junction exceeds the cooling rate of the transmission line, the bath is driven out of equilibrium, and a non-trivial steady state emerges. As we will see, this can significantly alter the IV characteristic, washing out the low-energy features of a junction, such as its Coulomb blockade. The back-action of the junction on its many-body electromagnetic environment under voltage bias has, to date, only been investigated in Ref. [69], where the environment consisted of a resistor coupled to a junction. In that work, the resistor experienced only weak overheating, leading to a minor correction to the IV curve. A comprehensive theoretical treatment of overheating in the case of a transmission line environment was, however, still lacking—motivating the studies presented in this chapter. Unlike the typical overheating of phonons or electrons for a resistor due to current flow, this phenomenon only involves the overheating of the photons in the line[1]. Thus, by analogy with the conventional effect, we refer to it as the *photonic Joule Effect*.

In order to study it, we first present three different theoretical approaches, with increasing degree of complexity, that were developed during the thesis. We then confront the theory with experiments done on three samples with the same geometry as in the previous chapter: a small junction embedded in a Josephson junction chain, acting as our transmission line.

4.2 Theory

4.2.1 Model

In the following subsections we will consider a voltage-biased small Josephson junction coupled to a harmonic bath of finite size: a chain of N junctions. The bath is itself coupled to the rest of the universe, represented by the external circuit. The circuit is sketched on Figure 4.1, and its full Hamiltonian can be written as

$$\begin{aligned}\hat{\mathcal{H}} = & -E_J \cos\left[\frac{2e}{\hbar}Vt - \hat{\phi}\right] + \sum_m^N \hbar\omega_m \hat{a}_m^\dagger \hat{a}_m \\ & + \int_0^\infty d\omega \left[\hbar\omega\, \hat{b}_\omega^\dagger \hat{b}_\omega + \sum_m \hbar\sqrt{\frac{\kappa_m}{2\pi}}\left(\hat{a}_m^\dagger \hat{b}_\omega + \hat{b}_\omega^\dagger \hat{a}_m\right)\right],\end{aligned} \tag{4.1}$$

with the $\hat{a}_m$ and $\hat{b}_\omega$ operators corresponding to the bosonic operators for the chain and the external circuit, respectively. We adopt the convention where the small junction's capacitance is absorbed in the harmonic bath, similar to what we described in Section 2.3.4 for the $P(E)$ theory. This means that ω_m and κ_m correspond,

[1] As we will show in 4.2.6, the quasi-particles of our superconducting electrodes do not overheat, as long as $\hbar\omega_p \ll \Delta$.

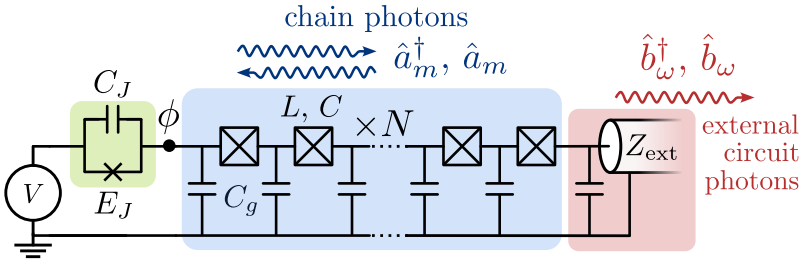

Figure 4.1: The full circuit considered for the photonic Joule effect in this chapter. A voltage-biased small junction (green), of Josephson energy E_J and capacitance C_J, is coupled to a long chain made of N large junctions (blue). The junctions in the chain are considered in their linear regime, characterized by their inductance L, self-capacitance C, and ground capacitance C_g. The photons in the chain thermalize thanks to the coupling with external lines of impedance $Z_{\rm ext}$ (red).

respectively, to the normal modes frequencies and losses of the finite-length chain terminated on one end by a capacitance C_J and by a resistance $Z_{\rm ext} = 50\,\Omega$ on the other. Additionally, the phase $\hat{\phi}$ is expressed as a linear combination of the modes operators $\hat{\phi} = \sum_m \Lambda_m(\hat{a}_m + \hat{a}_m^\dagger)$. The coupling constants Λ_m are related to the infinite-size limit of the chain impedance $Z_0(\omega)$, given by Eq. (2.117), through (see Appendix F for the derivation)

$$\Lambda_m^2 = 2\frac{\Delta\omega_m}{\omega_m}\frac{\mathrm{Re}\, Z_t(\omega_m)}{R_Q}, \tag{4.2}$$

with $Z_t(\omega) = 1/[1/Z_0(\omega) - i\omega C_J]$ representing the impedance seen by the junction, and $\Delta\omega_m = \omega_{m+1} - \omega_m$. The frequencies ω_m follow the dispersion relation $\omega(k)$ of Eq. (2.116) which gives

$$\Delta\omega_m \overset{N\gg 1}{=} \frac{\pi}{N}\frac{d\omega}{dk} = \frac{\pi}{N\sqrt{LC_g}}\left(1 - \frac{\omega^2}{\omega_p^2}\right)^{3/2}. \tag{4.3}$$

The losses κ_m can be estimated by noting that the energy stored at a given frequency ω is decreased by the coefficient $R(\omega) = |Z_{\rm ext} - Z_0(\omega)|^2/|Z_{\rm ext} + Z_0(\omega)|^2$ after a round trip time $t_R = 2\pi/\Delta\omega_m$. In the large N limit we thus have $R(\omega_m) = e^{-\kappa_m t_R}$, yielding

$$\kappa_m = \frac{\Delta\omega_m}{2\pi}\ln R(\omega_m) \approx \frac{2}{\pi}\frac{Z_{\rm ext}}{Z_0(\omega_m)}\Delta\omega_m, \tag{4.4}$$

where we used $Z_0 \gg Z_{\rm ext}$ for the approximation. We also note that $\Delta\omega_m \propto 1/N$ so κ_m, $\Lambda_m^2 \propto 1/N$. Moreover, since $\Delta\omega_m$ vanishes at ω_p, only the modes in the acoustic (linear) part of the dispersion are effectively coupled to the small junction while the ones with $\omega_m \approx \omega_p$ decouple. For the same reason, the loss rates κ_m also vanish at $\omega_m \to \omega_p$, possibly making these plasma modes long-lived. In reality, these modes are damped by the bulk losses of the chain which can be modeled as a very small admittance shunting each junction in the chain. To account for that, we add a small, but constant, part to the losses $\kappa_m \to \kappa_m + \omega_p/Q_{\rm int}$ through an internal quality factor that we fix at $Q_{\rm int} = 2\times 10^4$ for the rest of the section.

With these microscopic details sorted out, we now expose three treatments of the photonic Joule effect. In each case the main goal will be to compute the IV curve and the steady-state photonic populations $\bar{n}_m = \langle \hat{a}_m^\dagger \hat{a}_m \rangle$.

4.2.2 Single-temperature ansatz

The conventional $P(E)$ theory assumes that the bath coupled to the junction is unaffected by the Cooper pair tunneling, staying in a thermal state at all times. A straightforward extension of this to include the back-action of the junction is to still suppose that the bath is in a thermal state, but now with a time-dependent temperature $T(t)$. Assuming that the junction is coupled to N_{eff} modes with similar loss rates $\kappa_m \approx \kappa$, the energy balance condition for the bath yields [69]

$$\frac{dE}{dt} = -\kappa E + IV, \quad E = \sum_m^{N_{\text{eff}}} \hbar\omega_m \bar{n}_m. \tag{4.5}$$

The number of coupled modes N_{eff} can be estimated as the number of modes on the acoustic branch of the dispersion relation, $N_{\text{eff}} \approx \omega_p/\Delta\omega_1 \approx N\omega_p\sqrt{LC_g}/\pi$. We can further simplify by assuming that the temperature will be high enough, $k_BT \gtrsim \hbar\omega_p$, so that the classical equipartition of energy applies, $\hbar\omega_m\bar{n}_m \approx k_BT$. This gives us the dynamical equation for the temperature:

$$N_{\text{eff}}k_B\frac{dT}{dt} = -\kappa N_{\text{eff}}k_BT + IV. \tag{4.6}$$

In our case, we are interested in describing small junctions, so the temperature-dependent current I can be determined by using the $P(E)$ theory that we described in Section 2.3.4. The steady state temperature T_0 is obtained by imposing $dT/dt = 0$, yielding

$$\kappa N_{\text{eff}}k_BT_0 = I(V, T_0)V \tag{4.7}$$

Importantly, the product κN_{eff} does not depend on the bath size N, so T_0 is the same no matter the length of the chain, again because the bath thermalizes through its boundary with the external circuit[2]. The current $I(V, T)$ is computed using $P(E)$ [see Eq. (2.72)], yielding the self-consistency condition (we use $Z_0(0) = Z_c = \sqrt{L/C_g}$)

$$k_BT_0 = \pi^2 eV\frac{Z_{\text{ext}}}{Z_c}\frac{E_J^2}{\hbar\omega_p}\left[P(2eV, T_0) - P(-2eV, T_0)\right], \tag{4.8}$$

with the P function defined by Eq. (2.65). The correlator $J(t)$ appearing in Eq. (2.67) is now, in principle, a discrete sum

$$J(t) = \sum_m J_m(t) = \sum_m \Lambda_m^2\left[(2\bar{n}_m + 1)(\cos\omega_m t - 1) - i\sin\omega_m t\right]. \tag{4.9}$$

However, using Eq. (4.2), in the long chain limit $N \gg 1$ we recover the continuum expression, so we approximate the $P(E)$ function appearing in Eq. (4.8) by the one computed using the smooth impedance Z_t. We discuss the validity of this approximation further down in subsection 4.2.6. Using this, we solve Eq. (4.8) numerically, and plot the obtained dc current I_{dc} and T_0 on Figure 4.2. We see that the IV curve of the overheated environment differs significantly from the one for $T = 0$, with photonic temperatures reaching well above the Kelvin scale (in

[2]While the steady-state of the system does not depend on its size, the characteristic time taken to reach this steady-state does scale. As can be read from Eq. (4.6), we have $t_{\text{charac}} \propto N_{\text{eff}}$, which makes sense since the round-trip time of the transmission line is proportional to N_{eff} as well.

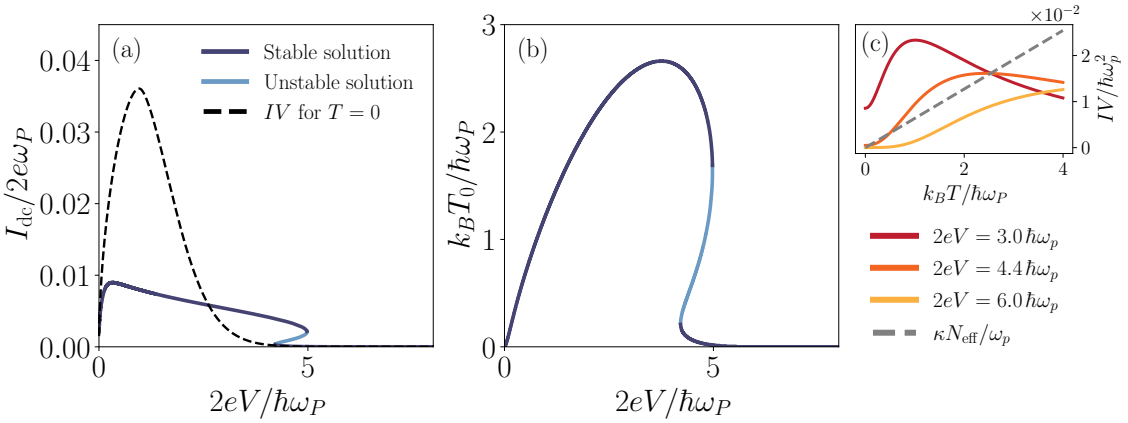

Figure 4.2: Steady-state dc current (a) and temperature (b) versus voltage, found by solving Eq (4.8), with the parameters $E_J = 0.2\,\hbar\omega_p$, $C_J = 2\,\mathrm{fF}$, $Z_c = 5\,\mathrm{k}\Omega$, $C/C_g = 1600$, and $Z_{\rm ext} = 50\,\Omega$. Due to the bath overheating, the current differs greatly from the zero temperature $P(E)$ solution, shown by a black dashed line. We plot on (c) the dependence of the power $IV = eV\pi E_J^2[P(2eV, T) - P(-2eV, T)]/\hbar$ on the temperature of the bath T for three bias values. The steady-state solutions to Eq. (4.6) are determined by the intersection with the gray dashed line of slope $\kappa N_{\rm eff}/\omega_p$. Depending on the bias value, up to three solutions can exist (see the curve for $2eV = 4.4\,\hbar\omega_{\rm p}$), yielding a bistable region in (a) and (b).

our circuits $\hbar\omega_p \approx 1\,\mathrm{K}$), and even exhibiting a bistability at high voltages. In the bistable region, three solutions T_0 of Eq. (4.8) exist, two are stable and one is unstable. This should be characterized by an experimental hysteric behavior in the IV when sweeping the voltage.

This simple calculation tells us that the bath state is strongly affected by the small junction dynamics, and heats up significantly. In order to refine the modelling, we now have to relax the assumption that all modes have the same temperature, taking into account the frequency dependence of κ_m, $\bar{n}_m$ coming from the dispersion relation of the chain or from the cutoff due to the small junction's capacitance C_J. Indeed, this other frequency scale $1/Z_cC_J$, serves as a high-frequency cutoff, and could skew the dynamics towards lower frequencies.

4.2.3 Kinetic equations

In order to gain insight on the frequency dependence of the dynamics, we write a kinetic equation for the average occupancy of each mode $\bar{n}_m(t)$. We still assume that the non-linearity of the system is small enough allowing us to consider a diagonal density matrix in the Fock basis of each mode. On top of that, we still neglect intermodal correlations and suppose that the full density matrix of the bath is separable $\hat{\rho} = \hat{\rho}_1 \otimes \hat{\rho}_2 \otimes \cdots \otimes \hat{\rho}_N$.

With these assumptions we can compute the transition rate $\Gamma_{n_m \to n_m + l}$ between $|n_m\rangle$ and $|n_m + l\rangle$ for the m-th mode by applying the Golden rule to the Josephson

term of Hamiltonian (4.1):

$$\Gamma_{n_m\to n_m+l} = \frac{\pi E_J^2}{2\hbar}\left[\left|\langle n_m+l|e^{i\Lambda_m(\hat{a}_m+\hat{a}_m^\dagger)}|n_m\rangle\right|^2 P(2eV-l\hbar\omega_m) + \left|\langle n_m+l|e^{-i\Lambda_m(\hat{a}_m+\hat{a}_m^\dagger)}|n_m\rangle\right|^2 P(-2eV-l\hbar\omega_m)\right]. \tag{4.10}$$

This equation tells us that each individual mode sees the others as a dissipative bath, allowing it to absorb $l\times\hbar\omega_m$ from the voltage bias while dumping the rest of the energy into this bath. Thus, the corresponding correlations $J(t)$ of the $P(E)$ functions appearing in the right-hand side should be computed without counting the contribution of the m-th mode, that is $J(t)=\sum_{k\neq m}J_k(t)$. However, in the long-chain limit, over-counting the contribution of a single mode gives an error only on the order of $\Lambda_m^2\propto 1/N$, for most modes (see the discussion at the end of this section). As such, we define our $J(t)$ function in this subsection as in Eq. (4.9) with the continuum limit

$$J(t)=2\int_0^{+\infty}\frac{d\omega}{\omega}\frac{\mathrm{Re}\,Z_t(\omega)}{R_Q}\left[(2\bar{n}(\omega)+1)(\cos\omega t-1)-i\sin\omega t\right]. \tag{4.11}$$

The matrix elements of the displacement operators $e^{\pm i\Lambda_m(\hat{a}_m+\hat{a}_m^\dagger)}$ can be expressed in terms of generalized Laguerre polynomials [80, 100]

$$\left|\langle n_m+l|e^{\pm i\Lambda_m(\hat{a}_m+\hat{a}_m^\dagger)}|n_m\rangle\right|^2=\frac{n_m!}{(n_m+l)!}e^{-\Lambda_m^2}\Lambda_m^{2l}\left[L_{n_m}^{(l)}(\Lambda_m^2)\right]^2. \tag{4.12}$$

The transition rate $\Gamma_{n_m\to n_m+l}$ is of order $\Lambda_m^{2l}\propto 1/N^l$ at least, unsurprisingly. Consequently, in the large N limit, we anticipate that only the rates with $l=\pm1$ will matter. Using the value of the Laguerre polynomial $L_n^{(l)}(0)=\binom{n+l}{n}$ gives us to second order[3]

$$\Gamma_{n_m\to n_m\pm1}=\left(n_m+\frac{1}{2}\pm\frac{1}{2}\right)\Gamma_m^{\pm}, \tag{4.13}$$

$$\Gamma_m^{\pm}=\Lambda_m^2\frac{\pi E_J^2}{2\hbar}\Big[P(2eV\mp\hbar\omega_m)+P(-2eV\mp\hbar\omega_m)\Big]. \tag{4.14}$$

In the end, the probability p_{n_m} to find n_m photons in mode m obeys the following rate equation:

$$\frac{\partial p_{n_m}}{\partial t}=\left[\Gamma_{n_m+1\to n_m}+\kappa_m(n_m+1)\right]p_{n_m+1}+\Gamma_{n_m-1\to n_m}\,p_{n_m-1} -\left(\Gamma_{n_m\to n_m+1}+\Gamma_{n_m\to n_m-1}+\kappa_m n_m\right)p_{n_m}, \tag{4.15}$$

where we added the decay due to the losses κ_m. Multiplying by n_m and summing over the probabilities gives us the kinetic equation for the average occupancies $\bar{n}_m$:

$$\frac{\partial\bar{n}_m}{\partial t}=\Gamma_m^+(\bar{n}_m+1)-(\Gamma_m^-+\kappa_m)\bar{n}_m. \tag{4.16}$$

[3]The coefficient for $l=-1$ is found by just shifting n_m by l in Eq. (4.12).

The steady-state occupancies satisfy the system of self-consistent equations[4]

$$\bar{n}_m = \frac{\Gamma_m^+}{\Gamma_m^- + \kappa_m - \Gamma_m^+}, \tag{4.17}$$

which again do not depend on N in the thermodynamic limit since $\Gamma^\pm, \kappa_m \propto 1/N$. This prompt us to take the thermodynamic limit of Eq. (4.16) by multiplying with the modal density $\nu(\omega_m) = 1/\Delta\omega_m$ to get

$$\nu(\omega)\frac{\partial \bar{n}(\omega)}{\partial t} = -\kappa(\omega)\bar{n}(\omega) + \left[\Gamma^+(\omega) - \Gamma^-(\omega)\right]\bar{n}(\omega) + \Gamma^+(\omega), \tag{4.18}$$

$$\Gamma^\pm(\omega) = \frac{E_J^2}{\hbar\omega}\frac{\mathrm{Re}\, Z_0(\omega)}{R_Q}\Big[P(2eV \mp \hbar\omega) + P(-2eV \mp \hbar\omega)\Big], \tag{4.19}$$

$$\kappa(\omega) = \frac{2}{\pi}\frac{Z_{\mathrm{ext}}}{Z_0(\omega)}. \tag{4.20}$$

Equation (4.18) can be seen as the frequency-resolved version of the energy balance equation (4.5) we had in the previous approach. We solve this system numerically, for the same parameters as for Figure 4.2, and obtain the dc current through the usual $P(E)$ formula evaluated with the steady-state populations. We plot on Figure 4.3 the IV obtained and the steady-state temperatures, defined through Bose-Einstein $k_B T_m = \hbar\omega_m/\ln(1+1/\bar{n}_m)$, for different voltage biases. Although the temperatures are not uniform in frequency, the current obtained matches rather well the simple single-temperature model. We also reproduce the bistability, which we obtain numerically by starting the numerical integration from two different initial conditions, either a cold state $n_m(t=0) = 0$ or a hot state $n_m(t=0) \gg 1$. However, this calculation relies on $\Lambda_m^2 \ll 1$ which is true only for modes with index $m \gg 2Z_c/R_Q$. Inspecting Eq. (4.2), we have $\Delta\omega_m \propto 1/N$ but also $\omega_m \propto m/N$ which might invalidate our treatment for the first few modes. To check the validity of this approach we now simulate the full classical dynamics of our system.

4.2.4 Classical chaotic dynamics

We have seen that the temperatures generated by the overheating are quite high, $T_m > \hbar\omega_m$. This justifies that the quantum fluctuations should be washed out and that a classical (possibly stochastic) approach is valid. We thus write down the classical equations of motion for the mode envelopes $\alpha_m = \langle \hat{a}_m \rangle$

$$\frac{d\alpha_m}{dt} = \left(-i\omega_m - \frac{\kappa_m}{2}\right)\alpha_m + i\Lambda_m \frac{I(t)}{2e}, \tag{4.21}$$

$$I(t) = \frac{2eE_J}{\hbar}\sin\left[\frac{2eVt}{\hbar} - \sum_m \Lambda_m(\alpha_m + \alpha_m^*)\right]. \tag{4.22}$$

We integrate these equations numerically to obtain the dc current $I = \overline{I(t)}$, the average populations $\bar{n}_m = \overline{|\alpha_m(t)|^2}$, with the overbar denoting time-averaging, and then infer the effective temperatures of our modes using the classical Rayleigh-Jeans

[4] We recall that the $\Gamma^\pm$ depend on the P function evaluated using the populations n_m of all the modes.

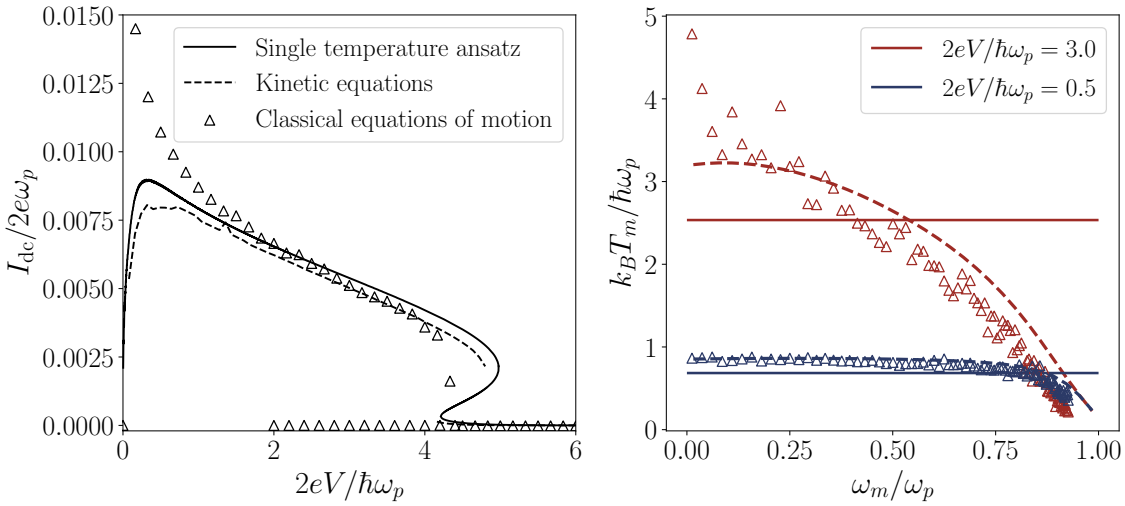

Figure 4.3: Comparison of our three approaches in the modelling of the photonic Joule effect. On the left we compare the IV curves obtained by three models, showing remarkable agreement. On the right we plot the effective temperatures T_m versus the frequencies ω_m for two bias values; the solid lines represent the single temperature obtained with the first approach. The parameters used are the same as for Figure 4.2, with the κ_m and Λ_m defined by Eqs (4.4) and (4.2), respectively. The classical simulation is done with 200 modes and for a chain of $N = 5000$ junctions.

relation $T_m = \hbar\omega\bar{n}_m$. We compare the results with the previous approaches on Figure 4.3, and, surprisingly, the classical solution matches the perturbative quantum calculations. The reason can be found in the details of the classical dynamics that is chaotic due to the non-linearity of the system. This is clearly visible in the time-trajectories of $\alpha_m(t)$ in the complex plane, that we plot in Figure 4.5 for two modes and two different bias values. Our system is ergodic and the trajectories $\alpha_m(t)$ sample a centered Gaussian distribution $p(\alpha_m) = (\hbar\omega_m/T_m)e^{-|\alpha_m|^2\hbar\omega_m/T_m}$, as shown on Figure 4.4. Thanks to chaos, the variables α_m behave as Gaussian random variables on long timescales despite the absence of any stochastic terms in the equations of motion, allowing the use of the perturbative calculations we made beforehand, if E_J is small.

Obviously, quantum fluctuations are present, but their effect is negligible when the temperature is high. However, we see on Figure 4.3, that the bistable region is larger in the classical calculations. This might be due to the importance of these vacuum fluctuations when in the cold state. It could also come from some higher-order effects not captured by perturbation theory, but we expect those to be small, so this is unlikely.

4.2.5 Link between classical chaos and the $P(E)$ approach

The relation between the classical chaotic equations of motion and the rate equations (4.15) is obtained by deriving a master equation for the classical phase-space distribution of the m-th mode $\rho_m(\alpha_m, \alpha_m^*)$. The procedure is essentially the same as that of the quantum master equation in Appendix G, except that the Lie bracket is now given by the Poisson bracket instead of the commutator. The details of the calculations are given in Appendix H. Starting from the classical equations of motion,

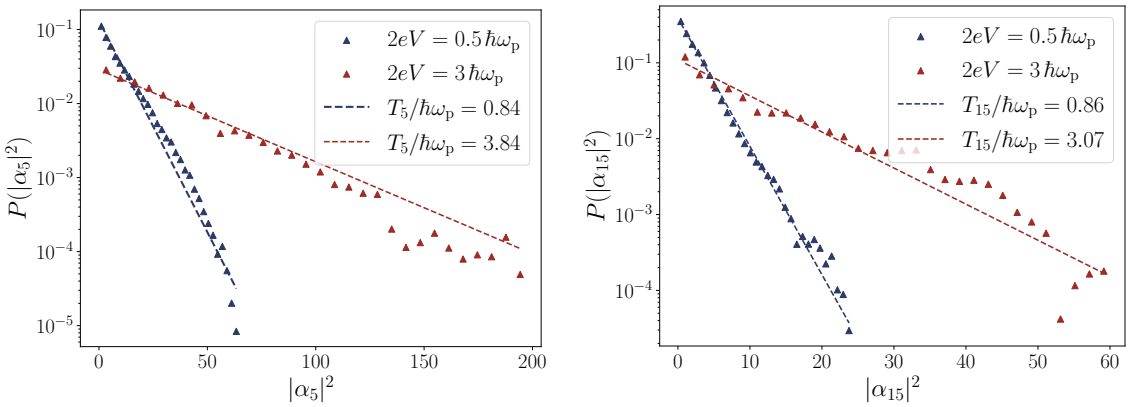

Figure 4.4: Probability distributions of $|\alpha_m|^2$ extracted by sampling the four trajectories in Fig. 4.5. An exponential distribution $p_m(|\alpha_m|^2) = (\hbar\omega_m/T_m)e^{-|\alpha_m|^2\hbar\omega_m/T_m}$ is also plotted (dotted lines) using the mode temperatures values T_m from Figure 4.3.

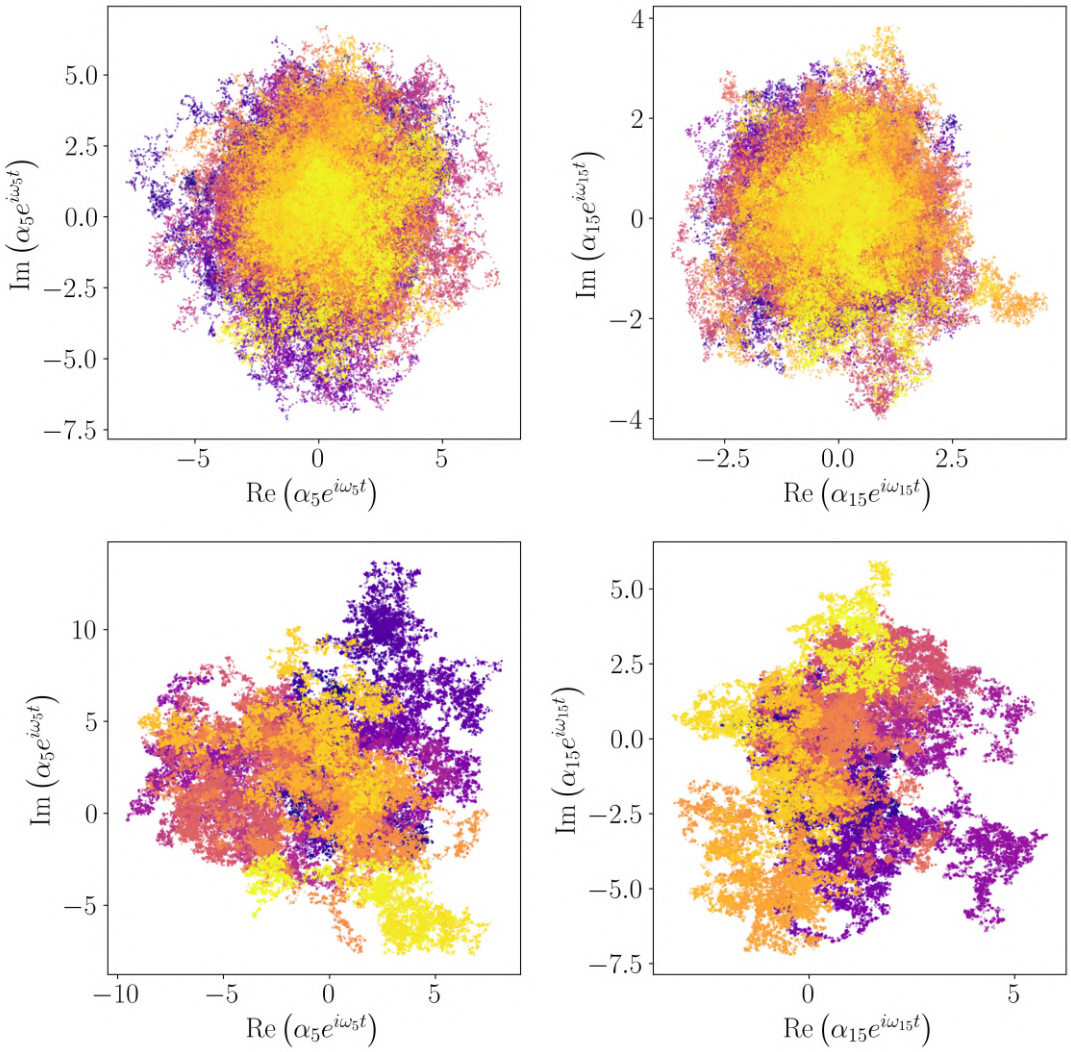

Figure 4.5: Trajectories of the slow envelopes $\alpha_m(t)\, e^{i\omega_m t}$ in the complex plane $(\mathrm{Re}\,\alpha, \mathrm{Im}\,\alpha)$ for the same system as in Figure 4.3 for two modes $m = 5$ and $m = 15$ (left and right column, respectively) at two voltages $2eV/(\hbar\omega_p) = 0.5$ and 3.0 (top and bottom row, respectively). The time is shown by color, from $\omega_p t = 0$ (purple) to $\omega_p t = 5 \times 10^5$ (yellow).

we derive a Fokker-Planck equation for ρ_m by tracing out the others modes[5]:

$$\frac{\partial \rho_m}{\partial t} = \frac{\Lambda_m^2}{4e^2} S_{II}(\omega_m) \frac{\partial^2}{\partial \alpha_m^* \partial \alpha_m} \rho_m + \frac{\kappa_m}{2} \left(\frac{\partial}{\partial \alpha_m} \alpha_m + \frac{\partial}{\partial \alpha_m^*} \alpha_m^* \right) \rho_m + \frac{\omega_m \Lambda_m^2 R_Q}{2\pi} \left[Y_J(\omega_m) \frac{\partial}{\partial \alpha_m} \alpha_m + Y_J^*(\omega_m) \frac{\partial}{\partial \alpha_m^*} \alpha_m^* \right] \rho_m. \tag{4.23}$$

The diffusion coefficient is proportional to the classical current spectral density S_{II} given by Eq. (2.74), but with a now classical correlator

$$J_{\mathrm{Cl}}(t) = \sum_k 2\Lambda_k^2 \langle |\alpha_k|^2 \rangle \left(\cos \omega_k t - 1 \right). \tag{4.24}$$

The drift coefficient contains the classical admittance of the junction Y_J, which can be computed in the same way as in Section 2.3.4 through the linear response of the Josephson current:

$$Y_J(\omega) = \left(\frac{2eE_J}{\hbar} \right)^2 \frac{1}{2\hbar\omega} \int_0^{+\infty} \left\langle \left\{ e^{i\phi(\tau)}, e^{-i\phi(0)} \right\} \right\rangle \left(e^{i\omega\tau} - 1 \right) \cos \left(\frac{2e}{\hbar} V\tau \right) d\tau, \tag{4.25}$$

with the average done on the other modes Gaussian distributions. The Poisson bracket is given by

$$\{A, B\} = \sum_m \frac{\partial A}{\partial \alpha_m} \frac{\partial B}{\partial \alpha_m^*} - \frac{\partial A}{\partial \alpha_m^*} \frac{\partial B}{\partial \alpha_m}. \tag{4.26}$$

Multiplying equation (4.23) by $|\alpha_m|^2$, and integrating over the complex plane, yields the kinetic equation for the average population $\bar{n}_m = \langle |\alpha_m|^2 \rangle$

$$\frac{\partial \bar{n}_m}{\partial t} = \frac{\Lambda_m^2}{4e^2} S_{II}(\omega_m) - \frac{\omega_m \Lambda_m^2 R_Q}{\pi} \mathrm{Re}\left[Y_J(\omega_m) \right] \bar{n}_m - \kappa_m \bar{n}_m. \tag{4.27}$$

This has to be compared with the quantum kinetic equation (4.16), that we rewrite here:

$$\frac{\partial \bar{n}_m}{\partial t} = \Gamma_m^+ - \left(\Gamma_m^- - \Gamma_m^+ \right) \bar{n}_m - \kappa_m \bar{n}_m. \tag{4.28}$$

It is not directly obvious that the classical limit of this equation is Eq. (4.27). In particular, the classical correlator $J_{\mathrm{Cl}}(t)$ is real for all times, implying $P(E) = P(-E)$. In this limit the rates equalize and $\Gamma_m^- - \Gamma_m^+$ vanishes if one directly apply Eq. (4.14) to compute them. However, the equivalence can be made by utilizing the definitions of the current noise spectral density (2.75) and the real part of the impedance (2.79) in the quantum treatment to rewrite the rates. We have

$$\Gamma_m^{\pm} = \frac{\Lambda_m^2}{4e^2} S_{II}(\pm\omega_m), \tag{4.29}$$

$$\Gamma_m^- - \Gamma_m^+ = \frac{\omega_m \Lambda_m^2 R_Q}{\pi} \mathrm{Re}\, Y_J(\omega_m), \tag{4.30}$$

which makes the correspondence between Eqs. (4.27) and (4.28) now apparent.

[5]The partial derivatives in the equation have to be understood as differential operators acting on everything to their right $\partial_\alpha \alpha \rho = (\alpha\rho)'$.

The diffusion coefficient in (4.23), arises from the symmetrized current noise spectrum density, Fourier transform of the anti-commutator $\{\hat{I}(t+\tau), \hat{I}(t)\}_+$, while the dissipative term, proportional to $\mathrm{Re}\, Y_J$, arises from a commutator which has to be replaced by a Poisson bracket[6]. In particular, comparing the classical (4.25) and quantum (2.78) definitions for Y_J, we have the limit

$$e^{J(t)} - e^{J^*(t)} \longrightarrow \left\langle \left\{ e^{i\phi(t)}, e^{-i\phi(0)} \right\} \right\rangle = -2i\, e^{J_{\mathrm{Cl}}(t)} \sum_k \Lambda_k^2 \sin \omega_k t. \tag{4.31}$$

The classical limit, on the right-hand side, corresponds to the first-order term in the expansion of the left-hand side with respect to the zero-point fluctuation (ZPF) part of the correlator $J(t)$ [see Eq. (4.9)]

$$J(t) = J_{\mathrm{Cl}}(t) + J_{\mathrm{ZPF}}(t) = J_{\mathrm{Cl}}(t) + \sum_k \Lambda_k^2 \left(e^{-i\omega_k t} - 1 \right). \tag{4.32}$$

Thus, for the bath correlations functions, which determine the fluctuation-dissipation felt by the subsystem, the classical limit is correctly recovered by taking the limit $J_{\mathrm{ZPF}} \to 0$. For the mode under consideration, the classical Fokker-Planck equation (4.23) can be recovered by using the Glauber-Sudarshan P-representation for the density matrix of the mode [5, 101]:

$$\hat{\rho}_m = \int d\alpha_m d\alpha_m^*\, P_{\mathrm{GS}}(\alpha_m, \alpha_m^*) |\alpha_m\rangle\langle\alpha_m|. \tag{4.33}$$

In our case P_{GS} can be directly identified with the phase-space distribution ρ_m in the classical limit, so that rewriting the quantum master equation of Appendix G in terms of P_{GS} yields the Fokker-Planck equation (4.23). The classical limit is then simply taken by replacing P_{GS} with ρ_m.

4.2.6 Discussion on the validity of the modeling

Overheating of the quasiparticles

Since the photonic bath heats up significantly, there is a possibility that it also overheats the quasiparticle bath in the superconducting electrodes of the junctions forming the array, potentially disrupting superconductivity in the chain. If quasiparticles scatter to energies exceeding the superconducting gap Δ, pair-breaking processes may occur. We derive in Appendix I a characteristic energy scale Ξ associated with the heating so that if $\Xi < \Delta$ and $\hbar\omega_p \ll \Delta$, quasiparticles should not overheat. The expression for Ξ is given by

$$\Xi = \left[\frac{1}{6\pi^2\sqrt{2}} (\hbar\omega_p)^2 k_B T_0 \Delta^3 \sqrt{\frac{C_{\mathrm{g}}}{C}} \frac{\tau_{\mathrm{n}}}{\hbar\nu_0} \right]^{1/6}, \tag{4.34}$$

with ν_0 the density of states of our aluminum electrodes in J^{-1}. To estimate Ξ for our case, we use the same parameters for the electromagnetic properties of the chain as in the previous section, and take $k_B T_0 = 3\hbar\omega_p$. We use the material values for aluminum displayed in table 4.1, giving us a ratio $\Xi/\Delta \sim 0.1$, telling us that the quasiparticles should not overheat in this case.

[6] The limit $\hbar \to 0$ is not straightforward to take as we have various $\hbar$ constants which are purely there for normalization (like those from the superconducting flux quantum, for example). If we really want to take the classical limit this way, we have to track the "dynamical $\hbar$" factors, introduced by the quantum time evolution, and take only these to 0.

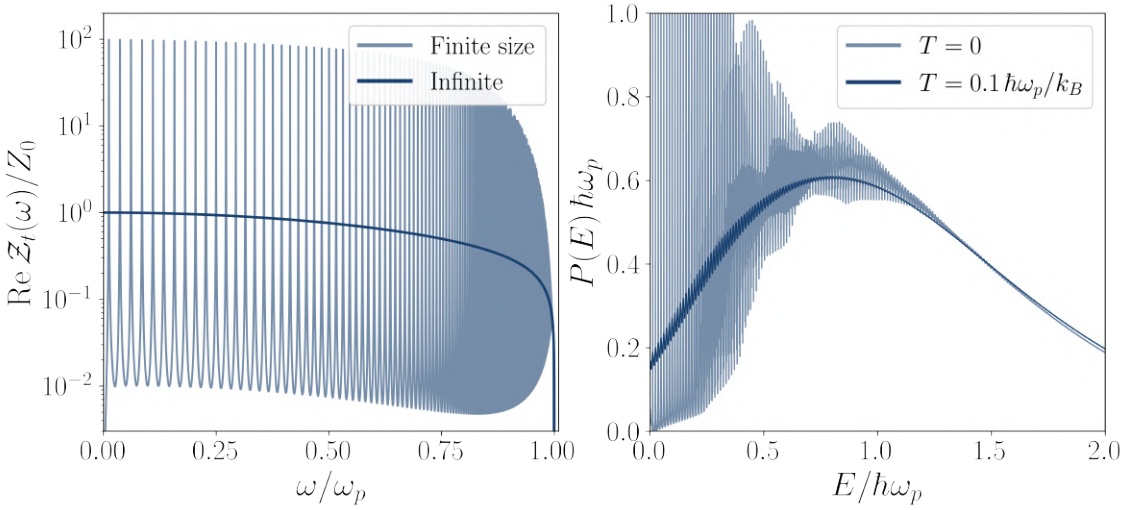

Figure 4.6: Left: comparison between the continuous impedance $Z_t(\omega)$ we use in the calculations and the finite-size version $\mathcal{Z}_t(\omega)$ defined by Eq. (4.35). Right: $P(E)$ function computed using the finite-size impedance $\mathcal{Z}_t(\omega)$ for two temperatures.

Applicability of $P(E)$ for finite size environments

The first two approaches we presented rely on applying $P(E)$ iteratively to obtain the long timescales dynamics. As discussed at the end of subsection 2.3.4, this is valid if the tunneling current is sufficiently small $E_J P(E) \ll 1$ and $E|\partial P/\partial E| \ll P(E)$. For a finite-size environment such as our array, these conditions are not necessarily satisfied at zero temperature. Indeed, the discrete impedance of the environment $\mathcal{Z}_t(\omega)$, seen by the small junction, is composed of sharp Lorentzians with linewidths $\kappa_m \ll \omega_m$,

$$2\pi \frac{\mathcal{Z}_t(\omega)}{R_Q} = \sum_m \omega_m \Lambda_m^2 \frac{2i\omega}{(\omega + i\kappa_m/2)^2 - \omega_m^2}. \tag{4.35}$$

To check the validity of our approach we compare on Figure 4.6 the function $P(E)$, computed using the discrete impedance $\mathcal{Z}_t(\omega)$, for $T = 0$ and $T = 0.1\,\hbar\omega_p/k_B \approx 100\,\mathrm{mK}$. We clearly see that the finite temperature smoothes out the fine structure, so our use of the continuum $P(E)$ is valid since the system overheats.

Moreover, even at zero temperature, $P(E)$ smoothes out at large voltages $2eV > \hbar\omega_p$ thanks to the high density of multiphoton states at these energies. This is only possible because we have dispersion in our system which makes the frequencies ω_m non-commensurate with each others, and washes out possible correlations. We can suspect that this is also what drives the chaos in the classical solutions, making

Volume V_{el}	$0.2\,\mu\mathrm{m}^3$
Fermi density of states D_F	$1.5 \times 10^{47}\,\mathrm{J}^{-1}\mathrm{m}^{-3}$
$\nu_0 = D_F V_{el}$	$3 \times 10^{28}\,\mathrm{J}^{-1}$
Superconducting gap Δ	$2\pi\hbar \times 50\,\mathrm{GHz}$
Phononic relaxation time τ_n	(10–100) ns

Table 4.1: Table of the material parameters used in the calculation of Ξ, assuming aluminum electrodes.

the dynamics incoherent (along with the non-linearity obviously). Indeed, if the frequencies were all multiple of a fundamental [102], like for $\lambda/4$ resonator $\omega_m = (2m+1)\omega_0$, the system would have a trivial recurrence time of $2\pi/\omega_0$ rendering our incoherent treatment invalid[7]. As we will see in more detail in the next chapter this incoherent hypothesis is not always satisfied in our system. Indeed, the first modes are almost commensurate with each other due to the absence of dispersion at low frequency $\partial^2\omega/\partial k^2 \xrightarrow{\omega\to 0} 0$. This can lead to the formation of a coherent state in these modes since they are also the most coupled to the non-linearity.

Range of validity of the approaches

Before moving on to the experimental study of the found overheating, we discuss when each approach is valid. We focus on comparing the kinetic equations approach with the classical calculation since the single-temperature model is essentially a simpler version of the former.

When both the perturbative quantum approach and the classical equations of motion agree, we expect the theory to be valid. Technically, there is still the possibility that the complete quantum many-body dynamics is somehow highly non-trivial, either through quantum scarring or many-body localization [103], escaping both models. This is outside the scope of this work, and, as we will see in the next section, our models describe rather well experimental data. If some richer dynamics exists, it is either outside our range of parameters or it adds a non obvious signature to the experimentally relevant observables.

At low voltages, the two calculations disagree and their validity will depend on the characteristic impedance of the environment Z_c. At low impedances $Z_c \ll R_Q$ and arbitrary E_J, we expect the classical solution to be valid, while if $Z_c \gg R_Q$, one should rather use $P(E)$, as long as the conditions we discussed above for the perturbative regime are satisfied. Close to zero bias, the Bloch band dynamics we described in Chapter 2 might impact our calculations. However, we can compute the power injected IV by the small junction using the low energy models of Chapter 2 and check if it exceeds the cooling power of our transmission line. If it does, the system will overheat, and we can expect the low energy physics of the small junction to be washed out. In this case, $P(E)$ become valid again.

However, as we will see when comparing our experimental data to theory, the two approach can disagree at large bias values. This will be caused by the appearance of a coherent state in the system invalidating the incoherent $P(E)$ approach. In this regime, we expect the classical calculation to be more reliable, and we will show that they agree with the experiment.

4.3 Experimental evidence

4.3.1 Extension of the setup

In order to measure the photonic Joule effect, we extend our measurement setup with respect to what we saw in Chapter 3, keeping the combination of dc and rf lines but

[7] We ignore losses in this argument, but since they are small ($\kappa_0 \ll \omega_0$), their presence alone should not be sufficient for chaos to emerge. This changes once the Lamb shift misaligns the frequencies enough to induce an effective dispersion.

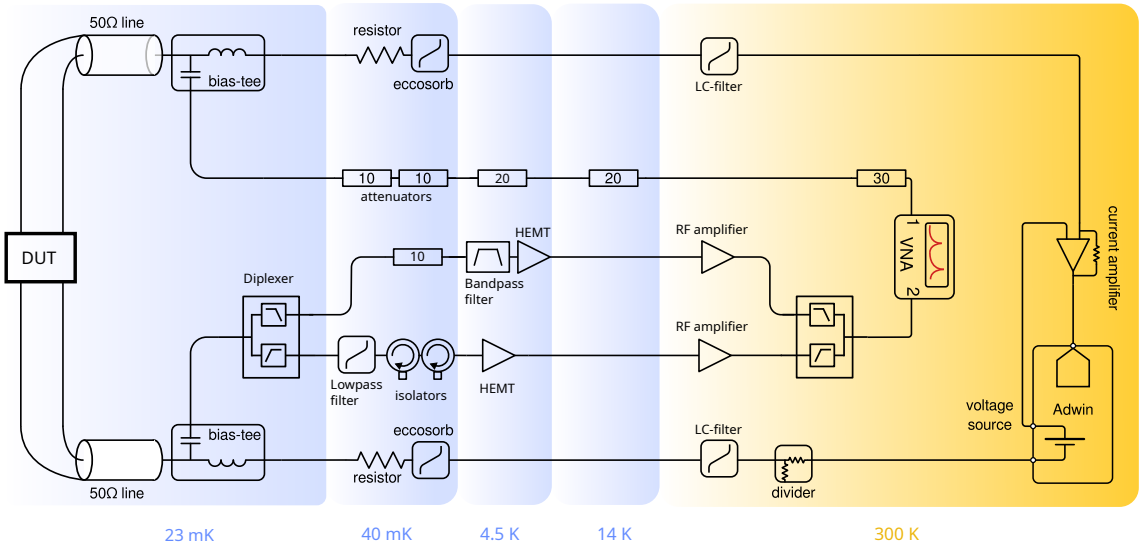

Figure 4.7: Extension of the experimental setup with the addition of an output line, allowing us to measure from 0.2 GHz to 12 GHz by splitting the microwave output in two, using a diplexer.

increasing our measurement bandwidth from 4–8 GHz to 0.2–12 GHz. As shown on Figure 4.7, this is done by splitting the output line in two using a diplexer, allowing us to amplify the 0.2–4 GHz and 4–12 GHz bands separately, before recombining them at room temp through a second diplexer. The 4–12 GHz output line has the same disposition as the one of Chapter 3 (see Figure 3.2), although with isolators and amplifiers of larger bandwidths. The 0.2–4GHz line does not contain isolators, because at these frequencies they would be too bulky to fit in our fridge, and so a simple -10 dB attenuator is used to remove the radiation emitted by the HEMT. The goal of this experiment is to measure the hot photons emitted by the sample due to the photonic Joule effect, so we have to calibrate the gain of our measurement chain. To do so, we heat up the two last stages of our cryostat by driving a current through a resistor anchored on the mixing chamber. The current is regulated using a PID controller, allowing us to control the temperature [94]. Using this, we measure the power spectral density (PSD) of the noise emitted by the setup with a spectrum analyzer, sweeping the coldest stages temperature T_{cold} from 40 mK to 500 mK. Since our first stage of amplification has at least 30 dB of gain, the measured spectrum is dominated by the thermal noise at T_{cold}, and the noise added the HEMTs. We model the added noise by an effective temperature T_{HEMT}, so that the measured PSD (in W/Hz) at the frequency f is given by

$$\text{PSD}(f) = G\left[\frac{hf}{2}\coth\left(\frac{hf}{2k_BT_{\text{cold}}}\right) + k_BT_{\text{HEMT}}\right], \tag{4.36}$$

with G the total gain of our measurement chain. Fitting this relation at each frequency to the measured PSD versus temperature allows us to extract the gain G and the noise temperature T_{HEMT} of our setup [104]. The result is given on Figure 4.8, where we clearly see a dip in the gain around 3.6 GHz. It corresponds to the transition between the two bands of the diplexer we use. The gain and noise values are consistent with the expected performances of our amplifiers. Since we heat up the entirety of the two stages, our plane of reference for this calibration

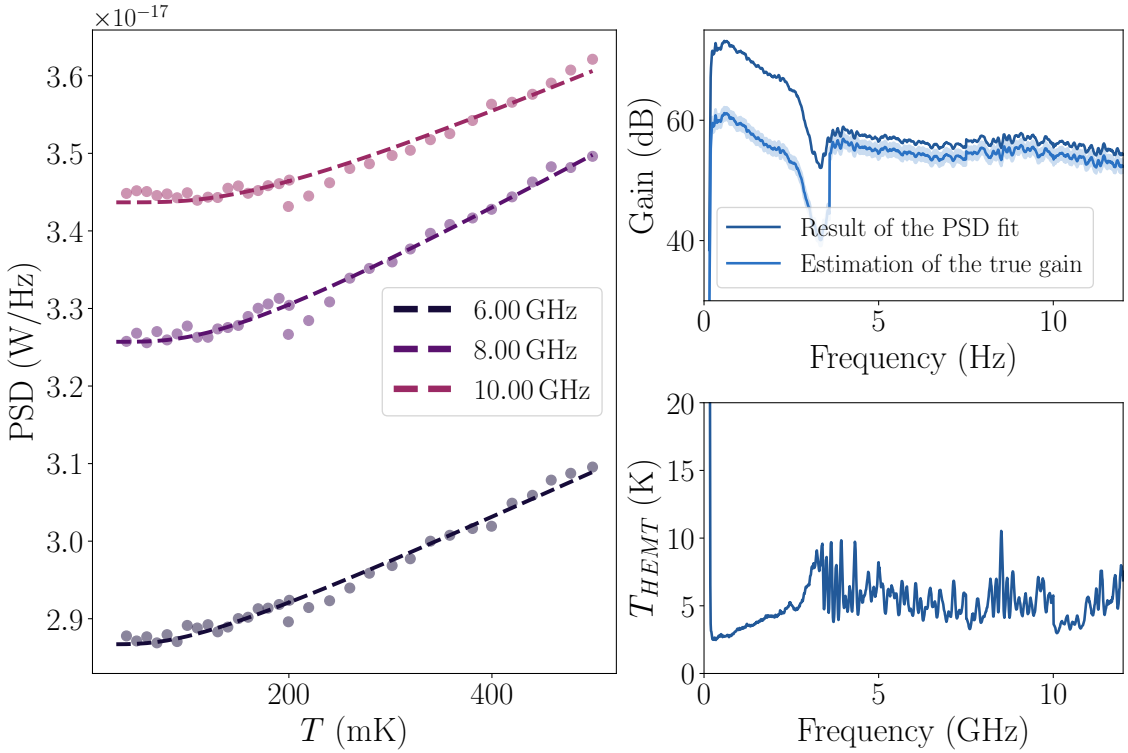

Figure 4.8: Results of the gain calibration: by sweeping the temperature of the coldest stages of our fridge we can fit Eq. (4.36) to the measured PSD at the output of our lines. The left plot shows such fit (dashed lines) against the measured PSD (dots) for three different frequencies. On the right part, we plot the gain (top right) obtained from this fit along with an estimation of the true gain since the plane of reference of this calibration is not at the sample output (see the main text for details). On the bottom right, we plot the noise temperature, obtained from the fit, of the first amplification stage of our lines. The two measurement bands of the setup (0.1–4 GHz and 4–12 GHz) are apparent from their differences in gain and noise. The absence of ripples on the 0.1–4 band, compared to the 4–12 band, stems from the presence of the -10 dB attenuator on the low frequency branch, damping any standing wave.

corresponds to the last dissipative 50 Ω-matched element on each line. These are the isolators for the 4–12 GHz band, and the −10 dB attenuator for the 0.2–4 GHz band. Because of this, we have to account for eventual losses between the sample and this plane of reference if we want access to the full gain of our measurement chain. Using the datasheets of our microwave components, we estimate these losses to be on the order of 2 dB at cold (plus the attenuator for the low-frequency line). We thus subtract this value, with an uncertainty of ±1 dB, when using our gain value.

4.3.2 Sample characterization

We use the same sample geometry as in the previous chapter: a small junction embedded in an array of 5000 larger junctions. We give on Figure 4.9 an IV curve (a) of the sample along with two broadband transmission measurements (b,c). The transmission measurements are taken at two different voltage bias points, $V_0 = 0$ and $V_0 = 0.28\,\mathrm{mV}$, indicated on panel (a) by colored dots. The IV curve shows a non-trivial current with a step-like feature which abruptly stops at 0.2 mV. A hysteretic behavior is observed close to the jump. The two transmission measurements enable us to distinguish between the odd and even modes of our system by analyzing their voltage dependencies. The odd modes, which are strongly coupled to the small junction, shift positions between zero bias (b) and large bias (c). At zero bias, they are inductively coupled, whereas at large bias, they become capacitively coupled. The even modes do not shift with voltage since they are effectively decoupled from the small junction in the center, allowing us to easily distinguish between odd and even (see also Figure 4.10). In order to extract the parameters of our system we adopt the same procedure as in the previous chapter: we fit the position of the even modes to the dispersion relation of a Josephson array with half the number of junctions. The different parameters of the sample are summarized in Table 4.2.

4.3.3 Emission measurements

To experimentally investigate the photonic Joule effect, we measure the radiation emitted by our sample as a function of the voltage bias. For each mode, this is

Parameter	SQUID	Array
Area	$0.14\,\mu\mathrm{m}^2$	$1.2\,\mu\mathrm{m}^2$
Critical current I_C	30 nA	270 nA
Junction capacitance C_J	6 fF	55 fF
Inductance L_J	11 nH	1.2 nH
Plasma frequency ω_p	20 GHz	20 GHz
E_J/E_C	4.9	170
Number of junctions N_{JJ}	–	5000
Characteristic impedance Z_c	–	6.1 kΩ
Ground capacitance C_g	–	33 aF

Table 4.2: Table recapitulating the parameters of the main sample studied in this chapter. As in Chapter 3, the values for the SQUID column take into account the two small junctions.

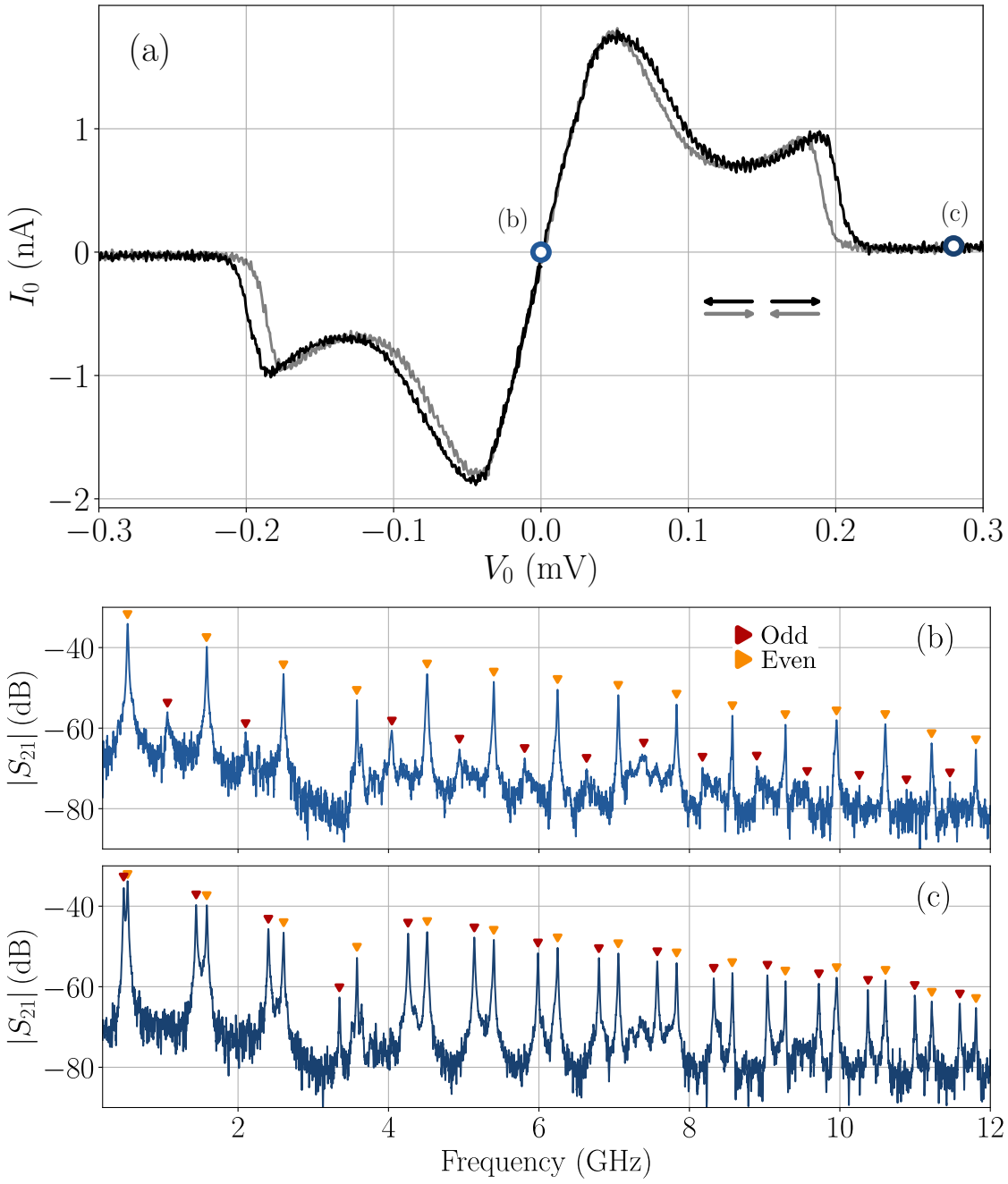

Figure 4.9: *IV* curve (a) and transmission coefficient S_{21} measurements for two different voltage bias (b,c), whose values are indicated by colored dots on (a). The arrows on plot (a) indicate the direction of the voltage sweep, either going towards higher (black) or lower (gray) voltages, to help highlight hysteretic features. The small triangles indicate if a mode is even or odd through their coloring.

achieved using a spectrum analyzer (R&S FSV3030) in zero-span, centered at the mode frequency. The resolution bandwidth (RBW) of the analyzer is set to 40 MHz, which is larger than any of the mode linewidths $\kappa \sim 20\,\mathrm{MHz}$. In place of the ADwin we use an arbitrary function generator (AFG Tektronix-AFG3252) to apply voltage ramps of amplitude 0.3 mV and frequency 1 kHz to the sample. The use of an AFG allows us to trigger the zero-span measurement of the spectrum analyzer and average efficiently the power versus voltage. The ramp amplitude and frequency are chosen in order to optimize measurement time while confining the distortions, arising from the low-pass cutoff of the setup, to the endpoints of the ramp. As shown on Figure 4.10, the odd modes frequencies move with the applied voltage, jumping from their inductive positions, close to zero-bias, to the capacitive ones when we increase the voltage. Thus, in order to collect all the emitted power by the sample, we measure at both positions and add them up for each odd mode. However, it turns out that most of the power ($> 99\%$) is emitted at the capacitive positions, even close to zero-bias. Although the odd mode frequencies do not shift after $V = 0.09\,\mathrm{mV}$, the losses of these modes greatly vary with the bias after this point, as can be read from their linewidth. This will be addressed in more detail in the next chapter, but this increase in losses is caused by the formation of a coherent state in the lowest modes of the system, enabling efficient decay processes from the other modes towards this coherent collective. After $V = 0.22\,\mathrm{mV}$, no more dc current flows in the system (see Figure 4.9), the dynamics dies, and the odd modes recovers linewidth equals to the even modes. This portion devoid of non-linear dynamics allows us to remove the background in the emission measurements as there is no radiation emitted by inelastic tunneling (since the current is zero). As such, we subtract the power measured at large bias when measuring the emission versus voltage to accurately recover the power emitted by the sample.

We show on Figure 4.11 the results of this measurement for all the fifteen odd modes capacitive frequencies present in our working frequency range. All modes exhibit a strong dependence of their emission on the applied bias. However, the first four modes behave differently from the others: their emission increases monotonically until reaching a discontinuity at $V_0 \approx 0.2\,\mathrm{mV}$. In contrast, the other modes peak at $V_0 \approx 0.09\,\mathrm{mV}$ before gradually decreasing to zero emission. The first modes, along with the one at 4.28 GHz, display hysteresis near the discontinuity. Additionally, the lowest mode of the system, at 0.48 GHz, is twenty times brighter than the others, peaking at roughly 60 fW for $V_0 = 0.2\,\mathrm{mV}$. Indeed, as mentioned above, our system undergoes a transition at the bias point $V_0 \approx 0.09\,\mathrm{mV}$, where the states of the first modes jump from thermal to coherent, depleting the populations of the other modes. This condensation-like transition will be more thoroughly studied in the next chapter, and we focus for now on comparing these measurements to our previously established theory.

4.3.4 Comparison with theory

Having made these measurements, let us confront them to the theory we developed at the beginning of this chapter. Given the large number of parameters, and the numerical complexity of the models, we do not directly fit them to the data. Therefore, we directly input the estimated parameters given in Table 4.2 into our models. In the experiment, the junction is in the center of the chain and not on its edge,

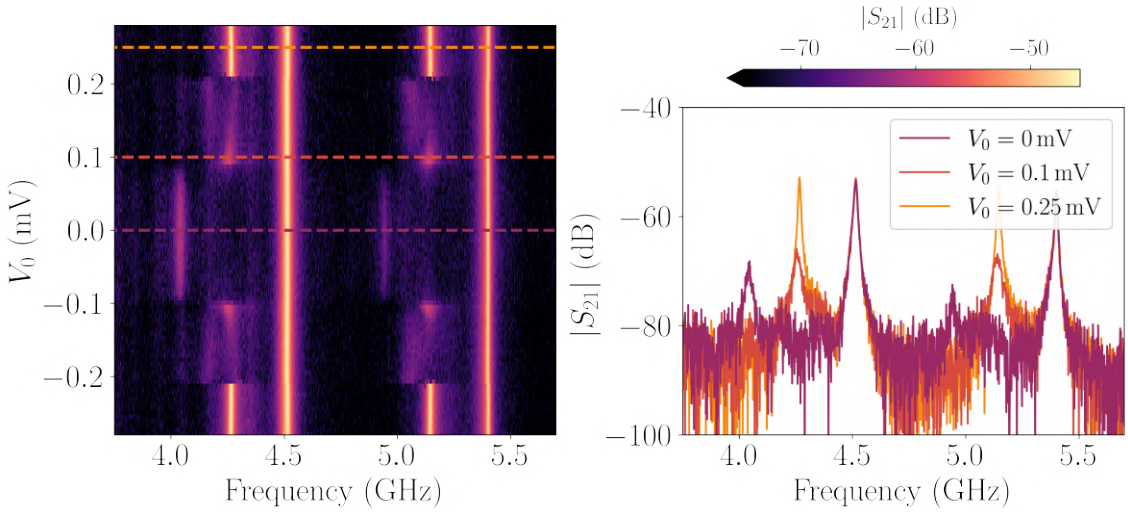

Figure 4.10: Voltage dependence of the mode frequencies. Evolution of the transmission coefficient versus voltage bias (left) showing that, while the even modes are unaffected by voltage, the odd modes frequencies strongly vary with voltage between two positions. A cut at three fixed voltages is shown on the right panel.

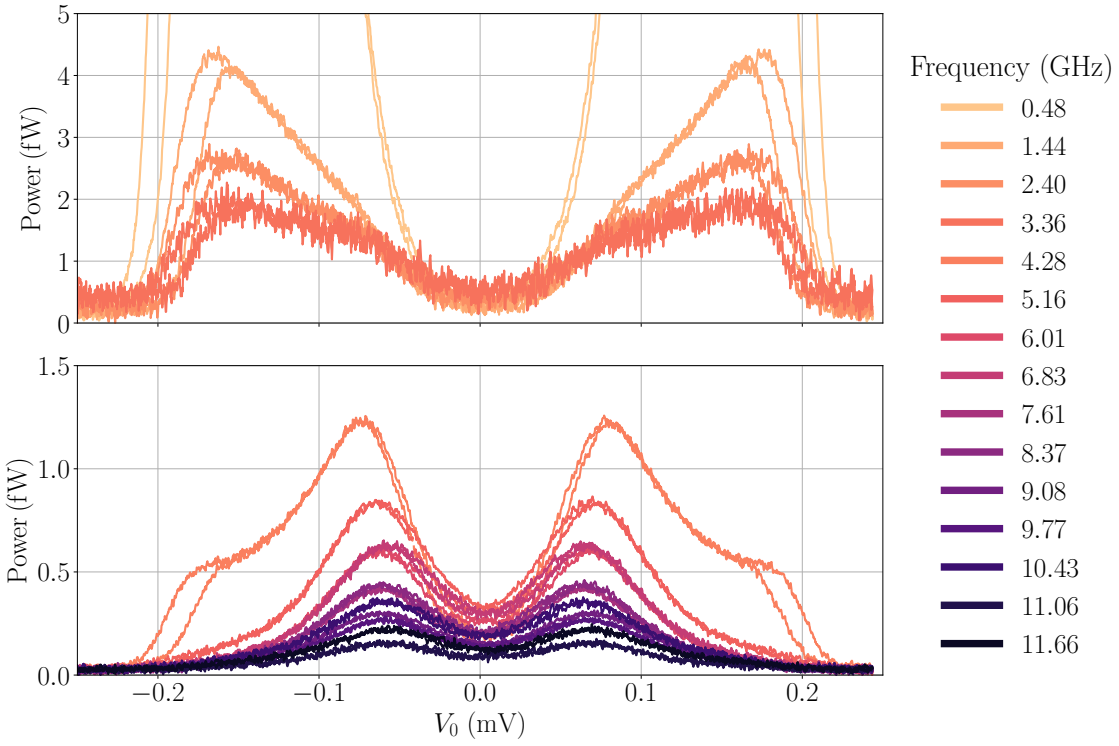

Figure 4.11: Power emitted at the sample versus voltage bias for every odd mode frequency. In order to highlight hysteresis, we superimpose the curve obtained by sweeping the bias from negative to positive with the one of reverse sweeping direction. The figure is split in two subplots to avoid dwarfing the higher frequencies in comparison with the lowest ones. The maximum emission of the first mode, at 0.48 GHz, is out of the bounds of the plot. It is one order of magnitude higher than the rest of the modes, with a maximum of 60 fW reached at $V_0 \sim 0.2$ mV.

so we have to account for that. We have already mentioned that it is coupled to only half the of the modes of the system, but it also feels twice the characteristic impedance Z_c of the chain. Thus, we input twice the impedance and half the number of junctions in our models. We also incorporate the experimental linewidths of our modes $\kappa \sim 20\,\text{MHz}$, which are larger than the theoretical value computed with Eq. (4.4). The calculations, the classical one in particular, are most sensitive to the parameters of the small junction. Unfortunately these are also the hardest parameters to extract experimentally. Given the complexity of the models, we cannot numerically fit them reliably. We therefore suppose that the plasma frequency of the small junction is the same as the ones in the chain, giving us E_J, and then adjust its capacitance C_J to best fit the models to the data. We find a capacitance of 4 fF to be the best fit, which is lower than what we expect from our fabrication process (6 fF). This discrepancy is acceptable considering our imperfect knowledge of the rest of the parameters, that we do not adjust.

Our IV curve exhibits a linear regime at low bias (see Figure 4.9a), with a slope of approximately $30\,\mu\text{S}$, which is not reproduced by any of our calculations. We suspect this linear behavior originates from experimental noise in the applied voltage bias, which is not included in the model (4.1). To estimate this noise, we analyze the emission measurement shown in Figure 4.11. As the current-voltage relation is purely linear at low bias, the emitted power follows a quadratic dependence on the bias, $P \propto I_0 V_0 \approx a V_0^2$, meaning it should vanish at zero bias. However, we observe it does not, and an offset remain due to noise. Indeed, if the bias fluctuates as $V_0 + \delta V$, we obtain

$$P(V_0 = 0) = a\langle \delta V^2 \rangle. \tag{4.37}$$

By fitting the power parabolas, we extract the coefficient a, allowing us to estimate the noise amplitude. Applying this procedure to all modes, we find characteristic noise amplitudes of approximately $50\,\mu V$. This represents a significant amount of noise that must be incorporated into at least one of our calculation.

For simplicity, and because it is expected to be more accurate at low bias, we modify the $P(E)$-based approach by adding a classical component to the correlator, $J(t) \to J(t) + J^{\text{noise}}(t)$. Since $V \to V + \delta V(t)$, this additional correlator is related to the spectral density of the noise $S_{VV}^{\text{noise}}(\omega)$ through

$$J^{\text{noise}}(t) = \frac{4e^2}{\hbar^2} \int_0^{+\infty} \frac{d\omega}{\omega^2} S_{VV}^{\text{noise}}(\omega)(\cos \omega t - 1). \tag{4.38}$$

The exact form of $S_{VV}^{\text{noise}}(\omega)$ remains unknown, as we only have access to its integral over frequency via $\langle \delta V^2 \rangle$. We assume

$$S_{VV}^{\text{noise}}(\omega) = \frac{\langle \delta V^2 \rangle}{\pi \omega_C} \frac{1}{1 + (\omega/\omega_C)^2}, \tag{4.39}$$

where ω_C represents the characteristic bandwidth of the bias noise, estimated to be 10 MHz.

The comparison experimental data and theory is shown in Figure 4.12. We also plot the temperatures $k_B T_m = \hbar\omega_m / \ln(1 + 1/\bar{n}_m)$ of each mode (b,c), that we can obtain experimentally through the power radiated by each mode with $\bar{n}_m = P_m / 2\kappa_m \hbar \omega_m$[8]. Overall, the theories describe well the dc current obtained. In par-

[8]The factor 2 comes from the fact that the photons escape the sample from both ends, effectively doubling the losses.

ticular, the position of the discontinuity at $2eV \approx 5\,\hbar\omega_p$ is in agreement with both calculations. Whereas for the temperature distribution it depends on the bias value: at low bias the data seem to agree better with $P(E)$, while at large voltages the coherent state emerges, and the classical solution becomes a better fit. We also compare the temperature as a function of voltage bias for two modes in (d) and (e). At this microscopic level, discrepancies with the theory become more apparent, though the overall qualitative agreement remains. The classical solution performs poorly for higher-frequency modes, as these modes remain relatively cold, whereas the $P(E)$-based solution provides a better approximation as long as the voltage stays below the condensation point at $2eV \approx 2.5\,\hbar\omega_p$.

It is important to emphasize that the classical calculation relies on the microscopic details of the system. While it accurately predicts macroscopic quantities like the current I, achieving a precise match for the emission without fine-tuning is unlikely. Incorporating noise into the classical calculation could enhance its accuracy, potentially improving the agreement with both emission data and low-bias currents.

We also show on Figure 4.13 the comparison with the IV of two other samples with different parameters, which are displayed in the table below. There is a higher discrepancy between the $P(E)$-based theory for Sample (III), which predicts the discontinuity in current at higher voltage. This can be explained by the fact that (III) has a much higher plasma frequency than the cutoff frequency $Z_c C_J \omega_p \approx 7$. The average mode spacing of (III) being $\sim 3\,\mathrm{GHz}$, this means the small junction is coupled to only a few modes, possibly invalidating the thermodynamic limit we take for the $P(E)$ theory.

4.3.5 Evidence for out-of-equilibrium quasiparticles

Sample (III) has a high plasma frequency, comparable to the superconducting gap, $\hbar\omega_p \sim \Delta$. As a result, the condition used in Subsection 4.2.6 and the calculations in Appendix I are no longer valid.

Indeed, in this sample we observe signs of quasiparticle overheating. Plotting the variation of the current as a function of external flux in Figure 4.14 reveals current features that are 4π-periodic with respect to the superconducting quantum of flux, suggesting that this current is carried by charges e. Interestingly, the current is maximal not at zero flux, but at $h/2e$, which corresponds to "half-flux" for e-charges. This periodicity survives until $\pm 10\pi$ of flux quantum, after which the field starts to affect the junction chain. A quantitative description of these currents is outside the scope of this work, but their presence indicate that the photonic overheating can affect the quasiparticle bath if ω_p is too large.

4.4 Conclusion

In this chapter, we explored the photonic Joule effect, where power injected by a small Josephson junction exceeds the cooling rate of the transmission line, leading to photon overheating. Unlike conventional Joule heating, this effect concerns photons rather than phonons or electrons.

We developed three theoretical approaches to describe this phenomenon, analyzing the photonic bath behavior and IV characteristics. Experimental measurements confirmed strong mode-dependent emission variations, validating the hypothesis of

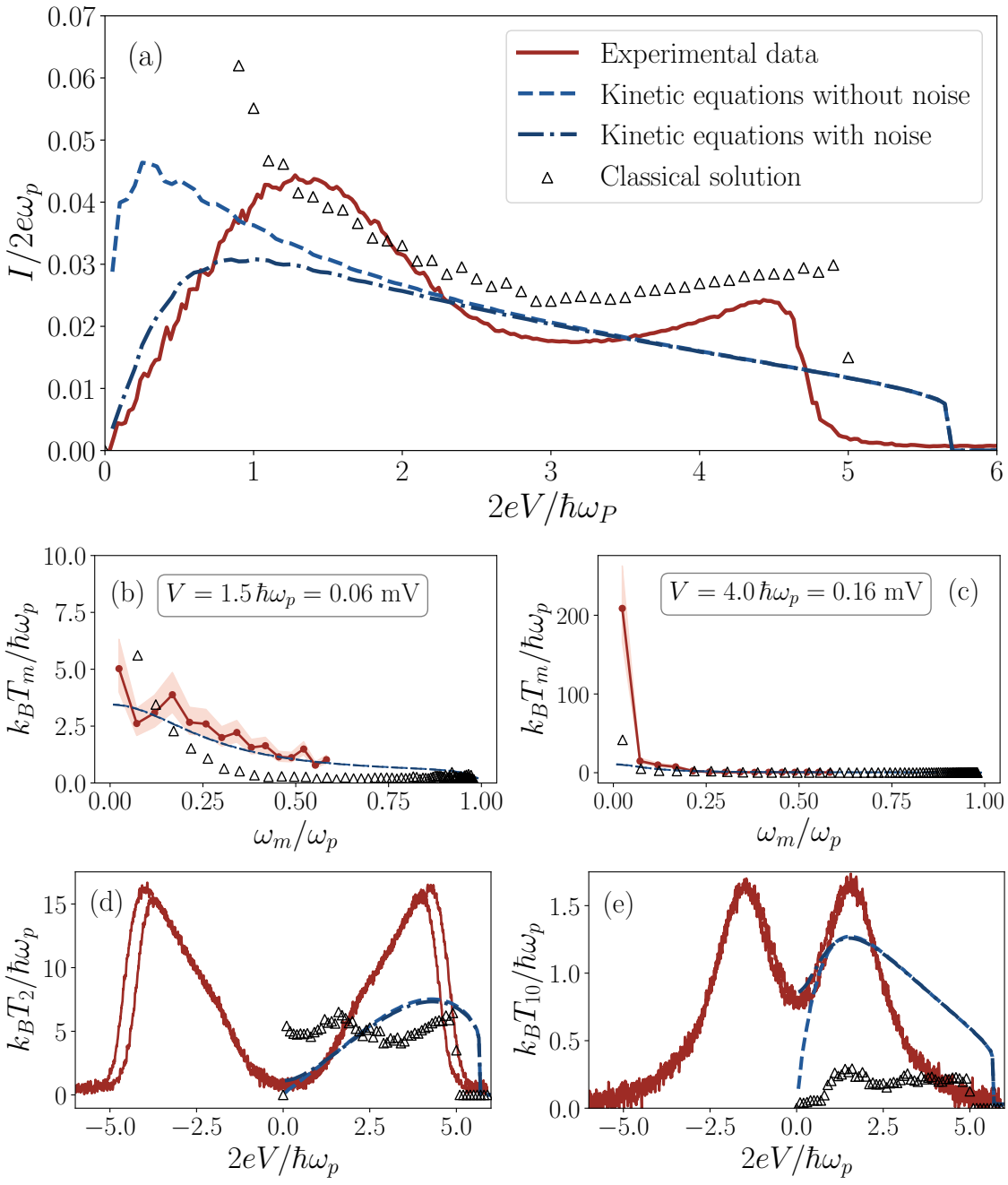

Figure 4.12: Comparison between the theory and experimental data. In (a) we compare the IV curves. In (b) and (c) the temperature distribution of the odd modes for two different bias values. In (c) the coherent state of the first mode dwarfs the other. In (d) and (e) we plot the temperature variation versus voltage bias for the second and tenth odd mode at 1.435 GHz and 8.364 GHz, respectively.

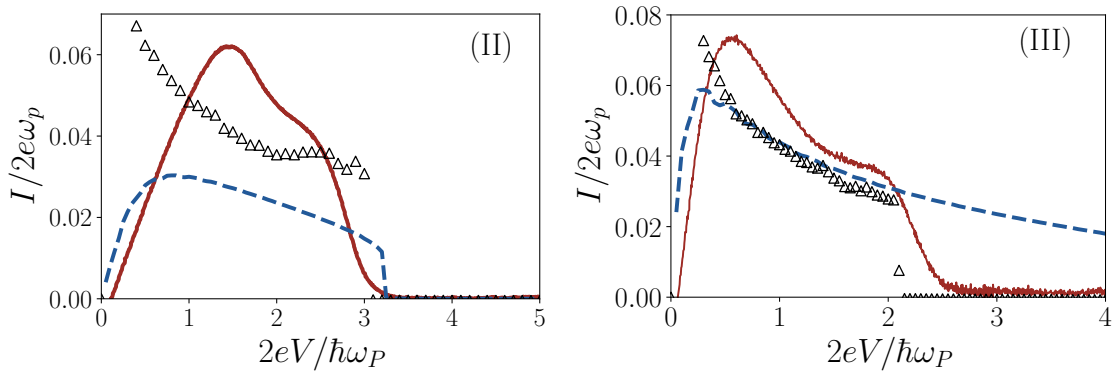

Sample	II		III	
Parameter	SQUID	Array	SQUID	Array
Area	0.08 μm^2	11 μm^2	0.08 μm^2	2.1 μm^2
Critical current I_C	20 nA	2.7 μA	120 nA	3.1 μA
Junction capacitance C_J	4 fF	500 fF	4 fF	100 fF
Inductance L_J	17 nH	0.12 nH	2.8 nH	0.1 nH
Plasma frequency ω_p	20 GHz	20 GHz	40 GHz	40 GHz
E_J/E_C	1.8	35000	10.8	7400
Number of junctions N_{JJ}	–	4000	–	5000
Characteristic impedance Z_c	–	1 kΩ	–	2.6 kΩ
Ground capacitance C_g	–	120 aF	–	16 aF

Figure 4.13: Comparison between theory and experiment for two other samples (II) and (III), using the same legend for the IV as for Figure 4.12. Their parameters are given in the table below the plots.

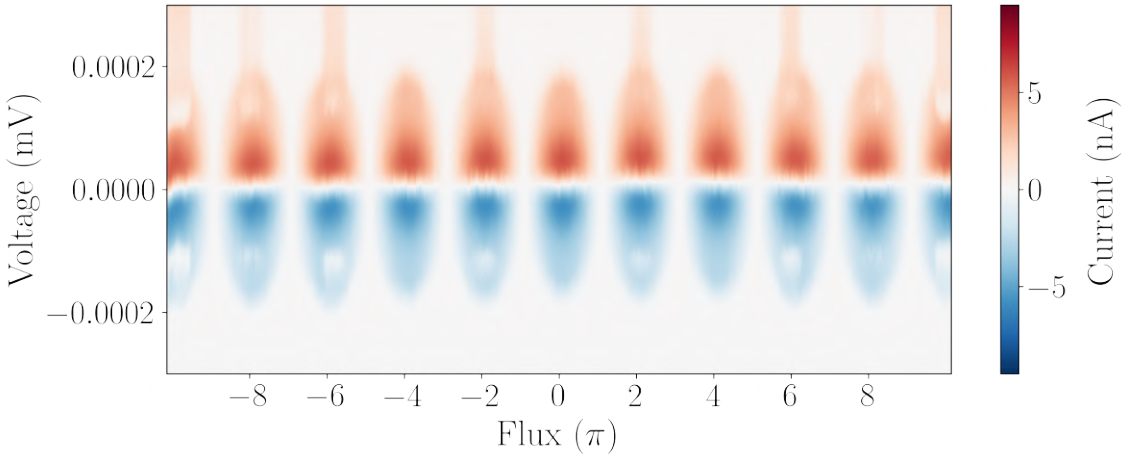

Figure 4.14: IV curve versus flux of sample (III) whose parameters are given in the table of Figure 4.13. The voltage is swept from negative to positive. A 4π periodicity is visible, indicating the presence of e-charges.

overheating. Comparisons between theory and experiment revealed good agreement in the IV curve but also some discrepancies, particularly at low bias, which we attributed to voltage noise. Incorporating a noise model improved our theoretical predictions, which we then confronted to our emission measurements, there again giving good agreement.

The picture is complicated by the appearance of a transition where the energy condenses in the lowest modes generating a coherent state. Although the classical simulation captures this transition, this model is rather complicated and depends on all the microscopic details of the chain modes. In the next chapter we will experimentally study the coherent state in more detail and try to develop some qualitative understanding on why this transition occurs.

Chapter 5

Josephson laser in a many-body setting

In the previous chapter we showed, theoretically and experimentally, that the dynamics of a voltage-biased small junction embedded in a high-impedance transmission line could overheat the modes of the system, storing a significant amount of energy in the transmission line, implemented as an array of Josephson junctions. However, when studying the phenomenon experimentally, we saw that this overheating does not occur for all bias values, as we expected. Instead, beyond a certain voltage, the system transitions from a thermal state, where energy is evenly distributed among the modes, to a state where the first mode dominates the stored energy.

As we will show in this chapter, this first mode is in a coherent state, making the transition resemble a condensation or lasing transition. There is no certainty that this transition survives in the thermodynamic limit, obtained by taking the line's length to infinity, so this not proven to be a phase transition *stricto sensu*. Nevertheless, given its similarities with conventional condensation transitions, we will, with some abuse of terminology, occasionally reuse the language of phase transition theory throughout this chapter and refer to the coherent state both as a "laser"[1] or a "condensate". We first briefly showcase some features of this coherent state using the classical approach we developed in the previous chapter, before moving to its experimental study where we observe and characterize the coherent radiation emitted by the system, allowing us to draw its phase diagram.

5.1 Brief theoretical study

The generation of coherent states in a multi-mode cavity by a voltage-biased junction has been observed experimentally before [80, 105, 106], prompting theoretical studies of the matter [102, 107, 108]. However, these studies do not apply to our system as they rely on the smallness of environmental fluctuations and, consequently on the resonant condition for the voltage $2eV = n\hbar\omega_0$, with n an integer. In our case, these fluctuations are non-negligible due to the high impedance ($Z_c > R_Q$) and high mode temperatures caused by the photonic Joule effect. Thus, previous works are not strictly applicable to our regime.

Although we do not have access to a toy model describing the transition, we saw that, when describing experimental data, solving the classical equations of motion captured the transition fairly well (see Figure 4.12). Therefore, we shall use it to get some quick insights onto the coherent part of the transition. We remind that the classical equations of motion of the system are

$$\frac{d\alpha_m}{dt} = \left(-i\omega_m - \frac{\kappa_m}{2}\right)\alpha_m + i\Lambda_m \frac{I(t)}{2e}, \tag{5.1}$$

$$I(t) = \frac{2eE_J}{\hbar} \sin\left[\frac{2eVt}{\hbar} - \sum_m \Lambda_m(\alpha_m + \alpha_m^*)\right]. \tag{5.2}$$

On Figure 5.1a, we plot again the theoretical IV obtained by numerically integrating the equations of motion above. In panel (b) we show the average population $|\alpha_0|^2$ of the first mode along with its standard deviation $\sigma_0 = \sqrt{\langle|\alpha_0|^4\rangle - \langle|\alpha_0|^2\rangle^2}$.

[1] This is perhaps also an abuse of terminology, as the device operates in the microwave regime and would more appropriately be termed a maser. However, following the convention established in previous works, we keep the laser denomination.

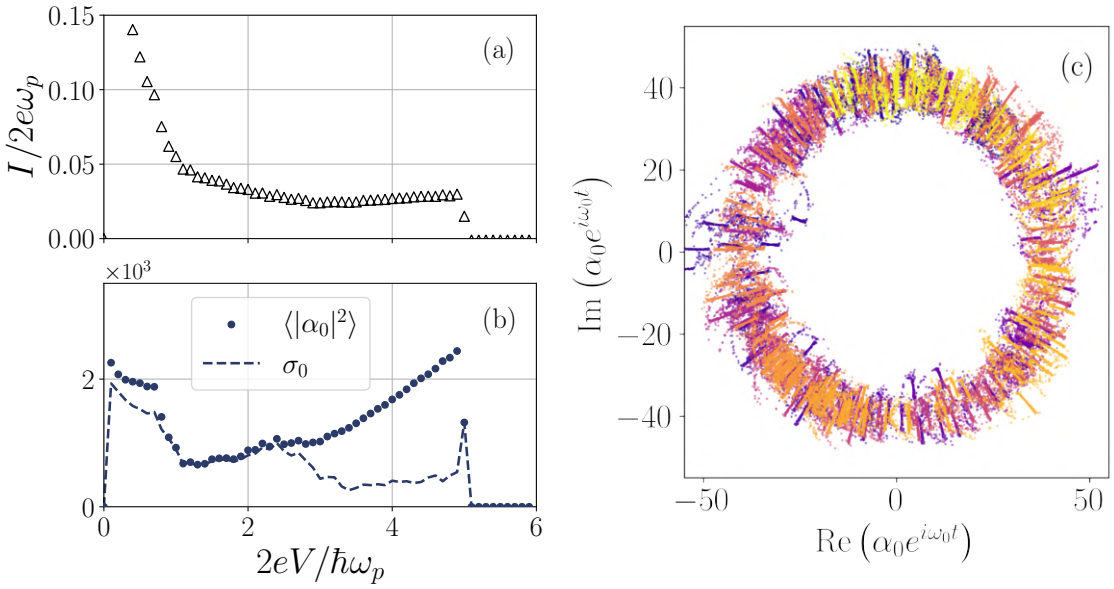

Figure 5.1: The transition in the classical simulation. On (a) we plot the IV curve obtained by integrating the numerical equations of motion Eq. (5.1) with the same parameters as last chapter given in Table 4.2. The average population (dots) of the first mode $\langle|\alpha_0|^2\rangle$ is plotted on (b) along with its standard deviation $\sigma_0 = \sqrt{\langle|\alpha_0|^4\rangle - \langle|\alpha_0|^2\rangle^2}$ (dashed line). The coherent state forms at $2eV \sim 2.8\,\hbar\omega_p$ when the average population exceeds σ_0 signaling that the probability density is no longer centered in phase space. This is confirmed by (c) where we plot the phase space evolution of the slow envelope $\alpha_0(t)e^{i\omega_0 t}$ at the bias point $2eV = 4\,\hbar\omega_p$.

The probability density is no longer centered in phase space once the average exceeds σ_0, which occurs around $2eV \approx 2.8\,\hbar\omega_p$, highlighting the transition to a coherent state. To confirm this, we also plot in (c) the trajectory of the first mode in phase space when $2eV = 4\,\hbar\omega_p$, clearly showing that the first mode is coherent. As shown on panel (b), the classical solution also yields a coherent solution at biases below $\hbar\omega_p$, but this cannot be trusted since the classical approach does not properly account for fluctuations at these low biases, and thus is not valid. For intermediates biases $\hbar\omega_p < 2eV < 2.8\,\hbar\omega_p$, we have $\langle|\alpha_0|^2\rangle = \sigma_0$, indicating that the thermal regime where the photonic Joule effect, described in the previous chapter, takes place. We also see that, in the coherent phase, the amplitude of the first mode scales directly with the bias voltage. The reason for this scaling can be found in the time dependence of the phase across the impedance formed by the transmission line,

$$\phi(t) = \sum_m \Lambda_m \left(\alpha_m + \alpha_m^*\right). \tag{5.3}$$

Figure 5.2 shows the time evolution of $\phi(t)$ for two different bias values. In the coherent state, $\phi(t)$ follows a triangular waveform whose frequency matching that of the first mode ω_0. A triangular signal $V(t)$ of amplitude A and fundamental frequency ω_0 has its Fourier series given by

$$V(t) = \frac{8A}{\pi^2} \sum_k \frac{(-1)^k}{(2k+1)^2} \sin\left[(2k+1)\,\omega_0 t\right], \tag{5.4}$$

indicating that our laser is not monochromatic since it contains all these higher

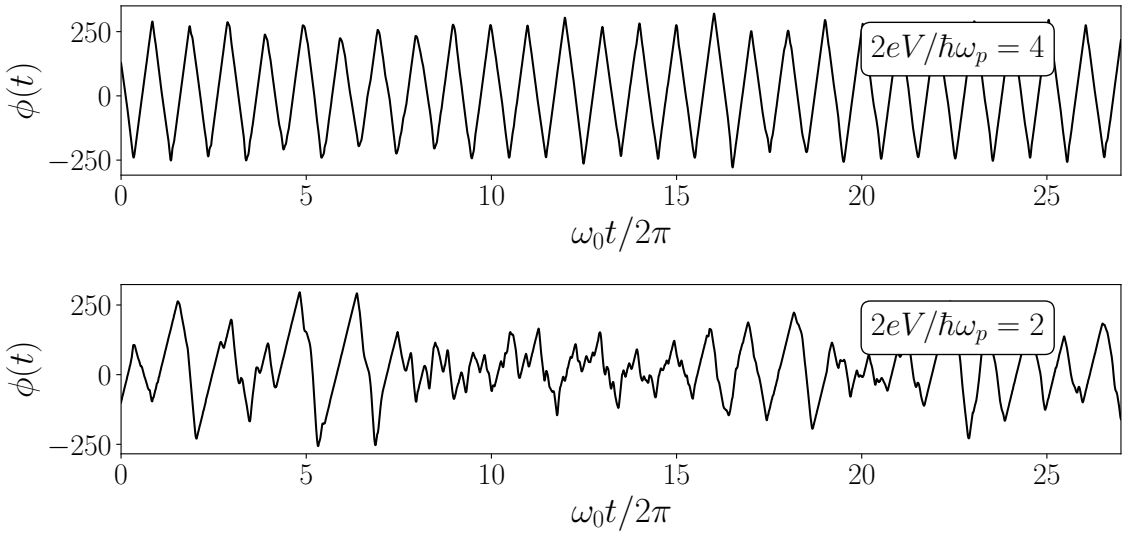

Figure 5.2: Evolution of the phase ϕ given by Eq. (5.3) for two bias values. In the coherent phase at $2eV = 4\,\hbar\omega_p$ the phase undergoes triangular oscillations with a frequency equal to that of the first mode. In the thermal state at $2eV = 2\,\hbar\omega_p$, the system fluctuates chaotically between ordered and disordered phase.

harmonics. Additionally, the slope of the linear segments approximately matches the applied voltage, $\dot{\phi} \approx 2eV/\hbar$. This is confirmed on the top panel of Figure 5.3 where we plot the time evolution of the voltage drop across the junction $\hbar\dot{\phi}/2eV$. From this observation, we estimate that the amplitude of the first mode scales linearly with the bias, $\omega_0\Lambda_0|\alpha_0| \approx 2eV/\hbar$, while higher harmonics are suppressed as $|\alpha_m| = \Lambda_0|\alpha_0|/\Lambda_m(2m+1)^2 \approx |\alpha_0|/(2m+1)^{3/2}$ (using the expression (4.2) for Λ_m). This coherent structure is then imprinted onto the current $I \propto \sin(2eVt/\hbar - \phi)$: on the downward slope of the triangular signal $\phi(t)$, the sine oscillates at a high frequency $4eV/\hbar$ and averages to 0 in the equations of motion (5.1), whereas on the upward slope $\dot{\phi}$ cancels out $2eV/\hbar$, making the mode populations undergo periodic random jumps as displayed on Figure 5.3.

An in-depth theoretical analysis of this transition lies beyond the scope of this work, and will be the topic of future efforts. We therefore now shift our focus to the experimental investigation of this transition.

5.2 Experimental observations

5.2.1 Coherent emission measurements

We use the same setup and study the same sample as in the previous chapter; its parameters are given in Table 4.2. However, the measurements in this chapter were performed during a different cooldown of the sample. In particular, the low-frequency noise was reduced by improving the grounding of the measurement setup, which made the current drop in the IV sharper. This can be seen by comparing the IVs of Figure 5.6 with those of the past chapter in Figure 4.9[2]. We plot on Figure 5.4

[2]Unfortunately the procedure to calibrate the noise using the zero-bias emission done in the past chapter (see Eq. (4.37)) could not be done here as I did not remeasure the thermal emission.

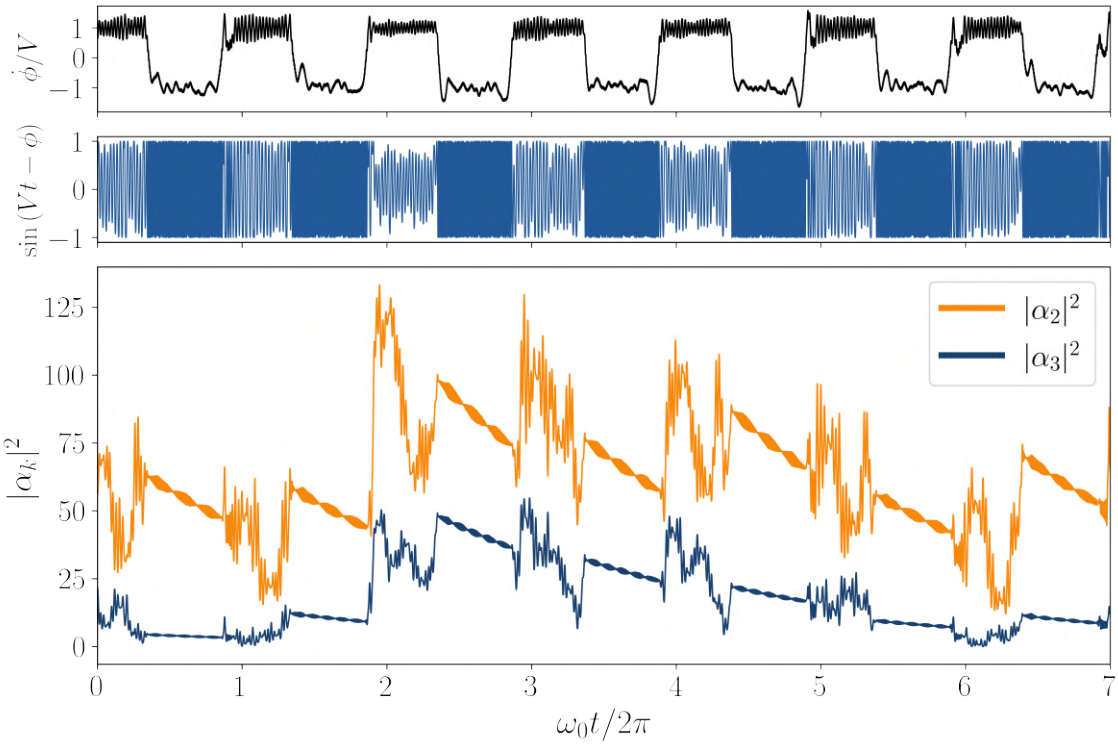

Figure 5.3: Evolution of the populations of the 2nd and 3rd mode in the coherent regime at $2eV = 4\hbar\omega_p$. The voltage drop across the junction $\hbar\dot{\phi}/2eV$ and the normalized current $\sin[2eVt/\hbar - \phi(t)]$ are plotted on top (we drop some normalization in the axis labelling for the sake of clarity), highlighting that the modes dynamics are periodically driven at the frequency ω_0. When $\dot{\phi} = -2eV/\hbar$, the sine oscillates rapidly at twice the Josephson frequency, averaging to 0 whereas when $\dot{\phi} = +2eV/\hbar$ the modes are strongly driven by the Josephson current.

the emission spectrum (a) of the laser for a bias of $V = 0.17\,\mathrm{mV}$, along with a quadrature measurement (b) done using the IQ mode of the spectrum analyzer (R&S FSV3030) with a resolution bandwidth of 3 MHz. The IQ measurement confirms that the emission is indeed coherent and undergoes phase diffusion. The diffusion timescale τ_θ can be estimated from the linewidth γ of the emission in (a). Indeed, the emitted radiation around the frequency ω_0 is determined by the time-dependence of $\alpha_0(t) = A_0 e^{-i(\omega_0 t+\theta_0)}$. Neglecting the amplitude fluctuations, the measured spectral density $S(\omega)$ is proportional to the Fourier transform of the correlator $\langle \alpha_0^*(t+\tau)\alpha_0(t)\rangle$ (we neglect the noise added by the amplifiers since the emission is bright)

$$S(\omega-\omega_0) \propto \int \langle e^{i\theta(\tau)} e^{-i\theta(0)}\rangle e^{-i\omega\tau}\, d\tau. \tag{5.5}$$

The phase noise probably arises from the voltage fluctuations generated by the other modes so that, knowing their fluctuations, we could reuse the $P(E)$ machinery and compute the spectrum, but this is out of the current scope of this chapter. A simple estimate can be made by supposing that the phase fluctuations are dominated, at long times, by a Brownian component $\langle[\theta(\tau)-\theta(0)]^2\rangle \approx 2|\tau|/\tau_\theta$, with τ_θ the characteristic diffusion time previously mentioned. Performing the Fourier transform we have

$$S(\omega-\omega_0) \propto \frac{1}{1+(\omega\tau_\theta)^2}, \tag{5.6}$$

meaning that the linewidth of the emission is $\gamma = 1/\tau_\theta$. In our case we have $\gamma \sim 1\,\mathrm{MHz}$, yielding a characteristic diffusion time of about $1\,\mu\mathrm{s}$. The cause of this diffusion is not known with certainty but we can speculate that it is caused by voltage fluctuations, either coming from the non-zero temperatures of the other modes or simply the imperfect external voltage bias.

As predicted by the theory the laser is not monochromatic, this was already visible in the measurements of the previous chapter on Figure 4.11 where the first four odd modes can be seen to participate in the lasing. Panels (c) and (d) shows the same type of emission measurements versus bias voltage but with a narrower bandwidth of 3 MHz, allowing us to only measure the coherent part of the emission. From the emitted power we can estimate if the harmonics follow the decomposition (5.4) of the triangular signal. The emitted power by a mode is given by $P_m = \kappa_m \hbar\omega_m |\alpha_m|^2$. Taking the bias point at $V = 0.17\,\mathrm{mV}$ where $P_0 = 50\,\mathrm{fW}$, $P_1 = 2\,\mathrm{fW}$, $P_2 = 0.5\,\mathrm{fW}$, and assuming that the κ_m are similar for the first three modes, we get $|\alpha_1|/|\alpha_0| \approx 0.12$ and $|\alpha_2|/|\alpha_0| \approx 0.045$. This has to be compared to the expected values for the triangular signal $|\alpha_1|/|\alpha_0| = 1/3\sqrt{3} \approx 0.19$ and $|\alpha_2|/|\alpha_0| = 1/5\sqrt{5} \approx 0.09$. This discrepancy likely arises from multiple factors, the most significant being the uncertainty in the calibration of the system gain, that we estimated to be around $\pm 1\,\mathrm{dB}$. Moreover, the emitted powers do not have the same dependency to the bias voltage, meaning the harmonic balance is not constant with respect to the bias anyway.

5.2.2 Phase diagram

The system has three distinct regimes: a hot regime at low voltages, characterized by the photonic Joule effect we described in the previous chapter, a coherent regime, and a trivial cold regime. Drawing from the phase transition analogy, we define an order parameter in our system. A natural choice is the average complex amplitude

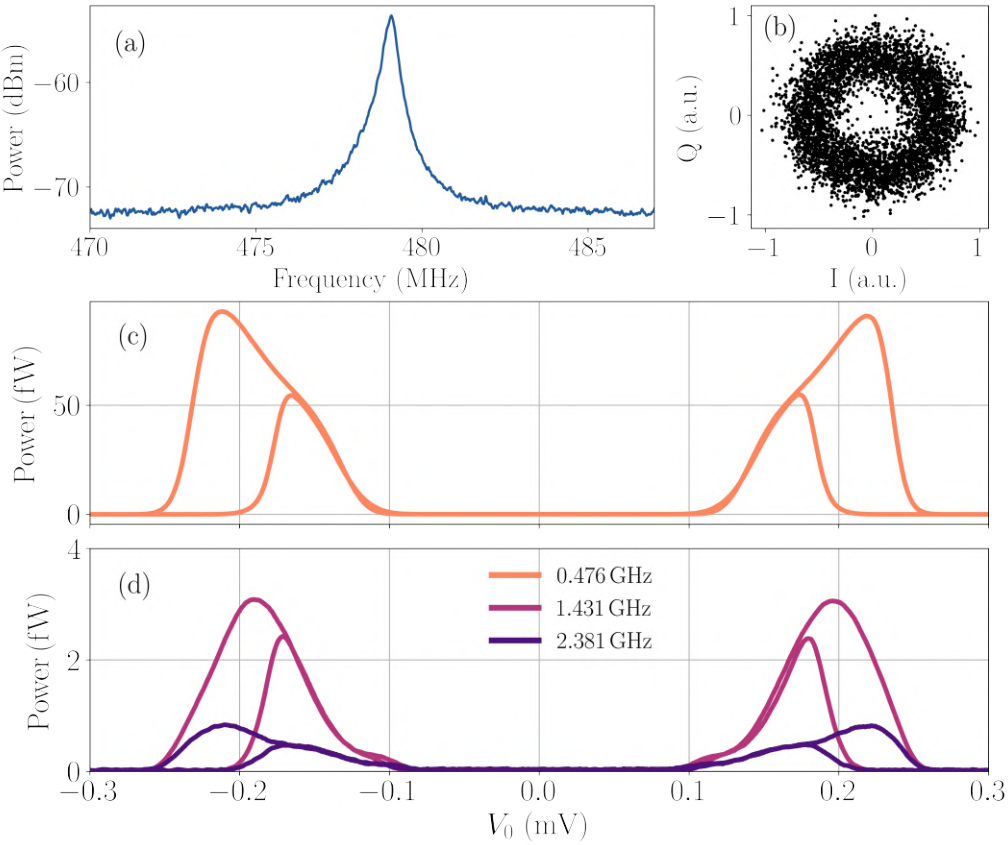

Figure 5.4: Coherent emission from the laser at zero flux. Panel (a) shows the emitted spectrum of the first mode at the bias value $V_0 = 0.18\,\mathrm{mV}$. The emission is confirmed to be coherent by measuring the quadratures of the mode (b). The emission of the first three harmonics of the laser versus voltage bias, measured with a resolution bandwidth of 3 MHz, are plotted in (c) and (d). Close to transition between hot and coherent ($V \sim 0.12\,\mathrm{mV}$), the measurement underestimates the emitted power because the frequency of the emitted radiation shifts more than the measurement bandwidth (see Figure 5.5 for the first mode).

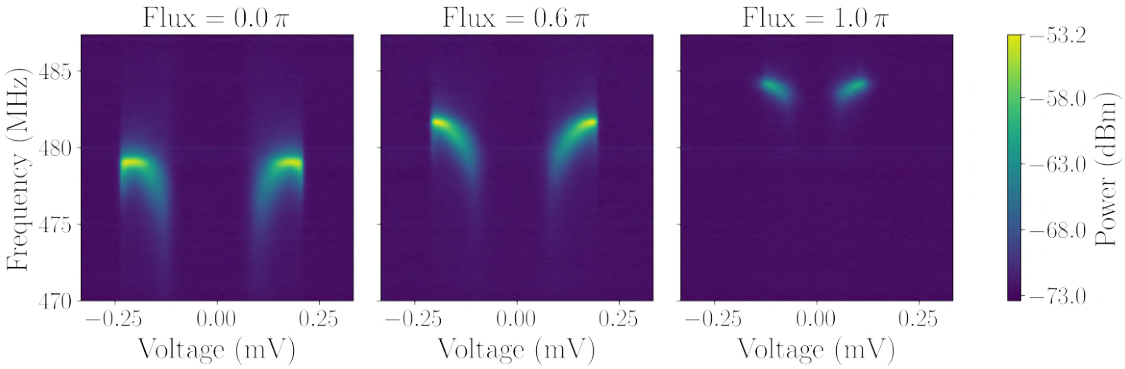

Figure 5.5: Dependence of the laser emission on the voltage and flux threading the SQUID. The boundaries of the coherent phase are located at the points where the emission discontinuously disappears.

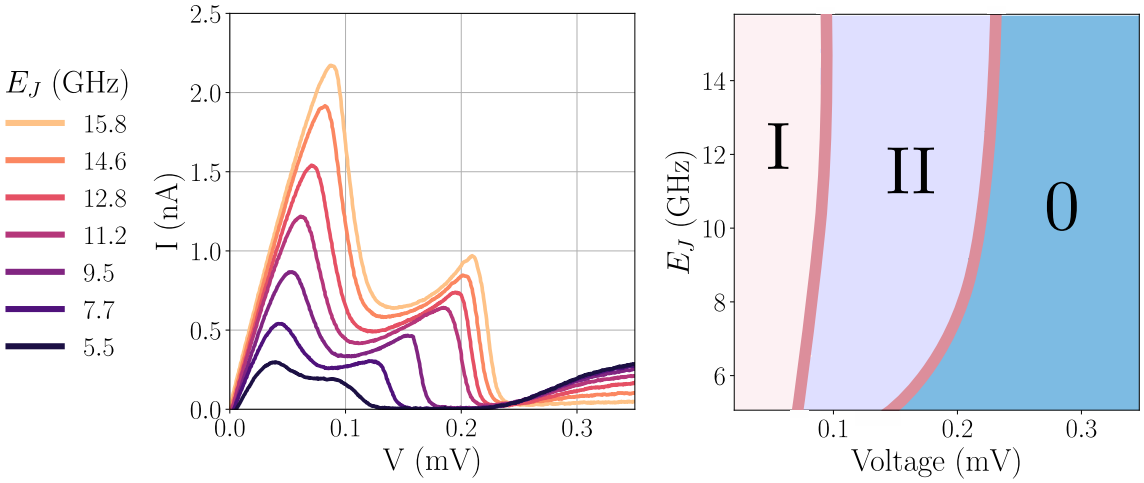

Figure 5.6: Left: IV characteristics as a function of the E_J of the small junction, obtained by sweeping the flux in the SQUID. Right: Extracted phase diagram of the system using the dependence of the coherent emission on voltage and flux as shown on Figure 5.5. It represents the three regime: the hot thermal regime (I) characterized by the photonic Joule effect, the coherent regime (II), and the trivial cold regime (0).

of the lowest mode $\langle \alpha_0 \rangle$ which vanishes in the thermal phase and acquires a nonzero value in the coherent phase[3]. In order to obtain the phase diagram we measure this order parameter of the system versus the applied voltage and the flux threading the SQUID, tuning the E_J of the small junction. The voltage dependence of the emission for three different fluxes is shown on Figure 5.5 where the limits of the coherent regime are clearly visible.

From this measurement, we define the boundaries of the coherent regime when the average emitted power in this restricted bandwidth exceeds a threshold value. Since the transition is sharp in voltage this exact value does not impact the phase diagram, and we take it to be $-72\,\mathrm{dBm}$ at the input of the analyzer. The resulting phase diagram is given on Figure 5.6a where we converted the flux Φ threading the SQUID to a variation of the Josephson energy using the formula [58]

$$E_J(\Phi) = E_J(0)\sqrt{\cos^2\left(\frac{\Phi}{2\Phi_0}\right) + d^2 \sin^2\left(\frac{\Phi}{2\Phi_0}\right)}. \tag{5.7}$$

The asymmetry $d = (E_{J_1} - E_{J_2})/(E_{J_1} + E_{J_2})$ of the SQUID is unknown to us, but we estimate it using the maximum dc current $I_{\max}(\Phi)$ in the IV curve at different flux values (see Figure 5.6). Assuming that this current is related to E_J^2 through second order perturbation theory[4] gives us $I_{\max}(\pi)/I_{\max}(0) \approx d^2$, allowing us to estimate $d \approx 30\,\%$.

Additionally, higher-order odd modes beyond the first four do not contribute to the coherent state and exhibit significantly increased losses in the lasing regime. Figure 5.7 compares the transmission coefficient in the cold regime at large bias to

[3] An equally correct choice would be the complex amplitude of $\phi(t)$.

[4] Technically, this is not true because of the photonic Joule effect. Indeed, the steady state current obtained from the theory of the previous chapter contains all orders E_J^n, but the leading order is always 2.

that in the lasing regime for the 12th and 13th odd modes. This behavior resembles a many-body system undergoing condensation, where a spectral gap emerges. In this scenario, photons injected into higher-frequency modes are expected to be efficiently down-converted into the condensate (the coherent signal) due to bosonic enhancement and the system's nonlinearity. Although, this seems like the most likely process for this loss of transmission, a definitive proof of this would require measuring the reflected signal at the modes frequencies to make sure it is not simply reflected at the sample input.

5.2.3 Fluctuations of the order parameter at the transition

When the system is biased near the boundary between the coherent and cold phases, it exhibits spontaneous switching between these two states. This behavior can be directly observed in real time by monitoring the coherent emission of the first mode as a function of time. The left panel of Figure 5.8 presents such a measurement, revealing discrete jumps between the two states.

By averaging these time-resolved measurements over long timescales, we can extract the probability distribution of the system occupying each attractor. Repeating this sampling across a range of voltage biases near the discontinuity in the IV curve allows us to track the evolution of the probability distribution as a function of bias voltage. As shown in the right panel of Figure 5.8, this evolution appears discontinuous within the bistable region, where the system intermittently undergoes stochastic excursions into one attractor for durations comparable to the measurement averaging time of 100 ms.

This discontinuous switching can be interpreted in several ways. From the laser point of view, this is reminiscent of the bistable switching in optical systems due to fluctuations [109–111]. From the condensed matter point of view, the total energy of the system, proportional to $\hbar\omega_0|\alpha_0|^2$, is clearly discontinuous at the II $\rightarrow$ 0 transition, making it a first-order phase transition. The switching could then be interpreted as the coexistence of the two phases near the transition point.

5.2.4 Injection-locking

Injection locking is a nonlinear synchronization phenomenon where a self-sustained oscillator locks its frequency and phase to that of an externally applied periodic signal when the external frequency is sufficiently close to the natural frequency of the oscillator. [45]. In our case, the self-sustained oscillator is realized by the coherent state oscillating at the fundamental frequency ω_0. To investigate injection-locking in our sample, we shine a pump tone at frequencies close to the laser frequency. Figure 5.9 shows the evolution of the coherent emission versus the pump power, for two different detuning values (2 MHz and 5 MHz). The laser clearly experiences frequency pulling, a characteristic behavior of the synchronization of coupled oscillators, until it locks with the pump at higher powers. Interestingly, in the locked state, the signal is not monochromatic as indicated by the presence of visible sidebands around the pump tone. The brightest sidebands carry a relative power of -20 dBc compared to the central carrier, and are detuned of about ~ 200 kHz with it. These sidebands were not investigated further at the time of measurement as I deemed them to be an artifact caused by either the microwave source used to gener-

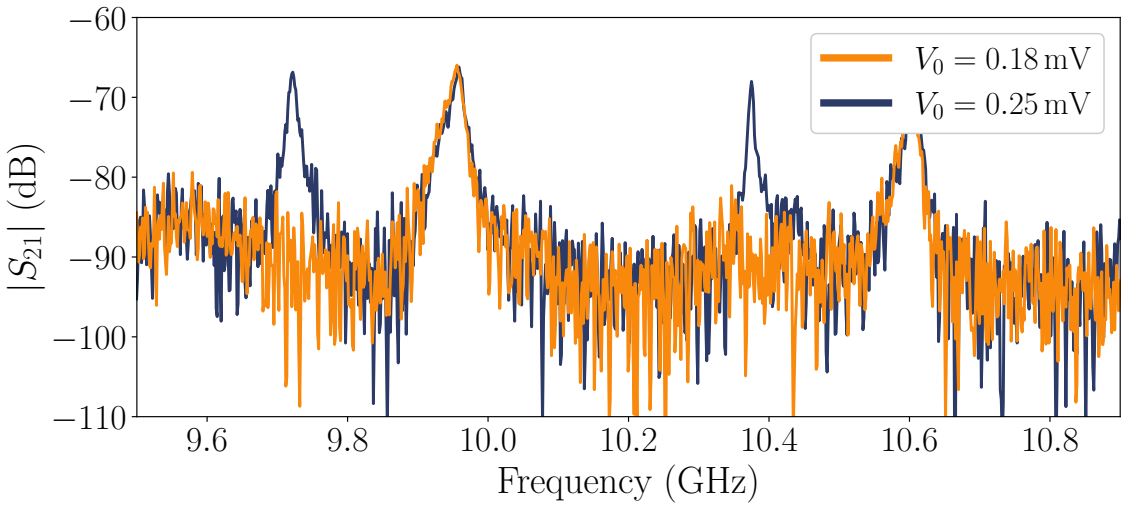

Figure 5.7: Comparison of the transmission of the sample between the cold regime (0) at $V_0 = 0.25\,\mathrm{mV}$ and the coherent regime (II) at $V_0 = 0.18\,\mathrm{mV}$. In the coherent regime the odd modes (shown here at 9.7 and 10.4 GHz) completely disappear due to their coupling to the condensate.

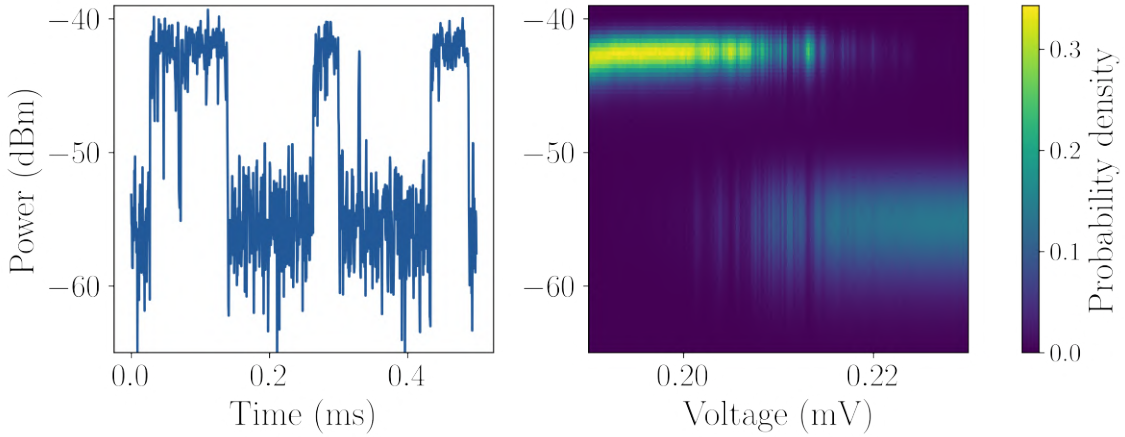

Figure 5.8: Fluctuations of the system close to the phase boundary. On the left we plot the time evolution of the coherent emission at 476 MHz at the bias value $V = 0.21\,\mathrm{mV}$. The bistability of the system is clearly visible along with the stochastic jump between the two states. By extracting the average time spent in each state we plot on the right the evolution of the probability density of system versus voltage bias.

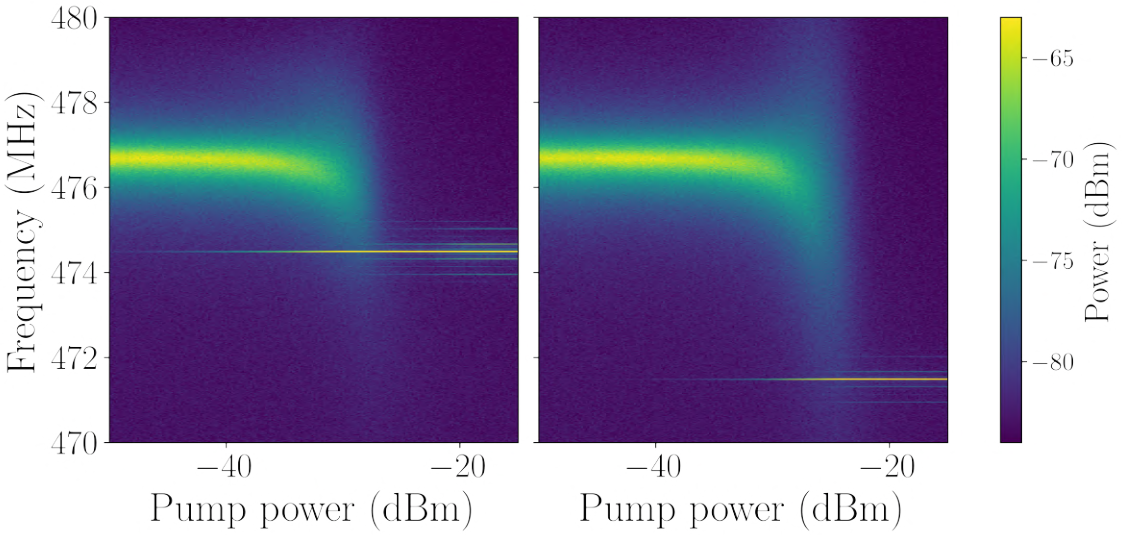

Figure 5.9: Demonstration of frequency pulling of the laser when a pump tone is injected close to it in frequency. The two panel show the evolution of the emitted spectrum versus frequency and pump power for two detunings with respect to the laser frequency. The detuning is 2 MHz on the left plot and 5 MHz on the right one.

ate the pump tone, or by the compression of the amplification chain. However, the datasheet of the source (R&S SMB-100A) specify that spectral leakage should be at worst −30 dBc, and the power at the input of the first amplifier (LNF-LNC0.2_3B) is on the order of −100 dBm when these sidebands appear, which is well below the compression point. Moreover, their appearance is always concomitant with the locking of the laser, which does not occur at the same power depending on the pump detuning. Nevertheless, further investigation is needed to conclude with certainty on their origin. Finally, it is important to note that the locking happens when the injected pump power roughly matches power of the bare emission $P_{\text{pump}} \sim P_{\text{laser}}$, which is consistent with the measurements of injection locking presented in Ref. [106], but in this case the driving tone can not be considered perturbative as is usually the case in the standard theory of injection-locking for lasers [45, 112].

5.3 Conclusion and arguments for the thermodynamic limit

In this chapter, we have explored the transition occurring in the circuit studied in the previous two chapters. By tuning the applied voltage the system can develop a coherent state in the lowest mode of the system while depleting the higher frequencies of excitations. While this transition bears strong similarities to conventional lasing in driven nonlinear systems, its many-body setting also allows us to draw analogy from the phase transitions of condensed matter.

Although numerical integration of the classical equations of motion successfully reproduces the transition, a more refined theoretical model is necessary to deepen our understanding. On the experimental part, a measurement of the statistical properties of the jumps at the bistability, shown on Figure 5.8 could be done, along with verifying that the suppression of higher-frequency modes indeed results from down-

conversion into the condensate. An interesting perspective of this down-conversion would be to see if it is possible to "kick-start" the laser with a few photons injected at high frequency, essentially using it as a photo-multiplier.

At a more fundamental level, this system could provide a way to smoothly interpolate between laser physics and the physics of phase transitions, furthering our understanding of driven-dissipative many-body dynamics. However, as stated at the start of this chapter, there is no certainty yet that this transition persist in the thermodynamic limit. Nonetheless, some heuristic arguments in support of this possibility can be made. First, the coupling constants Λ_m are independent of the system size N. This can be read from their definition (4.2), where the ratio $\Delta\omega_m/\omega_m$ does not depend on N for a given index m. Indeed, we have $\Delta\omega_m \propto 1/N$ and $\omega_m \approx (2m+1)\omega_0 \propto (2m+1)/N$, so that, while the frequencies of the lowest modes vanish in the limit, their couplings are constant. Additionally, as discussed for the photonic Joule effect in the previous chapter, the system losses are determined by the reflection at the boundary of the array, meaning $\kappa_m \propto 1/N$ and $\kappa_m/\omega_m = \text{const}$. We could therefore argue that the coherent steady-state is independent of N, although the characteristic time of the transition should scale with $1/\omega_0 \propto N$. Another important ingredient of this transition seems to be the commensurability of the frequencies of the system $\omega_m \approx (2m+1)\omega_0$. I did not thoroughly study the impact of this on the transition, but insights gained from the numerical integration of Eqs. (5.1) indicate it plays a strong role in the transition. Additionally, I observed that introducing disorder in the frequencies—i.e. randomly shifting ω_m by a small amount—led to an increase in size of the thermal phase (I) in the phase diagram, at the expense of the coherent part (II). In the absence of disorder, the main source of incommensurability is the dispersion of the array, given by $\partial^2\omega/\partial k^2$, along with the phase shift induced by that small junction capacitance. Another argument for the thermodynamic limit of the transition is thus that this dispersion vanishes in the limit $\omega \to 0$, possibly favoring the coherent solution in the large N limit. While these arguments hint that the transition should survive in the thermodynamic limit, a more rigorous theoretical study is obviously needed to claim that we are in presence of a phase transition.

Chapter 6

Conclusion and perspectives

6.1 Conclusion

In this thesis we have explored the dynamics of a small Josephson junction embedded in a high-impedance environment, composed of an array of Josephson junction itself. To fully characterize this system we measured and analyzed both the finite-frequency response of the system and its transport properties. This was achieved by combining the microwave expertise acquired from circuit-QED with the transport measurements routinely done in the condensed-matter community.

This allowed us to observe for the first time the dual Shapiro steps in Josephson junctions. Upon driving resonantly a mode of our circuit at a frequency f we measured quantized current steps in the current-voltage characteristic satisfying the fundamental relation $I = 2ef$. Furthermore, we explained theoretically the forest of current peaks, space by twice the superconducting gap, observed when voltage biasing an array of junctions. On each current peak, a junction in the chain turns resistive, adding its normal state resistance to the impedance felt by the small junction. This gave us the possibility to effectively sweep the impedance of the transmission line through the applied voltage. Moreover, this also reduced the quality factor of the modes, helping them to cool down, which turned out to be an essential ingredient for the observation of dual Shapiro steps.

Indeed, we discovered that, due to the low intrinsic losses of our transmission line, the small junction could overheat the modes by populating them through inelastic tunneling, thereby realizing the photonic counterpart of the well-known Joule effect. We developed three theoretical approaches to describe this novel effect: the first two built upon $P(E)$ theory, a well-established perturbative approach for tunnel junctions. The third approach relied on solving numerically the full classical dynamics of our circuit. Interestingly, we saw that the system generates its own noise thanks to its chaotic dynamics, validating the $P(E)$-approaches which rely on an incoherent bath state.

We then experimentally studied the photonic Joule effect by measuring the emitted radiation of the sample on a 0.1–12 GHz bandwidth, giving us access to the photonic populations of the first fifteen modes of our system. We repeated this measurement as a function of voltage bias, allowing us to confront not only the macroscopic observable, like the tunneling current, to theory but also the microscopic ones, like the populations of the modes. Overall, a good agreement between the experiment and theory was reached at low voltages, despite the absence of fitting

parameters.

However, at larger voltages, we experimentally saw that our system undergoes an incoherent-to-coherent transition reminiscent of condensation transitions in condensed matter, or lasing transitions in optics. Indeed, past a certain voltage, the first few modes of our device develop a coherent state, while other modes see their losses greatly increased, making them almost impossible to see in transmission measurements. In particular, we used the bright coherent emission of the first mode to measure the boundary of this transition in the parameter space spanned by the voltage bias and the Josephson energy of the small junction. By biasing the system close one of these boundaries, we could also observe in real time the system switching back and forth between a cold inert state and the coherent regime. Finally, we showcased that a strong pump tone, weakly detuned in frequency from the coherent emission, could pull it and lock it onto the pump, akin to injection-locking measurements done in lasers.

6.2 Perspectives

This work highlight the wealth of phenomena that can occur in the dynamics of a small Josephson junction coupled to a high-impedance transmission line. The findings of this thesis are merely the start, and so here we shall highlight some future possible prospects of this work.

6.2.1 Order of resistive switching in a long Josephson junction array

As we saw in Chapter 3, when one applies a dc voltage, which is large compared to the superconducting gap, to an array of junctions, they turn resistive one after the other. An interesting question, which was not addressed in this thesis, is what determines the order of switching of the junctions. In a short chain of 4 junctions, we saw that it was random, but in our sample the system is composed of thousands of junctions. Moreover, we expect the phase fluctuations, which are not uniform in our system due to the ground capacitance, to play a big role in this switching mechanism. Clarifying this issue might also help understand the non-trivial envelope of the 2Δ peaks we observed. One might also envision to control this switching by applying some external finite-frequency drive tone to shape the voltage drop distribution in the chain (although the usual Shapiro effect might come into play under irradiation).

6.2.2 Suppression of the photonic Joule effect with impedance matching

We saw that the overheating of the modes happens because they do not cool down sufficiently fast to evacuate the power IV injected by Cooper pairs tunneling across the small junction. One way to remove this heating is to just induce bulk losses in the line by shunting some part of it with resistive components, but one then has to give up on measuring the excitation of the bath. A second solution is to use impedance matching, either through microwave tapering or some other transformer; this would keep the access to the emitted radiation while increasing the losses of

the modes, keeping them cold. It is also noteworthy that this would give access to scattering experiments in a high-impedance regime where quantum fluctuations become important.

6.2.3 Observation of the Bloch oscillations

If the photonic Joule effect is properly suppressed, it will now be possible to properly probe the low energy physics of the small junction. In particular, direct measurements of the emitted radiation due to Bloch oscillations should be possible. Moreover, if the transmission line is impedance matched, as described in the previous paragraph, finite-frequency measurement will not be limited anymore to the discrete resonant frequencies of the system. Indeed, in a tapered sample, a continuous frequency band should be available (above a characteristic frequency inversely proportional to the length of the taper), allowing for a measurement of the relation $I = 2ef$ over a wide bandwidth.

6.2.4 Theoretical study of the lasing transition

Despite the fact that the numerical simulations reproduce the lasing transition, discussed in Chapter 4 and 5, a more comprehensive theoretical model is needed. In particular, one might wonder if the coherent regime survives in the thermodynamic limit. This is motivated by the fact that the coupling constant of the first mode Λ_0 does not depend on the size of the system. Obviously its frequency ω_0 goes to 0 in this limit and a coherent state at zero frequency does not make sense. The question is thus whether there exists a coherent regime for any arbitrarily large, but finite, N (although the coherent state might take an equivalently large time to develop).

6.2.5 Effect of the non-linearity of the array

In this thesis we ignored the non-linearity coming from the large junctions forming the array. However, most of the phenomena we investigated involve high-energy states of the bath, either due to a high temperature or a large coherent state. This might invalidate the assumption that the chain is a perfectly linear environment, and impact the dynamics experimentally. In particular, we have mentioned that the dispersion of the system impact the appearance of the coherent state in the numerical model, and so it would be interesting to see if the non-linearity of the chain can counteract this, similarly to what stabilizes solitons in non-linear media.

6.2.6 Chaos in the classical model

In Chapter 4, we observed that the solutions to the full classical equations of motion exhibited chaotic behavior, naturally leading to a Gaussian distribution in phase space. While the chaotic dynamics were not explored in detail, investigating their origin and characteristics would be an interesting direction for future work. For example, the minimal number of modes required to exhibit chaos at a given voltage and whether it is always correlated with the smoothness of $P(2eV)$, or some equivalent quantity for the coherent regime.

Bibliography

[1] H. Nyquist. "Thermal Agitation of Electric Charge in Conductors". In: *Physical Review* 32.1 (July 1928), pp. 110–113. ISSN: 0031-899X. DOI: 10.1103/PhysRev.32.110. (Visited on 10/12/2023) (Cited on page 5).

[2] Lars Onsager. "Reciprocal Relations in Irreversible Processes. I." In: *Physical Review* 37.4 (Feb. 1931), pp. 405–426. DOI: 10.1103/PhysRev.37.405 (Cited on page 5).

[3] Herbert B. Callen and Theodore A. Welton. "Irreversibility and Generalized Noise". In: *Physical Review* 83.1 (July 1951), pp. 34–40. DOI: 10.1103/PhysRev.83.34 (Cited on page 5).

[4] R. Kubo. "The Fluctuation-Dissipation Theorem". In: *Reports on Progress in Physics* 29.1 (Jan. 1966), p. 255. ISSN: 0034-4885. DOI: 10.1088/0034-4885/29/1/306 (Cited on page 5).

[5] C. Gardiner and Peter Zoller. *Quantum Noise: A Handbook of Markovian and Non-Markovian Quantum Stochastic Methods with Applications to Quantum Optics*. Springer Science & Business Media, 2004 (Cited on pages 5, 17, 41, 70, 113, 122, 123, 126).

[6] U. Weiss. *Quantum Dissipative Systems*. Series in Modern Condensed Matter Physics. World Scientific, 2008. ISBN: 978-981-279-162-7 (Cited on pages 5, 33).

[7] K. K. Likharev and A. B. Zorin. "Theory of the Bloch-wave Oscillations in Small Josephson Junctions". In: *Journal of Low Temperature Physics* 59.3 (May 1985), pp. 347–382. ISSN: 1573-7357. DOI: 10.1007/BF00683782 (Cited on pages 6, 12, 16, 19, 21, 27, 46).

[8] M. Tinkham. *Introduction to Superconductivity*. Vol. 1. Courier Corporation, 2004 (Cited on pages 10, 11, 20).

[9] A. J. Leggett. *Quantum Liquids: Bose Condensation and Cooper Pairing in Condensed-Matter Systems*. Oxford university press, 2006 (Cited on page 10).

[10] P. W. Anderson. "Special Effects in Superconductivity". In: *Lectures on the Many-body Problems*. Elsevier, 1964, pp. 113–135. ISBN: 978-0-12-395616-3. DOI: 10.1016/B978-0-12-395616-3.50010-3 (Cited on page 10).

[11] D. V. Averin and K. K. Likharev. "Single Electronics: A Correlated Transfer of Single Electrons and Cooper Pairs in Systems of Small Tunnel Junctions". In: *Modern Problems in Condensed Matter Sciences*. Ed. by B. L. Altshuler, P. A. Lee, and R. A. Webb. Vol. 30. Elsevier, 1991, pp. 173–271 (Cited on pages 11, 21).

[12] S. M. Apenko. "Environment-Induced Decompactification of Phase in Josephson Junctions". In: *Physics Letters A* 142.4 (Dec. 1989), pp. 277–281. ISSN: 0375-9601. DOI: 10.1016/0375-9601(89)90329-0 (Cited on page 11).

[13] Gerd Schön and A. D. Zaikin. "Quantum Coherent Effects, Phase Transitions, and the Dissipative Dynamics of Ultra Small Tunnel Junctions". In: *Physics Reports* 198.5 (Dec. 1990), pp. 237–412. ISSN: 0370-1573. DOI: 10.1016/0370-1573(90)90156-V (Cited on pages 11, 16, 20, 32).

[14] A. A. Golubov, M. Yu. Kupriyanov, and E. Il'ichev. "The Current-Phase Relation in Josephson Junctions". In: *Reviews of Modern Physics* 76.2 (Apr. 2004), pp. 411–469. DOI: 10.1103/RevModPhys.76.411 (Cited on page 11).

[15] L. D. Landau, E. M. Lifshitz, and L. P. Pitaevskii. *Statistical Physics: Theory of the Condensed State*. Vol. 9. Butterworth-Heinemann, 1980 (Cited on pages 12, 13).

[16] E. N. Adams II. "The Crystal Momentum as a Quantum Mechanical Operator". In: *The Journal of Chemical Physics* 21.11 (Nov. 1953), pp. 2013–2017. ISSN: 0021-9606. DOI: 10.1063/1.1698734 (Cited on page 13).

[17] J. P. Rouyet and J. Zak. "Bravais-Lattice Operator in Crystals". In: *Physical Review B* 23.2 (Jan. 1981), pp. 561–564. ISSN: 0163-1829. DOI: 10.1103/PhysRevB.23.561 (Cited on page 13).

[18] V. Bouchiat, D. Vion, P. Joyez, D. Esteve, and M. H. Devoret. "Quantum Coherence with a Single Cooper Pair". In: *Physica Scripta* 1998.T76 (Jan. 1998), p. 165. DOI: 10.1238/Physica.Topical.076a00165 (Cited on page 14).

[19] J. A. Schreier, A. A. Houck, Jens Koch, D. I. Schuster, B. R. Johnson, J. M. Chow, J. M. Gambetta, J. Majer, L. Frunzio, M. H. Devoret, S. M. Girvin, and R. J. Schoelkopf. "Suppressing Charge Noise Decoherence in Superconducting Charge Qubits". In: *Physical Review B* 77.18 (May 2008), p. 180502. DOI: 10.1103/PhysRevB.77.180502 (Cited on page 14).

[20] A. B. Zorin. "Bloch Inductance in Small-Capacitance Josephson Junctions". In: *Physical Review Letters* 96.16 (Apr. 2006), p. 167001. ISSN: 0031-9007, 1079-7114. DOI: 10.1103/PhysRevLett.96.167001. arXiv: cond-mat/0510435 (Cited on pages 14, 20, 21).

[21] Manuel Houzet, Tsuyoshi Yamamoto, and Leonid I. Glazman. "Microwave Spectroscopy of the Schmid Transition". In: *Physical Review B* 109.15 (Apr. 2024), p. 155431. DOI: 10.1103/PhysRevB.109.155431 (Cited on pages 14, 30–32, 34).

[22] A. Schmid. "Diffusion and Localization in a Dissipative Quantum System". In: *Physical Review Letters* 51.17 (Oct. 1983), pp. 1506–1509. ISSN: 0031-9007. DOI: 10.1103/PhysRevLett.51.1506 (Cited on page 16).

[23] Alexandre Blais, Arne L. Grimsmo, S. M. Girvin, and Andreas Wallraff. "Circuit Quantum Electrodynamics". In: *Reviews of Modern Physics* 93.2 (May 2021), p. 025005. ISSN: 0034-6861, 1539-0756. DOI: 10.1103/RevModPhys.93.025005. arXiv: 2005.12667 [quant-ph] (Cited on page 17).

[24] P. Krantz, M. Kjaergaard, F. Yan, T. P. Orlando, S. Gustavsson, and W. D. Oliver. "A Quantum Engineer's Guide to Superconducting Qubits". In: *Applied Physics Reviews* 6.2 (June 2019), p. 021318. ISSN: 1931-9401. DOI: 10.1063/1.5089550 (Cited on page 17).

[25] P. Forn-Díaz, L. Lamata, E. Rico, J. Kono, and E. Solano. "Ultrastrong Coupling Regimes of Light-Matter Interaction". In: *Reviews of Modern Physics* 91.2 (June 2019), p. 025005. DOI: 10.1103/RevModPhys.91.025005 (Cited on page 17).

[26] Anton Frisk Kockum, Adam Miranowicz, Simone De Liberato, Salvatore Savasta, and Franco Nori. "Ultrastrong Coupling between Light and Matter". In: *Nature Reviews Physics* 1.1 (Jan. 2019), pp. 19–40. ISSN: 2522-5820. DOI: 10.1038/s42254-018-0006-2 (Cited on page 17).

[27] Markus Ansmann, H. Wang, Radoslaw C. Bialczak, Max Hofheinz, Erik Lucero, M. Neeley, A. D. O'Connell, D. Sank, M. Weides, J. Wenner, A. N. Cleland, and John M. Martinis. "Violation of Bell's Inequality in Josephson Phase Qubits". In: *Nature* 461.7263 (Sept. 2009), pp. 504–506. ISSN: 1476-4687. DOI: 10.1038/nature08363 (Cited on page 17).

[28] Z. K. Minev, S. O. Mundhada, S. Shankar, P. Reinhold, R. Gutiérrez-Jáuregui, R. J. Schoelkopf, M. Mirrahimi, H. J. Carmichael, and M. H. Devoret. "To Catch and Reverse a Quantum Jump Mid-Flight". In: *Nature* 570.7760 (June 2019), pp. 200–204. ISSN: 1476-4687. DOI: 10.1038/s41586-019-1287-z (Cited on page 17).

[29] K. W. Murch, S. J. Weber, C. Macklin, and I. Siddiqi. "Observing Single Quantum Trajectories of a Superconducting Quantum Bit". In: *Nature* 502.7470 (Oct. 2013), pp. 211–214. ISSN: 1476-4687. DOI: 10.1038/nature12539 (Cited on page 17).

[30] P. Campagne-Ibarcq, L. Bretheau, E. Flurin, A. Auffèves, F. Mallet, and B. Huard. "Observing Interferences between Past and Future Quantum States in Resonance Fluorescence". In: *Physical Review Letters* 112.18 (May 2014), p. 180402. DOI: 10.1103/PhysRevLett.112.180402 (Cited on page 17).

[31] A. O. Caldeira and A. J. Leggett. "Influence of Dissipation on Quantum Tunneling in Macroscopic Systems". In: *Physical Review Letters* 46.4 (Jan. 1981), pp. 211–214. DOI: 10.1103/PhysRevLett.46.211 (Cited on pages 17, 34).

[32] Geva Arwas, Vladimir E. Manucharyan, and Cristiano Ciuti. "Metrics and Properties of Optimal Gauges in Multimode Cavity QED". In: *Physical Review A* 108.2 (Aug. 2023), p. 023714. DOI: 10.1103/PhysRevA.108.023714 (Cited on page 17).

[33] Konstantin K Likharev. *Dynamics of Josephson Junctions and Circuits*. Routledge, 2022 (Cited on pages 19–21, 25, 34, 52).

[34] Vinay Ambegaokar and B. I. Halperin. "Voltage Due to Thermal Noise in the Dc Josephson Effect". In: *Physical Review Letters* 22.25 (June 1969), pp. 1364–1366. ISSN: 0031-9007. DOI: 10.1103/PhysRevLett.22.1364 (Cited on pages 20, 26).

[35] G.-L. Ingold and Yu. V. Nazarov. "Charge Tunneling Rates in Ultrasmall Junctions". In: *Single Charge Tunneling*. Ed. by H. Grabert and M. H. Devoret. Vol. 294. NATO ASI Series B. Plenum Press, New York, 1992, pp. 21–107 (Cited on pages 20, 27–29, 31, 32, 37, 115, 129).

[36] M. H. Devoret, D. Esteve, H. Grabert, G.-L. Ingold, H. Pothier, and C. Urbina. "Effect of the Electromagnetic Environment on the Coulomb Blockade in Ultrasmall Tunnel Junctions". In: *Physical Review Letters* 64.15 (Apr. 1990), pp. 1824–1827. DOI: 10.1103/PhysRevLett.64.1824 (Cited on pages 20, 27, 31).

[37] Max Hofheinz, Fabien Portier, Quentin Baudouin, Philippe Joyez, Denis Vion, Patrice Bertet, Patrice Roche, and Daniel Esteve. "The Bright Side of Coulomb Blockade". In: *Physical Review Letters* 106.21 (May 2011), p. 217005. ISSN: 0031-9007, 1079-7114. DOI: 10.1103/PhysRevLett.106.217005. arXiv: 1102.0131 [cond-mat, physics:quant-ph] (Cited on pages 20, 29, 32).

[38] Vladislav D. Kurilovich, Benjamin Remez, and Leonid I. Glazman. *Quantum Theory of Bloch Oscillations in a Resistively Shunted Transmon*. Mar. 2024. DOI: 10.48550/arXiv.2403.04624. arXiv: 2403.04624 [cond-mat] (Cited on page 20).

[39] W. Guichard and F. W. J. Hekking. "Phase-Charge Duality in Josephson Junction Circuits: Role of Inertia and Effect of Microwave Irradiation". In: *Physical Review B* 81.6 (Feb. 2010), p. 064508. ISSN: 1098-0121, 1550-235X. DOI: 10.1103/PhysRevB.81.064508. arXiv: 0909.3749 [cond-mat] (Cited on pages 21, 23, 26).

[40] Ulrich Geigenmüller and Gerd Schön. "Single Electron Effects and Bloch Oscillations in Normal and Superconducting Tunnel Junctions". In: *Physica B: Condensed Matter* 152.1 (Aug. 1988), pp. 186–202. ISSN: 0921-4526. DOI: 10.1016/0921-4526(88)90087-7 (Cited on pages 21, 35, 37).

[41] A. D. Zaikin and I. N. Kosarev. "Quantum Coherent Effects and Zener Tunneling in Superconducting Tunnel Junctions". In: *Physics Letters A* 131.2 (Aug. 1988), pp. 125–130. ISSN: 0375-9601. DOI: 10.1016/0375-9601(88)90671-8 (Cited on pages 21, 22, 35).

[42] A.D. Zaikin and D.S. Golubev. "Effect of Environment on Interband Tunneling in Ultrasmall Josephson Junctions". In: *Physics Letters A* 164.3-4 (Apr. 1992), pp. 337–344. ISSN: 03759601. DOI: 10.1016/0375-9601(92)91117-A (Cited on pages 21, 22, 35).

[43] J. M. Schmidt, A. N. Cleland, and John Clarke. "Resonant Tunneling in Small Current-Biased Josephson Junctions". In: *Physical Review B* 43.1 (Jan. 1991), pp. 229–238. DOI: 10.1103/PhysRevB.43.229 (Cited on pages 21, 34).

[44] P. Silvestrini, V. G. Palmieri, B. Ruggiero, and M. Russo. "Observation of Energy Levels Quantization in Underdamped Josephson Junctions above the Classical-Quantum Regime Crossover Temperature". In: *Physical Review Letters* 79.16 (Oct. 1997), pp. 3046–3049. DOI: 10.1103/PhysRevLett.79.3046 (Cited on pages 21, 34).

[45] A. Pikovsky, M. Rosenblum, and J. Kurths. *Synchronization: A Universal Concept in Nonlinear Sciences*. Cambridge Nonlinear Science Series. Cambridge University Press, 2001. ISBN: 978-0-521-59285-7 (Cited on pages 26, 92, 94).

[46] B. A. Huberman, J. P. Crutchfield, and N. H. Packard. "Noise Phenomena in Josephson Junctions". In: *Applied Physics Letters* 37.8 (Oct. 1980), pp. 750–752. ISSN: 0003-6951. DOI: 10.1063/1.92020 (Cited on page 26).

[47] R. L. Kautz. "Noise, Chaos, and the Josephson Voltage Standard". In: *Reports on Progress in Physics* 59.8 (Aug. 1996), p. 935. ISSN: 0034-4885. DOI: 10.1088/0034-4885/59/8/001 (Cited on page 26).

[48] L. J. Landau. "Bessel Functions: Monotonicity and Bounds". In: *Journal of the London Mathematical Society* 61.1 (2000), pp. 197–215 (Cited on page 26).

[49] P. K. Tien and J. P. Gordon. "Multiphoton Process Observed in the Interaction of Microwave Fields with the Tunneling between Superconductor Films". In: *Physical Review* 129.2 (Jan. 1963), pp. 647–651. DOI: 10.1103/PhysRev.129.647 (Cited on page 27).

[50] Antonio Barone and Gianfranco Paterno. *Physics and Applications of the Josephson Effect*. Nashville, TN: John Wiley & Sons, July 1982 (Cited on page 27).

[51] Federico Borletto, Luca Giacomelli, and Cristiano Ciuti. "Circuit Quantum Electrodynamics of Direct and Dual Shapiro Steps with Finite-Size-Transmission-Line Resonators". In: *Physical Review Applied* 22.5 (Nov. 2024), p. 054061. DOI: 10.1103/PhysRevApplied.22.054061 (Cited on page 27).

[52] E. O. Göbel and U Siegner. *The New International System of Units (SI) – Quantum Metrology and Quantum Standards*. John Wiley & Sons, Ltd, 2019. ISBN: 978-3-527-81448-0 (Cited on page 27).

[53] D. B. Haviland, L. S. Kuzmin, P. Delsing, K. K. Likharev, and T. Claeson. "Experimental Evidence for the Coulomb Blockade of Cooper Pair Tunneling and Bloch Oscillations in Single Josephson Junctions". In: *Zeitschrift fur Physik B Condensed Matter* 85.3 (Oct. 1991), pp. 339–347. ISSN: 0722-3277, 1434-6036. DOI: 10.1007/BF01307629 (Cited on page 27).

[54] Leonid Kuzmin, Yuri Pashkin, Alexander Zorin, and Tord Claeson. "Linewidth of Bloch Oscillations in Small Josephson Junctions". In: *Physica B: Condensed Matter* 203.3 (Dec. 1994), pp. 376–380. ISSN: 0921-4526. DOI: 10.1016/0921-4526(94)90083-3 (Cited on pages 27, 37).

[55] Nicolò Crescini, Samuel Cailleaux, Wiebke Guichard, Cécile Naud, Olivier Buisson, Kater W. Murch, and Nicolas Roch. "Evidence of Dual Shapiro Steps in a Josephson Junction Array". In: *Nature Physics* 19.6 (June 2023), pp. 851–856. ISSN: 1745-2481. DOI: 10.1038/s41567-023-01961-4 (Cited on page 27).

[56] F. Kaap, C. Kissling, V. Gaydamachenko, L. Grünhaupt, and S. Lotkhov. "Demonstration of Dual Shapiro Steps in Small Josephson Junctions". In: *Nature Communications* 15.1 (2024), p. 8726 (Cited on pages 27, 33, 37, 58).

[57] Rais S. Shaikhaidarov, Kyung Ho Kim, Jacob Dunstan, Ilya Antonov, Dmitry Golubev, Vladimir N. Antonov, and Oleg V. Astafiev. "Quantized Current Steps Due to the Synchronization of Microwaves with Bloch Oscillations in Small Josephson Junctions". In: *Nature Communications* 15.1 (Oct. 2024), p. 9326. ISSN: 2041-1723. DOI: 10.1038/s41467-024-53600-y (Cited on pages 27, 33, 37, 58).

[58] U. Vool and M. H. Devoret. "Introduction to Quantum Electromagnetic Circuits". In: *International Journal of Circuit Theory and Applications* 45.7 (July 2017), pp. 897–934. ISSN: 0098-9886, 1097-007X. DOI: 10.1002/cta.2359. arXiv: 1610.03438 [quant-ph] (Cited on pages 28, 40, 91, 115).

[59] Ines Safi and Philippe Joyez. "Time-Dependent Theory of Nonlinear Response and Current Fluctuations". In: *Physical Review B* 84.20 (Nov. 2011), p. 205129. DOI: 10.1103/PhysRevB.84.205129 (Cited on page 30).

[60] John R. Tucker and Marc J. Feldman. "Quantum Detection at Millimeter Wavelengths". In: *Reviews of Modern Physics* 57.4 (Oct. 1985), pp. 1055–1113. DOI: 10.1103/RevModPhys.57.1055 (Cited on page 30).

[61] A. H. Worsham, N. G. Ugras, D. Winkler, D. E. Prober, N. R. Erickson, and P. F. Goldsmith. "Quantum Tunneling Currents in a Superconducting Junction". In: *Physical Review Letters* 67.21 (Nov. 1991), pp. 3034–3037. DOI: 10.1103/PhysRevLett.67.3034 (Cited on page 30).

[62] Inès Safi. "Driven Quantum Circuits and Conductors: A Unifying Perturbative Approach". In: *Physical Review B* 99.4 (Jan. 2019), p. 045101. DOI: 10.1103/PhysRevB.99.045101 (Cited on page 30).

[63] Luca Giacomelli and Cristiano Ciuti. "Emergent Quantum Phase Transition of a Josephson Junction Coupled to a High-Impedance Multimode Resonator". In: *Nature Communications* 15.1 (June 2024), p. 5455. ISSN: 2041-1723. DOI: 10.1038/s41467-024-48558-w (Cited on page 32).

[64] Nicolas Paris, Luca Giacomelli, Romain Daviet, Cristiano Ciuti, Nicolas Dupuis, and Christophe Mora. *Resilience of the Quantum Critical Line in the Schmid Transition*. July 2024. DOI: 10.48550/arXiv.2407.01699. arXiv: 2407.01699 [cond-mat] (Cited on pages 32, 33).

[65] Albert Schmid. "Diffusion and Localization in a Dissipative Quantum System". In: *Physical Review Letters* 51.17 (Oct. 1983), pp. 1506–1509. DOI: 10.1103/PhysRevLett.51.1506 (Cited on page 32).

[66] Philip W. Anderson. *Basic Notions Of Condensed Matter Physics*. Boca Raton: CRC Press, Mar. 2018. ISBN: 978-0-429-49411-6. DOI: 10.4324/9780429494116 (Cited on page 32).

[67] Romain Daviet and Nicolas Dupuis. "On the Nature of the Schmid Transition in a Resistively Shunted Josephson Junction". In: *Physical Review B* 108.18 (Nov. 2023), p. 184514. ISSN: 2469-9950, 2469-9969. DOI: 10.1103/PhysRevB.108.184514. arXiv: 2307.04835 [cond-mat] (Cited on page 33).

[68] L. S. Kuzmin, Yu. V. Nazarov, D. B. Haviland, P. Delsing, and T. Claeson. "Coulomb Blockade and Incoherent Tunneling of Cooper Pairs in Ultrasmall Junctions Affected by Strong Quantum Fluctuations". In: *Physical Review Letters* 67.9 (Aug. 1991), pp. 1161–1164. ISSN: 0031-9007. DOI: 10.1103/PhysRevLett.67.1161 (Cited on page 33).

[69] Diego Subero, Olivier Maillet, Dmitry S. Golubev, George Thomas, Joonas T. Peltonen, Bayan Karimi, Marco Marín-Suárez, Alfredo Levy Yeyati, Rafael Sánchez, Sunghun Park, and Jukka P. Pekola. "Bolometric Detection of Josephson Inductance in a Highly Resistive Environment". In: *Nature Communications* 14.1 (Dec. 2023), p. 7924. ISSN: 2041-1723. DOI: 10.1038/s41467-023-43668-3 (Cited on pages 33, 61, 63).

[70] Sébastien Léger, Javier Puertas-Martínez, Karthik Bharadwaj, Rémy Dassonneville, Jovian Delaforce, Farshad Foroughi, Vladimir Milchakov, Luca Planat, Olivier Buisson, Cécile Naud, Wiebke Hasch-Guichard, Serge Florens, Izak Snyman, and Nicolas Roch. "Observation of Quantum Many-Body Effects Due to Zero Point Fluctuations in Superconducting Circuits". In: *Nature Communications* 10.1 (Nov. 2019), p. 5259 (Cited on pages 34, 49, 51).

[71] Roman Kuzmin, Nitish Mehta, Nicholas Grabon, Raymond Mencia, and Vladimir E. Manucharyan. "Superstrong Coupling in Circuit Quantum Electrodynamics". In: *npj Quantum Information* 5.1 (Feb. 2019), pp. 1–6. ISSN: 2056-6387. DOI: 10.1038/s41534-019-0134-2 (Cited on page 34).

[72] A. Murani, N. Bourlet, H. le Sueur, F. Portier, C. Altimiras, D. Esteve, H. Grabert, J. Stockburger, J. Ankerhold, and P. Joyez. "Absence of a Dissipative Quantum Phase Transition in Josephson Junctions". In: *Physical Review X* 10.2 (Apr. 2020), p. 021003. DOI: 10.1103/PhysRevX.10.021003 (Cited on page 34).

[73] Roman Kuzmin, Nitish Mehta, Nicholas Grabon, Raymond A. Mencia, Amir Burshtein, Moshe Goldstein, and Vladimir E. Manucharyan. "Observation of the Schmid–Bulgadaev Dissipative Quantum Phase Transition". In: *Nature Physics* (Dec. 2024), pp. 1–5. ISSN: 1745-2481. DOI: 10.1038/s41567-024-02695-7 (Cited on page 34).

[74] Gert-Ludwig Ingold and Hermann Grabert. "Effect of Zero Point Phase Fluctuations on Josephson Tunneling". In: *Physical Review Letters* 83.18 (Nov. 1999), pp. 3721–3724. DOI: 10.1103/PhysRevLett.83.3721 (Cited on pages 34, 37).

[75] A. I. Larkin and Yu. N. Ovchinnikov. "Decay of the Supercurrent in Tunnel Junctions". In: *Physical Review B* 28.11 (Dec. 1983), pp. 6281–6285. DOI: 10.1103/PhysRevB.28.6281 (Cited on page 34).

[76] Yu. V. Nazarov. "Bloch Oscillations without Quantum Coherency in Josephson Tunnel Junction". In: *Solid State Communications* 85.7 (Feb. 1993), pp. 613–615. ISSN: 0038-1098. DOI: 10.1016/0038-1098(93)90319-I (Cited on page 35).

[77] Heli Vora, R. L. Kautz, S. W. Nam, and J. Aumentado. "Modeling Bloch Oscillations in Nanoscale Josephson Junctions". In: *Physical Review B* 96.5 (Aug. 2017), p. 054505. ISSN: 2469-9950, 2469-9969. DOI: 10.1103/PhysRevB.96.054505 (Cited on page 37).

[78] D. B. Haviland, L. S. Kuzmin, P. Delsing, and T. Claeson. "Observation of the Coulomb Blockade of Cooper Pair Tunnelling in Single Josephson Junctions". In: *Europhysics Letters* 16.1 (Sept. 1991), p. 103. ISSN: 0295-5075. DOI: 10.1209/0295-5075/16/1/018 (Cited on page 37).

[79] Lukas Grünhaupt, Martin Spiecker, Daria Gusenkova, Nataliya Maleeva, Sebastian T. Skacel, Ivan Takmakov, Francesco Valenti, Patrick Winkel, Hannes Rotzinger, Wolfgang Wernsdorfer, Alexey V. Ustinov, and Ioan M. Pop. "Granular Aluminium as a Superconducting Material for High-Impedance Quantum Circuits". In: *Nature Materials* 18.8 (Aug. 2019), pp. 816–819. ISSN: 1476-4660. DOI: 10.1038/s41563-019-0350-3 (Cited on page 37).

[80] Gianluca Aiello. "Quantum Dynamics of a High Impedance Microwave Cavity Strongly Coupled to a Josephson Junction". Theses. Université Paris-Saclay, Dec. 2020 (Cited on pages 37, 65, 85).

[81] Rais S. Shaikhaidarov, Kyung Ho Kim, Jacob W. Dunstan, Ilya V. Antonov, Sven Linzen, Mario Ziegler, Dmitry S. Golubev, Vladimir N. Antonov, Evgeni V. Il'ichev, and Oleg V. Astafiev. "Quantized Current Steps Due to the a.c. Coherent Quantum Phase-Slip Effect". In: *Nature* 608.7921 (Aug. 2022), pp. 45–49. ISSN: 1476-4687. DOI: 10.1038/s41586-022-04947-z (Cited on page 37).

[82] Silvia Corlevi, Wiebke Guichard, Frank WJ Hekking, and David B Haviland. "Phase-Charge Duality of a Josephson Junction in a Fluctuating Electromagnetic Environment". In: *Physical Review Letters* 97.9 (2006), p. 096802 (Cited on page 37).

[83] Nicholas A. Masluk, Ioan M. Pop, Archana Kamal, Zlatko K. Minev, and Michel H. Devoret. "Microwave Characterization of Josephson Junction Arrays: Implementing a Low Loss Superinductance". In: *Physical Review Letters* 109.13 (Sept. 2012), p. 137002. DOI: 10.1103/PhysRevLett.109.137002 (Cited on page 37).

[84] Javier Puertas Martínez, Sébastien Léger, Nicolas Gheeraert, Rémy Dassonneville, Luca Planat, Farshad Foroughi, Yuriy Krupko, Olivier Buisson, Cécile Naud, Wiebke Hasch-Guichard, Serge Florens, Izak Snyman, and Nicolas Roch. "A Tunable Josephson Platform to Explore Many-Body Quantum Optics in Circuit-QED". In: *npj Quantum Information* 5.1 (Feb. 2019), pp. 1–8. ISSN: 2056-6387. DOI: 10.1038/s41534-018-0104-0 (Cited on page 37).

[85] David M Pozar. *Microwave Engineering: Theory and Techniques*. John wiley & sons, 2021 (Cited on pages 41, 43).

[86] T. Giamarchi and H. J. Schulz. "Anderson Localization and Interactions in One-Dimensional Metals". In: *Physical Review B* 37.1 (Jan. 1988), pp. 325–340. DOI: 10.1103/PhysRevB.37.325 (Cited on page 44).

[87] R. M. Bradley and S. Doniach. "Quantum Fluctuations in Chains of Josephson Junctions". In: *Physical Review B* 30.3 (Aug. 1984), pp. 1138–1147. DOI: 10.1103/PhysRevB.30.1138 (Cited on page 44).

[88] SE Korshunov. "Effect of Dissipation on the Low-Temperature Properties of a Tunnel-Junction Chain". In: *Zhurnal Éksperimentalnoi i Teoreticheskoi Fiziki* 95 (1989), pp. 1058–1075 (Cited on page 44).

[89] M-S. Choi, J. Yi, M. Y. Choi, J. Choi, and S-I. Lee. "Quantum Phase Transitions in Josephson-junction Chains". In: *Physical Review B* 57.2 (1998), R716 (Cited on page 44).

[90] D. M. Basko, F. Pfeiffer, P. Adamus, M. Holzmann, and F. W. J. Hekking. *Superconductor-Insulator Transition in Josephson Junction Chains by Quantum Monte-Carlo*. Nov. 2019. DOI: 10.48550/arXiv.1911.02817. arXiv: 1911.02817 (Cited on page 44).

[91] David B. Haviland, Karin Andersson, and Peter Ågren. "Superconducting and Insulating Behavior in One-Dimensional Josephson Junction Arrays". In: *Journal of Low Temperature Physics* 118.5 (Mar. 2000), pp. 733–749. ISSN: 1573-7357. DOI: 10.1023/A:1004603814529 (Cited on pages 44, 52).

[92] S. Mukhopadhyay, J. Senior, J. Saez-Mollejo, D. Puglia, M. Zemlicka, J. M. Fink, and A. P. Higginbotham. "Superconductivity from a Melted Insulator in Josephson Junction Arrays". In: *Nature Physics* 19.11 (Nov. 2023), pp. 1630–1635. ISSN: 1745-2481. DOI: 10.1038/s41567-023-02161-w (Cited on page 44).

[93] G. J. Dolan. "Offset Masks for Lift-off Photoprocessing". In: *Applied Physics Letters* 31.5 (Sept. 1977), pp. 337–339. ISSN: 0003-6951. DOI: 10.1063/1.89690 (Cited on page 46).

[94] Sébastien Leger. "Electrodynamique quantique d'une jonction Josephson couplée à un environnement fortement dissipatif". 2021GRALY038. PhD thesis. 2021. URL: http://www.theses.fr/2021GRALY038/document (Cited on pages 46, 73).

[95] Dorian Fraudet. "Conversion spontanée de photons micro-ondes à partir d'une impureté quantique supraconductrice". 2023GRALY107. PhD thesis. 2023. URL: http://www.theses.fr/2023GRALY107 (Cited on page 46).

[96] Sébastien Léger, Théo Sépulcre, Dorian Fraudet, Olivier Buisson, Cécile Naud, Wiebke Hasch-Guichard, Serge Florens, Izak Snyman, Denis M. Basko, and Nicolas Roch. "Revealing the Finite-Frequency Response of a Bosonic Quantum Impurity". In: *SciPost Physics* 14.5 (May 2023), p. 130. ISSN: 2542-4653. DOI: 10.21468/SciPostPhys.14.5.130 (Cited on pages 49, 122).

[97] Vinay Ambegaokar and Alexis Baratoff. "Tunneling between Superconductors". In: *Physical Review Letters* 10.11 (June 1963), p. 486. DOI: 10.1103/PhysRevLett.10.486 (Cited on page 51).

[98] Adem Ergül, David Schaeffer, Magnus Lindblom, David B. Haviland, Jack Lidmar, and Jan Johansson. "Phase Sticking in One-Dimensional Josephson Junction Chains". In: *Physical Review B* 88.10 (Sept. 2013), p. 104501. ISSN: 1098-0121, 1550-235X. DOI: 10.1103/PhysRevB.88.104501. (Visited on 01/17/2022) (Cited on pages 51, 52).

[99] R. Dolata, H. Scherer, A. B. Zorin, and J. Niemeyer. "Single-Charge Devices with Ultrasmall Nb/AlOx/Nb Trilayer Josephson Junctions". In: *Journal of Applied Physics* 97.5 (Mar. 2005), p. 054501. ISSN: 0021-8979, 1089-7550. DOI: 10.1063/1.1855399 (Cited on page 52).

[100] J.-R. Souquet and A. A. Clerk. "Fock-State Stabilization and Emission in Superconducting Circuits Using Dc-Biased Josephson Junctions". In: *Physical Review A* 93.6 (June 2016), p. 060301. DOI: 10.1103/PhysRevA.93.060301 (Cited on page 65).

[101] Howard J Carmichael. *Statistical Methods in Quantum Optics 1: Master Equations and Fokker-Planck Equations*. Springer Science & Business Media, 2013 (Cited on page 70).

[102] Steven H. Simon and Nigel R. Cooper. "Theory of the Josephson Junction Laser". In: *Physical Review Letters* 121.2 (July 2018), p. 027004. ISSN: 0031-9007, 1079-7114. DOI: 10.1103/PhysRevLett.121.027004. eprint: 1708.02435 (cond-mat, physics:quant-ph) (Cited on pages 72, 85).

[103] Sanjay Moudgalya, B Andrei Bernevig, and Nicolas Regnault. "Quantum Many-Body Scars and Hilbert Space Fragmentation: A Review of Exact Results". In: *Reports on Progress in Physics* 85.8 (July 2022), p. 086501. ISSN: 0034-4885. DOI: 10.1088/1361-6633/ac73a0 (Cited on page 72).

[104] Luca Fasolo. "Development of a Superconducting Platform for the Manipulation of Quantum States in the Microwave Regime". PhD thesis. Sept. 2023. (Visited on 03/18/2025) (Cited on page 73).

[105] Fei Chen, Juliang Li, A. D. Armour, E. Brahimi, Joel Stettenheim, A. J. Sirois, R. W. Simmonds, M. P. Blencowe, and A. J. Rimberg. "Realization of a Single-Cooper-pair Josephson Laser". In: *Physical Review B* 90.2 (July 2014), p. 020506. DOI: 10.1103/PhysRevB.90.020506 (Cited on page 85).

[106] M. C. Cassidy, A. Bruno, S. Rubbert, M. Irfan, J. Kammhuber, R. N. Schouten, A. R. Akhmerov, and L. P. Kouwenhoven. "Demonstration of an Ac Josephson Junction Laser". In: *Science* 355.6328 (Mar. 2017), pp. 939–942. DOI: 10.1126/science.aah6640 (Cited on pages 85, 94).

[107] A. D. Armour, B. Kubala, and J. Ankerhold. "Josephson Photonics with a Two-Mode Superconducting Circuit". In: *Physical Review B* 91.18 (May 2015), p. 184508. DOI: 10.1103/PhysRevB.91.184508 (Cited on page 85).

[108] Florian Höhe, Lukas Danner, Ciprian Padurariu, Brecht I C Donvil, Joachim Ankerhold, and Björn Kubala. "Quantum Synchronization in Presence of Shot Noise". In: *New Journal of Physics* 27.2 (Feb. 2025), p. 023039. ISSN: 1367-2630. DOI: 10.1088/1367-2630/adb777 (Cited on page 85).

[109] A. Schenzle and H. Brand. "Fluctuations in Optical Bistable Systems". In: *Optics Communications* 27.3 (Dec. 1978), pp. 485–488. ISSN: 0030-4018. DOI: 10.1016/0030-4018(78)90429-7 (Cited on page 92).

[110] Hyatt M. Gibbs. *Optical Bistability: Controlling Light with Light*. Academic Press, 1985. ISBN: 978-0-12-281940-7 (Cited on page 92).

[111] M. I. Dykman, G. P. Golubev, D. G. Luchinsky, A. L. Velikovich, and S. V. Tsuprikov. "Fluctuational Transitions and Related Phenomena in a Passive All-Optical Bistable System". In: *Physical Review A* 44.4 (Aug. 1991), pp. 2439–2449. DOI: 10.1103/PhysRevA.44.2439 (Cited on page 92).

[112] C.J. Buczek, R.J. Freiberg, and M.L. Skolnick. "Laser Injection Locking". In: *Proceedings of the IEEE* 61.10 (Oct. 1973), pp. 1411–1431. ISSN: 1558-2256. DOI: 10.1109/PROC.1973.9294 (Cited on page 94).

[113] Henrik Bruus and Karsten Flensberg. *Many-Body Quantum Theory in Condensed Matter Physics: An Introduction*. OUP Oxford, 2004 (Cited on page 110).

[114] G. Catelani and D. M. Basko. "Non-Equilibrium Quasiparticles in Superconducting Circuits: Photons vs. Phonons". In: *SciPost Physics* 6.1 (Jan. 2019), p. 013. DOI: 10.21468/SciPostPhys.6.1.013. eprint: 1807.07377 (cond-mat, physics:quant-ph) (Cited on pages 128–130).

[115] M. V. Moody and J. L. Paterson. "Quasiparticle Relaxation Times in Clean Al Films". In: *Physical Review B* 23.1 (Jan. 1981), pp. 133–142. DOI: 10.1103/PhysRevB.23.133 (Cited on page 128).

[116] Leonid Glazman and Gianluigi Catelani. "Bogoliubov Quasiparticles in Superconducting Qubits". In: *SciPost Physics Lecture Notes* (June 2021), p. 031. ISSN: 2590-1990. DOI: 10.21468/SciPostPhysLectNotes.31. (Visited on 03/21/2025) (Cited on page 128).

Appendix A

Linear response of the isolated junction

In this appendix we detail the steps of the calculation for the impedance of an isolated junction that we used in Section 2.2.3. We apply a perturbatively small current $I(t)$ to our junction, which adds a $-I(t)\Phi_0\hat{\varphi}$ term to the Hamiltonian, and look at the variation in voltage $\langle\Delta\hat{V}\rangle$ across the junction. The Kubo formula directly relates these two quantities through [113]

$$\left\langle \Delta\hat{V}(t)\right\rangle = -\frac{i}{\hbar}\int_{-\infty}^{t}\left\langle\left[\hat{V}(t),-\hat{\varphi}(u)\right]\right\rangle \Phi_0 I(u)\,du, \tag{A.1}$$

with all the operators in the Heisenberg picture, determined by the unperturbed Hamiltonian. This can be rewritten, as usual, by using the retarded Green's function $G^{\mathrm{r}}_{V\varphi}(t-u)$

$$\left\langle \Delta\hat{V}(t)\right\rangle = -\frac{1}{2e}\int_{-\infty}^{+\infty} G^{\mathrm{r}}_{V\varphi}(t-u)I(u)\,du, \tag{A.2}$$

$$G^{r}_{V\varphi}(t) = -i\theta(t)\left\langle\left[\hat{V}(t),\hat{\varphi}(0)\right]\right\rangle. \tag{A.3}$$

Here θ represents the Heaviside step function. Taking Eq. (A.2) to Fourier space we directly see that the impedance of our junction is just

$$Z(\omega) = -\frac{1}{2e}G^{\mathrm{r}}_{V\varphi}(\omega). \tag{A.4}$$

Computing this Green's function is easier through its equation of motion obtained by differentiation of Eq. (A.3):

$$\partial_t G^{\mathrm{r}}_{V\varphi}(t) = -i\delta(t)\left\langle\left[\hat{V}(t),\hat{\varphi}(t)\right]\right\rangle + i\theta(t)\left\langle\left[\hat{V}(0),\dot{\hat{\varphi}}(-t)\right]\right\rangle \tag{A.5}$$

$$= -i\delta(t)\left\langle\left[\hat{V}(t),\hat{\varphi}(t)\right]\right\rangle + i\theta(t)\left\langle\left[\hat{V}(t),\frac{1}{\Phi_0}\hat{V}(0)\right]\right\rangle \tag{A.6}$$

$$= -i\delta(t)\left\langle\left[\hat{V},\hat{\varphi}\right]\right\rangle - \frac{1}{\Phi_0}G^{\mathrm{r}}_{VV}(t), \tag{A.7}$$

where we made use of the time translation invariance of our Green's functions to move the time argument around since we are going to average over stationary density

matrices (namely, over an eigenstate or a thermal state). In frequency space we now have

$$i\omega 2eZ(\omega) = -i\left\langle\left[\hat{V},\hat{\varphi}\right]\right\rangle - \frac{1}{\Phi_0}G^{\mathrm{r}}_{VV}(\omega). \tag{A.8}$$

To recover the expression of the main text, we now suppose that the system is in an eigenstate of the first band $|q,0\rangle$. The first term of Eq. (A.8) can readily be calculated using the definitions in Eqs. (2.13) and (2.16)

$$-i\left\langle\left[\hat{V},\hat{\varphi}\right]\right\rangle_{|q,0\rangle} = -2e\partial_q^2\epsilon_0(q) + \frac{1}{e}\sum_{s=1}^{+\infty}\Omega^{0s}(q)\left|\varphi^w_{0s}(q)\right|^2, \tag{A.9}$$

where we use the notations

$$\Omega^{rs}(q) = \epsilon_r(q) - \epsilon_s(q), \tag{A.10}$$

$$\varphi^w_{rs}(q) = \langle q,r|\hat{\varphi}^w|q,s\rangle. \tag{A.11}$$

The second term of Eq. (A.8) is calculated by using the Lehmann representation of $G^{\mathrm{r}}_{VV}(\omega)$

$$G^{\mathrm{r}}_{VV}(\omega) = \sum_{s=1}^{+\infty}\left|\langle q,0|\hat{V}|q,s\rangle\right|^2\left(\frac{1}{\omega+\Omega^{0s}/\hbar+i0^+} - \frac{1}{\omega-\Omega^{0s}/\hbar+i0^+}\right) \tag{A.12}$$

$$= \frac{1}{4e^2}\sum_{s=1}^{+\infty}\left[\Omega^{0s}(q)\right]^2\left|\varphi^w_{0s}(q)\right|^2\left(\frac{1}{\omega+\Omega^{0s}/\hbar+i0^+} - \frac{1}{\omega-\Omega^{0s}/\hbar+i0^+}\right), \tag{A.13}$$

so that, in the end, the impedance of the junction is written as

$$Z(\omega) = \frac{1}{-i\omega}\partial_q^2\epsilon_0(q) - \frac{i}{2e^2}\sum_{s=1}^{+\infty}\Omega^{0s}(q)\left|\varphi^w_{0s}(q)\right|^2\frac{\omega}{\omega^2-(\Omega^{0s}/\hbar)^2}. \tag{A.14}$$

At frequencies well below the first interband transition, $\hbar\omega \ll \Omega^{10}$, we recover the expression of the main text: a capacitor in series with an inductor,

$$Z(\omega) \xrightarrow{\omega\to 0} \frac{1}{-i\omega C_B(q)} - i\omega L_B(q), \tag{A.15}$$

with the definitions[1]

$$C_B(q) = \frac{1}{\partial_q^2\epsilon_0(q)}, \tag{A.16}$$

$$L_B(q) = \frac{\hbar^2}{2e^2}\sum_{s=1}^{+\infty}\frac{\left|\varphi^w_{0s}(q)\right|^2}{\Omega^{s0}(q)}. \tag{A.17}$$

To find the high frequency limit ($\hbar\omega \gg E_J$) of $Z(\omega)$ we make use of $C_J\hat{V} = \hat{Q}$ to compute $\left[\hat{V},\hat{\varphi}\right] = -i/C_J$ from Eq. (A.8) and observe that the Green's function

[1] We swap the indices with $\Omega^{0s} = -\Omega^{s0}$ to absorb the minus sign coming from the denominator in Eq. (2.18).

$G^{\mathrm{r}}_{VV}(\omega)$ decays as $1/\omega^2$. We therefore recover the purely linear capacitive response of the junction at high frequencies

$$Z(\omega) \xrightarrow{\omega\to+\infty} \frac{1}{-i\omega C_J}. \tag{A.18}$$

Additionally, equating $\left[\hat{V},\hat{\varphi}\right] = -i/C_J$ with Eq. (A.9) gives us the useful sum rule

$$C_J\partial_q^2\epsilon_0(q) = 1 - \frac{1}{4E_C}\sum_{s=1}^{+\infty}\Omega^{s0}(q)\left|\varphi^w_{0s}(q)\right|^2. \tag{A.19}$$

Appendix B

Derivation of the quantum Langevin equation

In this appendix we derive the quantum Langevin equation of a junction coupled to an arbitrary external admittance $Y(\omega)$. We essentially follow the procedure described by Gardiner & Zoller [5]. Starting with the full Hamiltonian of the system

$$\hat{\mathcal{H}} = \sum_{m=1}^{M} \left[\frac{1}{2} \left(\hat{p}_m - g_m \hat{\varphi} \right)^2 + \frac{1}{2} \omega_m^2 \hat{x}_m^2 \right] + \hat{\mathcal{H}}_{JJ}, \tag{B.1}$$

where $\hat{\mathcal{H}}_{JJ}$ represents the Hamiltonian of the uncoupled junction, which can be arbitrary, as long as it does not contain any bath operators. We will assume that the bath is large enough, and the coupling weak enough, so that the density matrix of the full system is separable at all times, $\hat{\rho}_{tot} = \hat{\rho}_{JJ} \otimes \hat{\rho}_{env}$. Moreover, we will suppose that the bath is in a thermal state, so that

$$\hat{\rho}_{env} = \frac{1}{\mathcal{Z}} \exp\left(-\frac{\hat{\mathcal{H}}_B}{k_B T} \right), \quad \hat{\mathcal{H}}_B = \sum_{m=1}^{M} \frac{1}{2} \hat{p}_m^2 + \frac{1}{2} \omega_m^2 \hat{x}_m^2 \tag{B.2}$$

With that said, we want to derive some effective equations of motion for the junction's operators and so, we start by writing down the equations for the bath variables,

$$\begin{cases} \dot{\hat{p}}_m = -\omega_m^2 \hat{x}_m, \\ \dot{\hat{x}}_m = \hat{p}_m - g_m \hat{\varphi}. \end{cases} \tag{B.3}$$

We rewrite them in the normal mode basis of the environment by posing $\hat{a}_m = \frac{1}{\sqrt{2\hbar\omega_m}} \left(\omega_m \hat{x}_m + i \hat{p}_m \right)$, yielding

$$\dot{\hat{a}}_m = -i\omega_m \hat{a}_m - g_m \sqrt{\frac{\omega_m}{2\hbar}} \hat{\varphi}. \tag{B.4}$$

We can solve for $\hat{a}_m$ by Laplace transform

$$\hat{a}_m(s) = \frac{1}{s + i\omega_m} \left[\hat{a}_m^0 - g_m \sqrt{\frac{\omega_m}{2\hbar}} \hat{\varphi}(s) \right], \tag{B.5}$$

where $\hat{a}_m^0 = \hat{a}_m(t = 0)$ is the initial condition in the time domain. This also gives us the expression for the Laplace transform of the bath canonical variables. In

particular, for $\hat{x}_m$ this yields

$$\hat{x}_m(s) = \sqrt{\frac{\hbar}{2\omega_m}}\left[\hat{a}_m(s) + \hat{a}_m^\dagger(s)\right] \tag{B.6}$$

$$= \sqrt{\frac{\hbar}{2\omega_m}}\left[\frac{\hat{a}_m^0}{s+i\omega_m} + \frac{\hat{a}_m^{0\dagger}}{s-i\omega_m}\right] - g_m\frac{s}{s^2+\omega_m^2}\hat{\varphi}. \tag{B.7}$$

We then write down the Heisenberg equations of motion for an arbitrary junction operator $\hat{O}$

$$\dot{\hat{O}} = \frac{1}{i\hbar}\left[\hat{O}, \hat{\mathcal{H}}_{JJ}\right] + \frac{1}{2i\hbar}\sum_m \left[\hat{O}, (\hat{p}_m - g_m\hat{\varphi})^2\right] \tag{B.8}$$

$$= \frac{1}{i\hbar}\left[\hat{O}, \hat{\mathcal{H}}_{JJ}\right] - \frac{1}{2i\hbar}\sum_m (\hat{p}_m - g_m\hat{\varphi})\left[\hat{O}, g_m\hat{\varphi}\right] + \left[\hat{O}, g_m\hat{\varphi}\right](\hat{p}_m - g_m\hat{\varphi}) \tag{B.9}$$

$$= \frac{1}{i\hbar}\left[\hat{O}, \hat{\mathcal{H}}_{JJ}\right] - \frac{1}{2i\hbar}\sum_m \left\{\left[\hat{O}, g_m\hat{\varphi}\right], \dot{\hat{x}}_m\right\}_+ \tag{B.10}$$

where we made use of $\left[\hat{O}, \hat{p}_m\right] = 0$ and of Eqs.(B.3). We denoted the anti-commutator with $\{\bullet, \bullet\}_+$. The $\dot{\hat{x}}_m$ term of the right-hand side can be found by multiplying Eq. (B.7) by s and going back to the time domain. Reinjecting, we get the quantum Langevin equation for the operator $\hat{O}$

$$\dot{\hat{O}} = \frac{1}{i\hbar}\left[\hat{O}, \hat{\mathcal{H}}_{JJ}\right] + \frac{1}{2i\hbar}\left\{\left[\hat{O}, \hat{\varphi}\right], \int_0^t y(t-u)\dot{\hat{\varphi}}(u)\,du + y(t)\hat{\varphi}(0) + \tilde{\chi}(t)\right\}_+, \tag{B.11}$$

with the y function defined as

$$y(t) = \sum_m g_m^2 \cos(\omega_m t). \tag{B.12}$$

The variable $\tilde{\chi}(t)$ is given by $\hat{a}_m^0$ operators:

$$\tilde{\chi}(t) = i\sum_m g_m\sqrt{\frac{\hbar\omega_m}{2}}\left(\hat{a}_m^{0\dagger}e^{i\omega_m t} - \hat{a}_m^0 e^{-i\omega_m t}\right). \tag{B.13}$$

Since the bath is considered to be in a thermal state at all times we have

$$\langle\hat{a}_m^0\rangle = 0, \tag{B.14}$$

$$\langle\hat{a}_m^{0\dagger}\hat{a}_n^0\rangle = \frac{\delta_{mn}}{e^{\hbar\omega_m/k_BT} - 1}, \tag{B.15}$$

$$\langle\hat{a}_m^0\hat{a}_n^0\rangle = 0, \tag{B.16}$$

where the averages are performed by tracing over the bath density matrix $\hat{\rho}_{env}$ only. Thus, we formally replace $\tilde{\chi}(t)$ with a centered Gaussian random noise whose moments are[1]

$$\langle\tilde{\chi}(t)\rangle = 0, \tag{B.17}$$

$$\langle\tilde{\chi}(t)\tilde{\chi}(0)\rangle = \sum_m g_m^2\hbar\omega_m\left[\coth\left(\frac{\hbar\omega_m}{2k_BT}\right)\cos\omega_m t - i\sin\omega_m t\right]. \tag{B.18}$$

[1]This replacement is where we make use of the separability of the density matrix at all times and trace out the bath variables. Everything before that is just formal manipulations of the equations of motion.

Furthermore, we can identify $\tilde{\chi}(t)$ with the fluctuations coming from the admittance $Y(\omega)$, and by using the fluctuation-dissipation relations we fix g_m to be [35, 58]

$$g_m = \frac{\hbar}{2e}\sqrt{\frac{2\mathrm{Re}\left[Y(\omega_m)\right]\Delta\omega_m}{\pi}}, \tag{B.19}$$

with $\Delta\omega_m$ corresponding to the frequency spacing of the bath oscillators at ω_m, usually taken to be constant. This means, in the continuum limit, $y(t)$ essentially becomes

$$y(t) \xrightarrow{M\to\infty} \left(\frac{\hbar}{2e}\right)^2 \frac{2}{\pi}\int_0^{+\infty} \mathrm{Re}\left[Y(\omega)\right]\cos(\omega t)\, d\omega \tag{B.20}$$

The $y(t)\hat{\varphi}(0)$ term in Eq.(B.11) can be neglected since it decays for large t as long as $Y(\omega \to 0)$ is finite[2].

As a final note, we give the Langevin equation for the case of a purely ohmic environment $Y(\omega) = 1/R$. We have

$$y(t) = \left(\frac{\hbar}{2e}\right)^2 \frac{2}{R}\delta(t), \tag{B.21}$$

and so Eq.(B.11) is rewritten as

$$\dot{\hat{O}} = \frac{1}{i\hbar}\left[\hat{O}, \hat{\mathcal{H}}_{JJ}\right] + \frac{1}{2i\hbar}\left\{\left[\hat{O}, \hat{\varphi}\right], \left(\frac{\hbar}{2e}\right)^2 \frac{1}{R}\dot{\hat{\varphi}} + \tilde{\chi}(t)\right\}_+ . \tag{B.22}$$

[2]If the admittance diverges at zero frequency it usually means that there is some inductive shunt in the environment. In this case, one has to separate the inductive term and put it in the junction's Hamiltonian.

Appendix C

Thévenin-Norton transformation

Here we quickly derive the Thévenin-Norton transformation for our dissipative quantum system, that is a junction coupled to an admittance $Y(\omega)$. We start from the current bias configuration, so that the total Hamiltonian is written as

$$\hat{\mathcal{H}} = \sum_m \frac{1}{2}\left(\hat{p}_m - g_m\hat{\varphi}\right)^2 + \frac{1}{2}\omega_m^2\hat{x}_m^2 + 4E_C\hat{n} - E_J\cos\hat{\varphi} - \Phi_0\, I(t)\hat{\varphi} \tag{C.1}$$

The transformation is easier to achieve at the level of the equations of motion for the canonical variables of the subsystem[1]. As such, we write down Eq. (B.11) for $\hat{n}$ and $\hat{\varphi}$:

$$\begin{cases} 2e\,\dot{\hat{n}} = -I_C\sin\hat{\varphi} - \Phi_0\, y * \dot{\hat{\varphi}} + I(t) + \hat{\chi}(t) \\ \hbar\,\dot{\hat{\varphi}} = 8E_C\hat{n} \end{cases}, \tag{C.2}$$

where the function y is the Fourier transform of the admittance, and the symbol $*$ represents the convolution operation. The transformation is done by translating $\dot{\varphi}$ with

$$\dot{\hat{\varphi}}' = \dot{\hat{\varphi}} - \frac{1}{\Phi_0} z * I(t) \tag{C.3}$$

where z is the Fourier transform of $Z = 1/Y$ such that $z * y = \mathbb{1}$. The equations of motion of the system are thus shifted to

$$\begin{cases} 2e\,\dot{\hat{n}} = -I_C\sin\left[\hat{\varphi}' + \int^t z * I(u)\,du\right] - \Phi_0\, y * \dot{\hat{\varphi}} + \hat{\chi}(t) \\ \hbar\,\dot{\hat{\varphi}} = 8E_C\hat{n} + 2e\, z * I(t) \end{cases}, \tag{C.4}$$

which are exactly the equations of motion of the same circuit under a voltage bias $V(t)$ given by

$$V(t) = z * I(t) \iff V(\omega) = Z(\omega)I(\omega). \tag{C.5}$$

[1] Although it is probably possible to achieve it at the Hamiltonian level by jumping back and forth between interaction representations.

Appendix D

Fabrication recipe

In this appendix we expose the detail of the nano-fabrication recipe used to make all the sample during the thesis. More specifically we expose the full recipe to make the sample used in Chapter 3. The recipe for the samples of Chapter 4 and 5 is identical apart from the steps related the conductive resist as we switched to pure silicon wafer for these samples. The steps in question are the spin-coating of Electra-92 and its development in water. In table D.1 we detail the fabrication steps of the focus markers we use on our chip to focus during the electronic lithography for the junctions. The details of the fabrication of Josephson circuits is contained in table D.2.

Step	Details
Resist stack	–Pre-bake at 180° for 2 min –Spin-coat PMMA 3% AR-P 679 (950K) at 4000 rpm for 30 s with 4000 rpm/s –Bake at 180° for 5 min –Spin-coat Electra-92 AR-PC 5090 at 3500 rpm for 60 s with 3500 rpm/s
Lithography	–Beam current of 15 nA –Dose of 10 C/cm^2
Development	–Electra, water at room temp. for 60 s –PMMA, MIBK:IPA 1:3 for 60 s and IPA for 30 s
Evaporation	–5 nm of Ti at 0.1 nm/s –50 nm of Au at 0.1 nm/s
Lift-off	–Leave in NMP for 5 h at 80° –Ultrasonics for 30 s

Table D.1: Fabrication steps for the creating the gold focus markers used in the lithography of junctions.

Step	Details
Resist stack	–Pre-bake at 200° for 2 min –Spin-coat PMMA/MAA 9% AR-P 617.14 diluted 9:5 in AR-P 600.07 at 3500 rpm for 30 s with 3500 rpm/s –Bake at 200° for 10 min –Spin-coat PMMA 4% AR-P 679.04 at 5000 rpm for 30 s with 5000 rpm/s –Bake at 180° for 5 min –Spin-coat Electra-92 AR-PC 5090 at 3500 rpm for 60 s with 3500 rpm/s –Bake at 90° for 2 min
Lithography	**Large structures: pads, feedlines, ...** –Beam current of 15 nA –Dose of 12 C/cm^2 **Small structures: junctions** –Beam current of 1 nA –Undercut layer dose of 3 C/cm^2 –Full development dose of 10 C/cm^2
Development	–Electra, water at room temp. for 60 s –Bilayer stack, MIBK:IPA 1:3 for 60 s and IPA for 30 s
Evaporation	–RIE cleaning with O_2 plasma at 10 W for 15 s –Overnight pumping –20 nm of Al at 0.1 nm/s at an angle of +35° –Oxidation for $1-10$ min at $1-10$ mbar, depending on the design –50 nm of Al at 0.1 nm/s at an angle of -35°
Lift-off	–Leave in NMP for 5 h at 80° –Ultrasonics for 30 s
Dicing and back-plating	–Spin-coat (front face): photoresist S1818 at 4000 rpm for 30 s with 4000 rpm/s –Evaporate 10 nm of Ti at 0.05 nm/s on the back of the wafer –Evaporate 200 nm of Cu at 0.5 nm/s on the back of the wafer –Dice into 8x8 mm chips –Remove the protective resist in Acetone

Table D.2: Fabrication steps for the creating the Josephson junctions circuits.

Appendix E

Frequency shift of the odd modes

Here we rapidly present the derivation of the frequency shift of the odd modes relative to the even ones. We do this by looking at the resonant condition of the total circuit (TL+JJ+TL). Let us neglect losses so that the impedance seen at the junction's node

$$Z(\omega) = \frac{1}{\frac{1}{Z_{\mathrm{tl}}} + \frac{1}{Z_{JJ}+Z_{\mathrm{tl}}}} \tag{E.1}$$

has to diverge on resonance for a real ω. We denoted the impedance of the small junction with Z_{JJ}. The impedance Z_{tl} of the (identical) lines is the one seen from the position of the small junction. First, we directly see that the condition $Z(\omega) \to \infty$ is satisfied if $Z_{\mathrm{tl}} \to \infty$, recovering the even modes. The odd modes are found by equating the denominator of Eq. (E.1) to 0 which gives the usual transverse resonant condition

$$2Z_{\mathrm{tl}}(\omega) = -Z_{JJ}(\omega). \tag{E.2}$$

If Z_{JJ} is large the frequency shift will be small, and we can expand Z_{tl} around an even mode ω_m,

$$Z_{\mathrm{tl}} \approx q_m \frac{2i\omega}{\omega^2 - \omega_m^2}, \tag{E.3}$$

keeping only a single pair of poles ($\pm iq_m$ is the residue of Z_{tl} at these poles). Thus, if $Z_{JJ} = -i\omega L$, we have that

$$\omega = \sqrt{\omega_m^2 + \frac{4q_m}{L}} > \omega_m, \tag{E.4}$$

using Eq. (E.2), while if $Z_{JJ} = -1/i\omega C$, we have

$$\omega = \frac{1}{\sqrt{1 + 4q_m C}}\omega_m < \omega_m, \tag{E.5}$$

yielding a negative shift. In our case, since the losses are small, Z_{tl} is given by application of Eq. (2.114) with $\gamma = ik(\omega)$:

$$Z_{\mathrm{tl}}(\omega) = Z_0(\omega)\,\frac{1 - e^{-2ikL}}{1 + e^{-2ikL}}, \tag{E.6}$$

where we put $r_2 = -1$, approximating the $50\,\Omega$ termination by a short since Z_0 is much larger. Here the length L corresponds to the length of one line (so essentially half the length of the sample), $k(\omega)$ is given by Eq. (2.116), and $Z_0(\omega)$ by

Eq. (2.117). The resonant frequencies of the even modes correspond to $e^{-2ikL} = -1$ or equivalently

$$k(\omega_m) = \frac{\pi}{2L}(2m+1)\,. \tag{E.7}$$

The residue of $Z_{\rm tl}$ can be found by expanding the denominator of Eq. (E.6) near the zero ω_m, yielding

$$q_m \approx \frac{Z_0(\omega_m)}{L}\frac{d\omega}{dk}\Big|_{k=k(\omega_m)}. \tag{E.8}$$

If L is large we can approximate $d\omega/dk$ by the discrete difference $(\omega_{m+1}-\omega_m)L/\pi$ by Taylor expanding $k(\omega_{m+1})$, and arrive at the more convenient form

$$q_m \approx \frac{Z_0(\omega_m)}{\pi}(\omega_{m+1}-\omega_m)\,, \tag{E.9}$$

which is what we use experimentally to quickly evaluate C or L.

Appendix F

Derivation of the couplings Λ_m

In this appendix we derive Eq. (4.2) used in the main text. It can be found by computing the finite-size impedance $\mathcal{Z}_t(\omega)$ seen at the small junction node (where ϕ is placed on Figure 4.1). For the sake of simplicity, we neglect losses and approximate the $50\,\Omega$ boundary as a short. From the linear response of Hamiltonian (4.1) we obtain

$$2\pi\frac{\mathcal{Z}_t(\omega)}{R_Q} = \sum_m \omega_m \Lambda_m^2 \frac{i2\omega}{\omega^2 - \omega_m^2}. \tag{F.1}$$

By computing the impedance of the finite chain of length L (see Eq. (2.114)), shunted by C_J, we find

$$\mathcal{Z}_t(\omega) = \frac{1}{-i\omega C_J + \frac{1}{Z_{t1}(\omega)}} = \frac{iZ_0(\omega)}{\omega Z_0(\omega) C_J + \cot[k(\omega)L]}. \tag{F.2}$$

Equation (F.1) tells us that Λ_m can be found by computing the residue of $\mathcal{Z}_t$ at $\pm\omega_m$, giving us

$$i\Lambda_m^2 \omega_m \frac{R_Q}{2\pi} = \operatorname{Res} \mathcal{Z}_t(\omega_m). \tag{F.3}$$

By definition, the denominator of Eq. (F.2) vanishes on resonance, so that the residue of $\mathcal{Z}_t$ can be found by expanding $\cot kL$ close to ω_m, yielding [we denote $k_m = k(\omega_m)$]

$$\begin{aligned}\operatorname{Res} \mathcal{Z}_t(\omega_m) =& \frac{1}{L}\frac{d\omega}{dk}\Big|_{k_m} \frac{iZ_0(\omega_m)}{1 + \cot^2 k_m L} \\ =& \frac{1}{L}\frac{d\omega}{dk}\Big|_{k_m} \frac{iZ_0(\omega_m)}{1 + [\omega_m Z_0(\omega_m) C_J]^2}.\end{aligned} \tag{F.4}$$

We can approximate $d\omega/dk$ by the discrete difference $\Delta\omega_m L/\pi$. Then, by equating this with Eq. (F.3), we finally recover the expression given in the main text:

$$\Lambda_m^2 = 2\frac{\Delta\omega_m}{\omega_m}\frac{\operatorname{Re} Z_t(\omega_m)}{R_Q}, \tag{F.5}$$

with $Z_t(\omega) = 1/[-i\omega C_J + 1/Z_0(\omega)]$.

Appendix G

Quantum master equation for the photonic Joule effect

In this Appendix we derive a master equation for the mode reduced density matrix $\hat{\rho}_m$ and use to it rederive the kinetic equation (4.16) of the main text. In the interaction representation the full density matrix $\hat{\rho}$ obeys

$$\dot{\hat{\rho}}(t) = \frac{1}{i\hbar}\left[\hat{\mathcal{H}}_{\text{int}}(t), \hat{\rho}(t)\right], \tag{G.1}$$

with the interaction Hamiltonian given by

$$\hat{\mathcal{H}}_{\text{int}}(t) = -E_J \cos\left[\frac{2eV}{\hbar}t - \hat{\phi}(t)\right], \tag{G.2}$$

$$\hat{\phi}(t) = \sum_m \hat{\phi}_m(t) = \sum_m \Lambda_m \left(\hat{a}_m e^{-i\omega_m t} + \hat{a}_m^\dagger e^{i\omega_m t}\right). \tag{G.3}$$

As stated in the main text we will suppose the full density matrix of the system separable so that, at all times, $\hat{\rho} = \hat{\rho}_1 \otimes \hat{\rho}_2 \otimes \cdots \otimes \hat{\rho}_N$. We want to derive a master equation for each reduced density matrix $\hat{\rho}_m$ by treating the all the other modes as a bath. Following Gardiner & Zoller [5], we go to second order in $\hat{\mathcal{H}}_{\text{int}}$ in Eq. (G.1) and trace out all the other modes but the m-th mode (we denote this partial trace by $\text{Tr}_{\bar{m}}\{\bullet\}$), yielding

$$\dot{\hat{\rho}}_m(t) = \frac{1}{i\hbar}\,\text{Tr}_{\bar{m}}\left\{\left[\hat{\mathcal{H}}_{\text{int}}(t),\, \hat{\rho}(t_0)\right]\right\} - \frac{1}{\hbar^2}\int_{t_0}^{t} \text{Tr}_{\bar{m}}\left\{\left[\hat{\mathcal{H}}_{\text{int}}(t),\, \left[\hat{\mathcal{H}}_{\text{int}}(u),\, \hat{\rho}(u)\right]\right]\right\} du. \tag{G.4}$$

As in the main text, we assume that each mode is in a thermal state. Therefore, the first term on the right-hand side vanishes in the thermodynamic limit (additionally it will oscillate at a high frequency $2eV/\hbar$). Indeed, since we suppose a Gaussian density matrix, we have the bound [96]

$$\langle \hat{\mathcal{H}}_{\text{int}} \rangle \leq E_J e^{-\frac{1}{2}\sum_m^N \Lambda_m^2}, \tag{G.5}$$

with the sum in the exponent of the right-hand side diverging as $\ln(N\sqrt{C_g/C})$ in the limit $N \to +\infty$. We also suppose that the correlation times of the bath are going to be much shorter than the inner dynamics of the mode, allowing us to simplify the second term [5]

$$\dot{\hat{\rho}}_m(t) = -\frac{1}{\hbar^2}\int_0^{+\infty} \text{Tr}_{\bar{m}}\left\{\left[\hat{\mathcal{H}}_{\text{int}}(t),\, \left[\hat{\mathcal{H}}_{\text{int}}(t-\tau),\, \hat{\rho}(t)\right]\right]\right\} d\tau. \tag{G.6}$$

Moreover, if the non-linearity is weak we can perform the usual rotating wave approximation (RWA) and retain only the terms which do not oscillate (i.e. which only depend on τ and not t) after expanding the double commutator. In the main text we took the thermodynamic limit, allowing us to expand perturbatively in Λ_m. Here, we perform the same approximation, giving us

$$\hat{\mathcal{H}}_{\text{int}}(t) \approx -\frac{E_J}{2}\left[1 + i\hat{\phi}_m(t) - \frac{1}{2}\hat{\phi}_m^2(t)\right] e^{i\hat{\phi}(t) - i2eVt/\hbar} + \text{h.c.} \tag{G.7}$$

Expanding the double correlator in Eq. (G.6) and rearranging the terms yields

$$\begin{aligned}\dot{\hat{\rho}}_m = {} & 2\,\text{Re}\,[z(-\omega_m)]\,\hat{a}_m\hat{\rho}_m\hat{a}_m^\dagger + 2\,\text{Re}\,[z(+\omega_m)]\,\hat{a}_m^\dagger\hat{\rho}_m\hat{a}_m \\ & - [z(-\omega_m) - i\,\text{Im}\,z(0)]\,\hat{a}_m^\dagger\hat{a}_m\hat{\rho}_m - \hat{\rho}_m\hat{a}_m^\dagger\hat{a}_m\,[z^*(-\omega_m) + i\,\text{Im}\,z(0)] \\ & - [z(+\omega_m) - i\,\text{Im}\,z(0)]\,\hat{a}_m\hat{a}_m^\dagger\hat{\rho}_m - \hat{\rho}_m\hat{a}_m\hat{a}_m^\dagger\,[z^*(+\omega_m) + i\,\text{Im}\,z(0)]\,,\end{aligned} \tag{G.8}$$

with the complex quantity $z(\omega)$ defined by

$$z(\omega) = \frac{1}{2}\left(\frac{E_J\Lambda_m}{\hbar}\right)^2 \int_0^{+\infty} e^{J(\tau)}\cos\left(\frac{2eV}{\hbar}\tau\right) e^{-i\omega\tau}\,d\tau. \tag{G.9}$$

In particular, using the definitions of Eqs. (2.74) and (2.78) from Chapter 2, we have

$$\text{Re}\,z(\omega_m) = \frac{\Lambda_m^2}{8e^2}S_{II}(\omega_m), \tag{G.10}$$

$$\text{Im}\,[z(\omega_m) + z(-\omega_m) - 2z(0)] = \frac{\Lambda_m^2\omega_m R_Q}{4\pi}\,\text{Im}\,Y_J(\omega_m). \tag{G.11}$$

Thus, using the property $2\hat{A}\hat{B} = [\hat{A},\hat{B}] + \{\hat{A},\hat{B}\}_+$, Eq. G.8 can be recast in the usual Linblad form

$$\begin{aligned}\dot{\hat{\rho}}_m = {} & -i\frac{\Lambda_m^2\omega_m}{4\pi R_Q}\,\text{Im}\,Y_J(\omega_m)\,[\hat{a}_m^\dagger\hat{a}_m,\,\hat{\rho}_m] \\ & + \frac{1}{2}\Gamma_m^-\left(2\hat{a}_m\hat{\rho}_m\hat{a}_m^\dagger - \hat{a}_m^\dagger\hat{a}_m\hat{\rho}_m - \hat{\rho}_m\hat{a}_m^\dagger\hat{a}_m\right) \\ & + \frac{1}{2}\Gamma_m^+\left(2\hat{a}_m^\dagger\hat{\rho}_m\hat{a}_m - \hat{a}_m\hat{a}_m^\dagger\hat{\rho}_m - \hat{\rho}_m\hat{a}_m\hat{a}_m^\dagger\right),\end{aligned} \tag{G.12}$$

with the rates $\Gamma_m^\pm$ given by the same definition as in the main text

$$\Gamma_m^\pm = \frac{\Lambda_m^2}{4e^2}S_{II}(\pm\omega_m) = \frac{\pi\Lambda_m^2}{2\hbar}E_J^2\,[P(2eV \mp \omega_m) + P(-2eV \mp \omega_m)]\,. \tag{G.13}$$

The first term of Eq. (G.15) is the frequency shift of the mode due to the impedance of the Josephson term, akin to a Lamb shift or Stark shift [5]. We ignored this term in the main text as it is small at high temperatures. The second and third terms are the usual super-operators for decay and excitation. The losses κ_m can be incorporated by adding the interaction with the external circuitry in $\hat{\mathcal{H}}_{\text{int}}$:

$$\hat{\mathcal{H}}'_{\text{int}}(t) = \hat{\mathcal{H}}_{\text{int}}(t) + \sum_m \int_0^{+\infty} \hbar\sqrt{\frac{\kappa_m}{2\pi}}\left(\hat{a}_m e^{-i\omega_m t} + \hat{a}_m^\dagger e^{i\omega_m t}\right)\left(\hat{b}_\omega e^{-i\omega t} + \hat{b}_\omega^\dagger e^{i\omega t}\right) d\omega. \tag{G.14}$$

We then expand the double commutator of Eq. (G.6) and retain only the RWA terms. Since the computation occurs in parallel as the one for the rates $\Gamma^{\pm}$, we just get an additional dissipator (we suppose that the external circuitry is at zero temperature):

$$\begin{aligned}\dot{\hat{\rho}}_m = & -i\frac{\Lambda_m^2\omega_m}{4\pi R_Q}\,\mathrm{Im}\,Y_J(\omega_m)\left[\hat{a}_m^\dagger\hat{a}_m,\,\hat{\rho}_m\right] \\ & + \frac{1}{2}\left(\Gamma_m^- + \kappa_m\right)\left(2\hat{a}_m\hat{\rho}_m\hat{a}_m^\dagger - \hat{a}_m^\dagger\hat{a}_m\hat{\rho}_m - \hat{\rho}_m\hat{a}_m^\dagger\hat{a}_m\right) \\ & + \frac{1}{2}\Gamma_m^+\left(2\hat{a}_m^\dagger\hat{\rho}_m\hat{a}_m - \hat{a}_m\hat{a}_m^\dagger\hat{\rho}_m - \hat{\rho}_m\hat{a}_m\hat{a}_m^\dagger\right), \end{aligned} \tag{G.15}$$

Multiplying by $\hat{a}_m^\dagger\hat{a}_m$ and taking the trace recovers the kinetic equation (4.16) of the main text.

Appendix H

Classical master equation from chaotic dynamics

In this appendix we derive the classical master equation used in Subsection 4.2.5. As stated in the main text, the calculations are sensibly the same as for the quantum master equation (done in the previous Appendix G), with the replacement of the commutator by the Poisson bracket. The losses κ_m do not impact the derivation, so we ignore them for now and add them at the very end. Therefore, the Hamiltonian generating the classical dynamics is given by

$$\mathcal{H} = \mathcal{H}_0 + \mathcal{H}_{\text{int}} = \sum_m \hbar\omega_m \alpha_m^* \alpha_m - E_J \cos\left[\frac{2e}{\hbar} Vt - \phi\right], \tag{H.1}$$

$$\phi = \sum_k \phi_k = \sum_k \Lambda_k \left(\alpha_k + \alpha_k^*\right), \tag{H.2}$$

and the Poisson bracket is

$$\{A, B\} = \sum_m \frac{\partial A}{\partial \alpha_m}\frac{\partial B}{\partial \alpha_m^*} - \frac{\partial A}{\partial \alpha_m^*}\frac{\partial B}{\partial \alpha_m}. \tag{H.3}$$

Motivated by the choatic dynamics, the full phase-space distribution is assumed to be Gaussian centered, and separable $\rho(\alpha_0, \alpha_0^*, \ldots, \alpha_N, \alpha_N^*) = \prod_m \rho_m(\alpha_m, \alpha_m^*)$. It obeys Liouville's equation[1]:

$$\dot{\rho} = \frac{1}{i\hbar}\{\mathcal{H}, \rho\}. \tag{H.4}$$

As in the previous Appendix G, we move to the interaction picture, here given by the canonical transformation to the rotating frame $\alpha_m(t) \to \alpha_m(t)e^{-i\omega_m t}$, and go to second order in $\mathcal{H}_{\text{int}}$[2]:

$$\dot{\rho} = -\frac{1}{\hbar^2}\int_{t_0}^{t} \{\mathcal{H}_{\text{int}}(t), \{\mathcal{H}_{\text{int}}(u), \rho(u)\}\}\, du. \tag{H.5}$$

The equation for ρ_m is obtained by integrating over the other degrees of freedom $\alpha_{k\neq m}$. This is algebraically equivalent to taking a partial trace, so we denote this operation by $\text{Tr}_{\bar{m}}\{\bullet\}$, like for the quantum case. We also assume that the correlations

[1] The $\hbar$ here is arbitrary and arises from the normalization of α_m.

[2] We do not write the first order term as it will vanish in the thermodynamic limit, see Eq. (G.5) in the previous Appendix.

times of the bath, composed by the other modes, are short compared to the inner dynamics of the m-th mode, in its rotating frame. This allows us to extend the integration bound to infinity and replace $\rho(u)$ with $\rho(t)$ on the right-hand side [5], yielding

$$\dot{\rho}_m = -\frac{1}{\hbar^2}\int_0^{+\infty} \mathrm{Tr}_{\bar{m}}\left[\{\mathcal{H}_{\mathrm{int}}(t), \{\mathcal{H}_{\mathrm{int}}(t-\tau), \rho(t)\}\}\right] d\tau. \tag{H.6}$$

As in the derivation of the kinetic equation in the main text, we expand the interaction Hamiltonian to second order in Λ_m, yielding

$$\mathcal{H}_{\mathrm{int}}(t) \approx -\frac{E_J}{2}\left[1 + i\phi_m(t) - \frac{1}{2}\phi_m^2(t)\right] e^{i\phi(t) - i2eVt/\hbar} + \mathrm{c.c.} \tag{H.7}$$

Then, keeping only the terms which do not rotate in the double bracket of Eq. H.6, we get,

$$\begin{aligned}\dot{\rho}_m = u(\omega_m)\frac{\partial^2}{\partial\alpha_m^*\partial\alpha_m}\rho_m + \left[v(-\omega_m)\frac{\partial}{\partial\alpha_m}\alpha_m - v(\omega_m)\frac{\partial}{\partial\alpha_m^*}\alpha_m^*\right]\rho_m \\ - v(0)\left(\alpha_m\frac{\partial}{\partial\alpha_m} - \alpha_m^*\frac{\partial}{\partial\alpha_m^*}\right)\rho_m\end{aligned} \tag{H.8}$$

with the complex quantities defined as

$$u(\omega) = \frac{1}{2}\left(\frac{E_J\Lambda_m}{\hbar}\right)^2 \int_{-\infty}^{+\infty} e^{J_{\mathrm{Cl}}(\tau)}\cos\left(\frac{2eV}{\hbar}\tau\right) e^{-i\omega\tau}\, d\tau, \tag{H.9}$$

$$v(\omega) = \frac{1}{2}\left(\frac{E_J\Lambda_m}{\hbar}\right)^2 \int_{0}^{+\infty} \left\langle \left\{e^{i\phi(\tau)}, e^{-i\phi(0)}\right\}\right\rangle_{\bar{m}} \cos\left(\frac{2eV}{\hbar}\tau\right) e^{-i\omega\tau}\, d\tau, \tag{H.10}$$

where $\langle\bullet\rangle_{\bar{m}}$ denotes the average over the bath variables, that is $\mathrm{Tr}_{\bar{m}}(\bullet\rho)$. The phase-phase correlator $J_{\mathrm{Cl}}(\tau) = \langle[\phi(\tau) - \phi(0)]\phi(0)\rangle$ is now purely real and given by

$$J_{\mathrm{Cl}}(t) = \sum_k 2\Lambda_k^2\langle|\alpha_k|^2\rangle\left(\cos\omega_k t - 1\right), \tag{H.11}$$

where we overcount the contribution of the m-th mode as in the main text.

We made use of several properties to derive and rearrange the terms of Eq. (H.8). To simplify expressions involving Poisson brackets with the bath functions, we use that, for any[3] phase-space functions A and B,

$$\mathrm{Tr}\left(\{A, B\}\right) = 0. \tag{H.12}$$

This also implies

$$\mathrm{Tr}\left(A\{B, C\}\right) = \mathrm{Tr}\left(\{B, AC\} - \{B, A\}C\right) = \mathrm{Tr}\left(\{A, B\}C\right), \tag{H.13}$$

which is what we use to obtain the terms $v(\omega)$ in Eq. (H.8), along with the property $J_{\mathrm{Cl}}(\tau) = J_{\mathrm{Cl}}(-\tau)$.

[3] Technically this is only true if A or B are sufficiently regular at infinity, but since we deal with Gaussian distributions this condition is always fulfilled.

The coefficients in Eq. (H.8) can be related to the fluctuations and the impedance of the junction respectively. The u coefficient is simply the classical current noise spectral density, as can be read from Eq. (2.74)

$$u(\omega_m) = \frac{\Lambda_m^2}{4e^2} S_{II}(\omega_m). \tag{H.14}$$

By computing the linear response of the junction in a similar fashion as for the quantum case (see Section 2.3.4 in Chapter 2) we get that the admittance of the junction is given by

$$Y_J(\omega) = \left(\frac{2eE_J}{\hbar}\right)^2 \frac{1}{2\hbar\omega} \int_0^{+\infty} \left\langle \left\{ e^{i\phi(\tau)}, e^{-i\phi(0)} \right\} \right\rangle \left(e^{i\omega\tau} - 1\right) \cos\left(\frac{2e}{\hbar} V\tau\right) d\tau. \tag{H.15}$$

Therefore, the v coefficient is related to Y_J through

$$v(-\omega_m) - v(0) = \frac{\omega_m \Lambda_m^2 R_Q}{2\pi} Y_J(\omega_m), \tag{H.16}$$

which also tell us that $v(\omega) = -v^*(-\omega)$. Using these we can simplify Eq. (H.8) into the form used in the main text,

$$\dot{\rho}_m = \frac{\Lambda_m^2}{4e^2} S_{II}(\omega_m) \frac{\partial^2}{\partial\alpha_m^* \partial\alpha_m} \rho_m + \frac{\omega_m \Lambda_m^2 R_Q}{2\pi} \left[Y_J(\omega_m) \frac{\partial}{\partial\alpha_m} \alpha_m + Y_J^*(\omega_m) \frac{\partial}{\partial\alpha_m^*} \alpha_m^* \right] \rho_m \tag{H.17}$$

The losses κ_m are added in the same fashion as for the quantum case (see Eq. (G.14)), and carrying the calculations adds a simple dissipative term to Eq. (H.17)

$$\begin{aligned} \dot{\rho}_m = &\frac{\Lambda_m^2}{4e^2} S_{II}(\omega_m) \frac{\partial^2}{\partial\alpha_m^* \partial\alpha_m} \rho_m + \frac{\omega_m \Lambda_m^2 R_Q}{2\pi} \left[Y_J(\omega_m) \frac{\partial}{\partial\alpha_m} \alpha_m + Y_J^*(\omega_m) \frac{\partial}{\partial\alpha_m^*} \alpha_m^* \right] \rho_m \\ &+ \frac{\kappa_m}{2} \left(\frac{\partial}{\partial\alpha_m} \alpha_m + \frac{\partial}{\partial\alpha_m^*} \alpha_m^* \right) \rho_m. \end{aligned} \tag{H.18}$$

Appendix I

Estimation of the quasiparticle steady-state

In this appendix we derive the condition used in the main text to check if the quasiparticle overheats due to the large thermal populations in the chain modes. Using the approach of Ref. [114], we consider the best-case scenario where a single quasiparticle is present somewhere in the chain. Taking into account only phonon-quasiparticle and photon-quasiparticle interactions, the quasiparticle distribution function $f(\epsilon)$ satisfies the kinetic equation:

$$\frac{\partial f}{\partial t} = \mathrm{St_N} f(\epsilon) + \mathrm{St_T} f(\epsilon), \tag{I.1}$$

where the right-hand side represents the collision integrals for the phoNon and phoTon processes, respectively. The energy of the quasiparticle ϵ is counted from the superconducting gap. We only consider phonon emission, neglecting phonon absorption and generation/recombination of quasiparticles, so that the collision integral can be taken from Ref. [114]:

$$\mathrm{St_N} f(\epsilon) = \frac{105}{128} \int_{\epsilon}^{\infty} \frac{f(u)}{\tau_\mathrm{n}} \frac{(u+\epsilon)(u-\epsilon)^2}{\sqrt{\Delta^7 u}} du - \left(\frac{\epsilon}{\Delta}\right)^{\frac{7}{2}} \frac{f(\epsilon)}{\tau_\mathrm{n}}. \tag{I.2}$$

where τ_n corresponds to the typical relaxation timescale associated to phonon-quasiparticle scattering and is estimated to be on order of 10–100 ns for thin aluminum films [115].

The photonic collision integral can be derived from the quasiparticle tunneling Hamiltonian which couples its tunneling to the phase drop across the junction, allowing it to absorb or emit photons when tunneling. In the low energy limit, it is written as [116]

$$\hat{H}_T = \sum_{j}^{N} \sum_{p,p',\sigma} i T_{pp'} \hat{\gamma}_{p\sigma}^{j\dagger} \hat{\gamma}_{p'\sigma}^{j-1} \sin \frac{\delta\hat{\phi}_j}{2} + \mathrm{h.c.} \tag{I.3}$$

where p, p' denote momentum indices and σ represents the spin index. The $\hat{\gamma}^j$ correspond to the quasiparticle operators for the j-th superconducting electrode, while $\delta\hat{\phi}_j = \hat{\phi}_j - \hat{\phi}_{j-1}$ denotes the superconducting phase difference across the j-th junction in the chain. The transition rate between different quasiparticles states is derived through the Fermi Golden rule, yielding

$$\Gamma_{p\to p'} = \frac{2\pi}{\hbar} |T_{pp'}|^2 f(\epsilon_p) [1 - f(\epsilon_{p'})] \mathcal{C}(\epsilon_p - \epsilon_{p'}), \tag{I.4}$$

where $\mathcal{C}$ represents the spatial average of the photonic noise spectral density [35]

$$\begin{aligned}\mathcal{C}(\epsilon) &= \frac{1}{N}\sum_j \int_{-\infty}^{+\infty} \frac{dt}{2\pi\hbar} e^{\frac{i}{\hbar}\epsilon t} \left\langle \sin\frac{\delta\hat{\phi}_j(t)}{2} \sin\frac{\delta\hat{\phi}_j(0)}{2} \right\rangle \\ &\approx \frac{1}{4N}\sum_j \int_{-\infty}^{+\infty} \frac{dt}{2\pi\hbar} e^{\frac{i}{\hbar}\epsilon t} \left\langle \delta\hat{\phi}_j(t)\delta\hat{\phi}_j(0) \right\rangle . \end{aligned} \tag{I.5}$$

Neglecting the impact of the small junction capacitance C_J on the mode profiles, we can write the $\delta\phi_j$–$\delta\phi_j$ correlator as

$$\begin{aligned}\left\langle \delta\hat{\phi}_j(t)\delta\hat{\phi}_j(0) \right\rangle = \sum_m \Lambda_m^2 \left\{\cos\left[k_m j\right] - \cos\left[k_m (j-1)\right]\right\}^2 \\ \times \left\{\left[\bar{n}(\omega_m)+1\right] e^{-i\omega_m t} + \bar{n}(\omega_m) e^{i\omega_m t}\right\}, \end{aligned} \tag{I.6}$$

where $k_m = \pi(m-1/2)/N$. The equation above also neglects the finite size of the junctions forming the chain. This is valid as long as the hot modes correspond to small wavevectors $k_m \ll \pi$, which is our case (see Figure 4.3). Moreover, since the temperature of these modes is high, $T_m \gg \hbar\omega_m$, we can neglect the zero-point energy $\bar{n}(\omega_m)+1 \approx \bar{n}(\omega_m)$, symmetrizing the correlator in frequency. In the long chain limit $N \to \infty$ the finite difference in Eq. (I.6) yields a $\sin^2(kx)$ term. Performing the spatial average and using the continuum expression (F.5) for Λ_m gives the final expression for $\mathcal{C}$:

$$\mathcal{C}(\omega) = \frac{k(\omega)^2}{4\hbar\omega} \frac{\mathrm{Re}\, Z_t(\omega)}{R_Q} \bar{n}(\omega), \tag{I.7}$$

with $k(\omega)$ determined from the continuum dispersion relation Eq. (2.116). The collision integral is then obtained by averaging Eq. (I.4) over initial and final states

$$\begin{aligned}\mathrm{St}_\mathrm{T} f(\epsilon) = \frac{4E_J}{\pi\nu_0^2\Delta} \int_0^{\omega_p} d\omega \left\{\nu(\epsilon-\hbar\omega)\left[f(\epsilon-\hbar\omega) - f(\epsilon)\right]\right. \\ \left. + \nu(\epsilon+\hbar\omega)\left[f(\epsilon+\hbar\omega) - f(\epsilon)\right]\right\} \mathcal{C}(\omega), \end{aligned} \tag{I.8}$$

where ν_0 is the normal-state density of states per spin (that we assume identical in both electrodes), and we explicitly restricted the integration bounds due to the hard cutoff coming from $\mathcal{C}(\omega)$. We also made use of the Ambegaokar-Baratoff relation linking the tunneling matrix elements, that we suppose independent of momentum $|T_{pp'}|^2 \sim t^2$, to the Josephson energy of the junction $t^2\nu_0^2 = E_J^\mathrm{chain}/\pi^2\Delta$. The factor $\nu(\epsilon)$ is the BCS density of states

$$\nu(\epsilon) = 2\nu_0 \frac{\epsilon+\Delta}{\sqrt{(\epsilon+\Delta)^2 - \Delta^2}} \theta(\epsilon) \overset{\epsilon\ll\Delta}{\approx} \nu_0 \sqrt{\frac{2\Delta}{\epsilon}} \theta(\epsilon), \tag{I.9}$$

where θ is the Heaviside function.

To estimate if the quasiparticle bath heats up we can focus on the large scale features of $f(\epsilon)$. Assuming $\epsilon \gg \hbar\omega_p$, we approximate the collision integral of Eq. (I.8) by a differential operator [114]

$$\mathrm{St}_\mathrm{T} f(\epsilon) \approx \frac{4\hbar^2 E_J^\mathrm{chain}}{\pi\nu_0^2\Delta} \left[\int_0^{\omega_p} \omega^2 \mathcal{C}(\omega)\, d\omega\right] \left\{\nu(\epsilon)\partial_\epsilon^2 f(\epsilon) + 2\partial_\epsilon\left[\nu(\epsilon)\right]\partial_\epsilon f(\epsilon)\right\}. \tag{I.10}$$

The prefactor can be readily computed in the limit of a single high temperature for the modes $\bar{n}(\omega) \approx k_B T_0/\hbar\omega$, and by taking the limits $Z_{\rm tot} \sim Z_c$ and $k(\omega) \sim (\omega/\omega_p)\sqrt{C_g/C}$,

$$\mathrm{St}_{\mathrm{T}} f(\epsilon) = \frac{1}{3\sqrt{2\Delta}} \frac{E_J^{\rm chain} k_B T_0}{\pi \nu_0} \frac{C_{\rm g}}{C} \frac{Z_c}{R_Q} \omega_p \left[\frac{1}{\sqrt{\epsilon}} \partial_\epsilon^2 f(\epsilon) - \frac{1}{\epsilon\sqrt{\epsilon}} \partial_\epsilon f(\epsilon) \right]. \tag{I.11}$$

Going to the high energies, only the second term in Eq. (I.2) is relevant, thus the steady state is characterized by

$$\Xi^{\frac{5}{2}} \left[\frac{1}{\sqrt{\epsilon}} \partial_\epsilon^2 f(\epsilon) - \frac{1}{\epsilon\sqrt{\epsilon}} \partial_\epsilon f(\epsilon) \right] = \left(\frac{\epsilon}{\beta} \right)^{7/2} f(\epsilon), \tag{I.12}$$

where we introduced Ξ the characteristic energy scale of the problem

$$\Xi = \left[\frac{1}{6\pi^2\sqrt{2}} (\hbar\omega_p)^2 k_B T_0 \Delta^3 \sqrt{\frac{C_{\rm g}}{C}} \frac{\tau_{\rm n}}{\hbar\nu_0} \right]^{1/6}, \tag{I.13}$$

and used $E_J^{\rm chain} = (\hbar\omega_p R_Q/2\pi Z_c)\sqrt{C/C_g}$. As in Ref [114], making the change of variable $z = 4^{-1/3}(\epsilon/\Xi)^2$ transforms Eq. (I.12) into the Airy equation $\partial_z^2 f - zf = 0$, meaning that in the high energy limit the distribution function is proportional to the Airy function

$$f(\epsilon) \propto \mathrm{Ai}\left[4^{-1/3} \left(\frac{\epsilon}{\Xi} \right)^2 \right] \overset{\epsilon \gg \Xi}{\sim} e^{-\frac{1}{6}\left(\frac{\epsilon}{\Xi}\right)^3}. \tag{I.14}$$

Thus checking if $\Xi > \Delta$ tells us if the quasiparticle reach energies higher than Δ, allowing it to break Cooper pairs and forms new quasiparticles, leading to overheating.